Left Ventricular Wall Detection from MRI Scans using Random Walk

Sarada Prasad Dakua

Left Ventricular Wall Detection from MRI Scans using Random Walk

A

Thesis Submitted

in Partial Fulfilment of the Requirements

for the Degree of

DOCTOR OF PHILOSOPHY

By

Sarada Prasad Dakua

Department of Electronics and Electrical Engineering

Indian Institute of Technology Guwahati

Guwahati - 781 039, INDIA.

April, 2011

Left Ventricular Wall Detection from MRI Scans using Random Walk

A

Thesis Submitted

in Partial Fulfilment of the Requirements

for the Degree of

DOCTOR OF PHILOSOPHY

By

Sarada Prasad Dakua

Department of Electronics and Electrical Engineering

Indian Institute of Technology Guwahati

Guwahati - 781 039, INDIA.

April, 2011

Certificate

This is to certify that the thesis entitled "**Left Ventricular Wall Detection from MRI Scans using Random Walk**", submitted by Sarada Prasad Dakua, a research scholar in the *Department of Electronics and Electrical Engineering, Indian Institute of Technology Guwahati*, for the award of the degree of **Doctor of Philosophy**, is a record of an original research work carried out by him under my supervision and guidance. The thesis has fulfilled all requirements as per the regulations of the Institute and in my opinion has reached the standard needed for submission. The results embodied in this thesis have not been submitted to any other University or Institute for the award of any degree or diploma.

Dated: 15. 04. 2011
Guwahati.

Dr. J. S. Sahambi
Associate Professor
Dept. of Electronics and Electrical Engg.
Indian Institute of Technology Guwahati
Assam - 781 039
India.

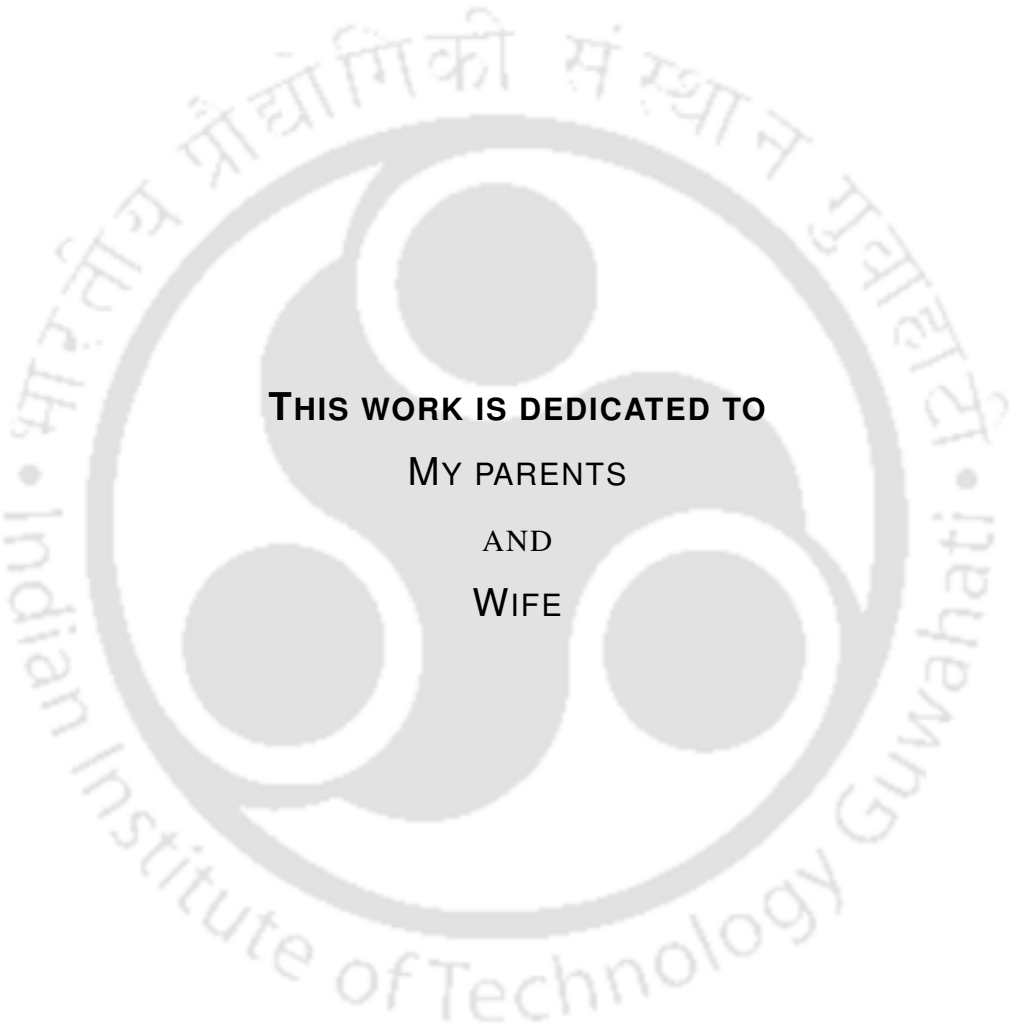

THIS WORK IS DEDICATED TO

MY PARENTS

AND

WIFE

Acknowledgements

First of all, I feel it is a great privilege to express my deepest and most sincere gratitude to my supervisor Dr. J. S. Sahambi, for his valuable guidance, moral support and endless encouragement. I would also like to thank my doctoral committee members, Prof. P. K. Bora, Prof. S. Dandapat, Dr. S. R. M. Prasanna and Dr. A. Mitra. Their suggestions, comments and assistance have been valuable. My special thanks also extend to Dr. M. K. Bhuyan for his worthful support. I would also like to express my gratitude to Dr. Alexander Andreopoulos for providing me the cardiac MRI data sets without which this work would not have been possible. I am thankful to all research engineers in the department especially Mr. Sanjib Das, for his smooth cooperation during the entire course of this work in the ISPL laboratory. I am grateful to all the other faculty members and staff of the department of EEE.

Next, I need to thank all the people who create such a good atmosphere in the lab; among my friends, I would like to extend my special thanks to Katiyar, Anand, Kartik, Rupaban sir, Deka sir, Padampriyal, Dr. Padhy bhaina, Dr. Vinod bhaiya, Dr. Babu bhaiya, Dr. Senthil bhaiya, Rajib, Kuntal, Narasimhamurthy sir, Pati sir, Ramesh sir, Mukesh sir and Ganguly madam. I would also like to thank Mr. R. K. Das for his sincere effort in editing this thesis. I would also take this opportunity to apologize for everything that annoyed anybody intentionally and unintentionally.

My parents, wife, brothers, and sister were always behind me, regardless of being miles away. Their love and confidence gave me strength when I needed it most. I would like to express my appreciation to my eldest brother, Mr. Annada Prasad Dakua for supporting me to join engineering at the toughest mode of my career. Finally, I would like to thank my wife for her inherent support during the junctures in the course of my research.

(Sarada Prasad Dakua)

Abstract

The left ventricle (LV) is one of four chambers (two atria and two ventricles) in the human heart. Because it supplies oxygenated blood to the entire body, it possesses a stance of great significance in the medical diagnosis. In order to know the problem against any chest pain, physicians first try to look to the shape of the LV. Therefore, its segmentation always remains as the first and foremost step. The accuracy of any segmentation is usually achieved through lessening the user interaction. A semi-automatic method for image segmentation that uses random walks was introduced in 2006. This approach requires user guidance to define the desired content to be extracted in the image. This is fast, effective and intuitive which can successfully perform segmentation irrespective of the image type. At the same time, its performance depends largely on the degree of homogeneity and separability of the objects present in the image. The lesser is the obscurity, unlike the cardiac magnetic resonance images, the better is its execution. Since myocardium (thick layer of cardiac muscle) is responsible for the contraction and relaxation of the ventricle, its inner (endocardium) and outer (epicardium) lining should be extracted simultaneously. The main contributions of this thesis are as follows: 1) In endocardial wall detection, Random Walk approach faces many challenges while applying this algorithm on ischemic cardiac magnetic resonance (CMR) images (as they are more obscure), one of them is initial seed(s) selection. Furthermore, the free parameter β in this algorithm does have the influence on its performance, which is usually decided by the user. In order to reduce the user interaction (because more user interaction introduces larger variability in the performance), attempts have been made to solve these two issues in our research and made the algorithm automatic, 2) The grey level distribution of myocardial muscle does not differ much from the outer surrounding muscles, therefore, Random Walk approach is little suitable for its meaningful segmentation. Instead, a modified active contour model that operates on the endocardial boundary is applied to section out the epicardium, 3) The methodologies adapted in endocardial wall detection do not produce satisfactory result, especially in case of short axis CMR images. After a thorough review of the nature of weighting function, three functions for the same purpose have been suggested to achieve better segmentations, and finally 4) To compare the performances of these weighting functions, an unsupervised technique has been proposed in the end.

Contents

List of Figures

List of Tables

Nomenclature

LV	Left Ventricle.
MRI	Magnetic Resonance Imaging.
CT	Computed Tomography.
CMR	Cardiac Magnetic Resonance.
NMR	Nuclear Magnetic Resonance.
RF	Radio Frequency.
CAD	Coronary Artery Disease.
VSD	Ventricular Septal Defect.
EM	Expectation Maximization.
STACS	Stochastic Active Contour Scheme.
DoG	Difference of Gaussian.
DoLoG	Difference of Laplacian of Gaussian.
LoDroG	Laplacian of Derivative of Gaussian.
NV	Noise Variance.
RPD	Relative Point-wise Distance.
MSE	Mean Square Error.
CRLB	Cramer-Rao Lower Bound.
ML	Maximum Likelihood.
FOM	Figure of Merit.

Mathematical Notations

I	Iamge.
G	Graph.
V	Vertex.
E	Edge.
w_{ij}	Weight of the edge between nodes i and j.
d_i	Degree of node i.
N_i	Neighborhood nodes of i.
u	Temperature.
x	Postilion.
t	Time.
L	Length.
$(b_{stop}, g_{stop}))$	Co-ordinate of stopping pixel.
$u\,(x,t)$	Rod intensity (actual pixel intensity in the original image) at the position x at the time t.
DF_f	Deciding function.
E	Threshold.
N_s	Number of steps.
z	Position in the complex plane.

l	Step size.
d	Distance.
Ł	Label.
J_{un}	Laplacian matrix of the unseeded nodes $x^{Ł}$.
β	Parameter used in the weighting function in determining the adjacency matrix.
P	Transition probability.
$\overline{\lambda}$	Eigen values of the Laplacian.
$V\,(b, g)$	Original image may be described by an array of $B \times G$ elements
$CRLB$	Cramer-Rao lower bound.
I	Fisher information matrix.
F	Fitting term.
C	Variable curve.
ϕ	Contour.
L_u	Edge weights for the unlabeled pixels.
m	Set of labels for the seed points.
B^T	Edge weights corresponding to the labels.
X	Probability for each pixel being a member of the labels.
x	Textual object.
y	Class.
$v(x)$	Blurred edge.
t	Width of the region of interest.
σ_s	Extent of the blurring.
E_v^w	Characteristic function with respect to an edge, v, and a weighting function, w.

n	Order of the derivative.
σ^2	Variance.
X_0, Y_0 and Z_0	X, Y and Z values for the reference white.
ϕ	Scale function.
ψ	Wavelet function.
A_j	Approximate coefficients.
D_{jk}	Detail coefficients.
K	Binary image.
$\sigma_W^2(t)$	Intra-class variance.
I_s	Segmentation contour.
I_t	Ground truth contour.
$d(i)$	Distance between the i^th pixel of I_s and the nearest pixel of I_t.

Chapter 1

Introduction

The human heart is a powerful muscular organ situated in the chest. It is the primal pump of our circulatory system. An average heart has a throughput of 7200 litres of blood per day. The left ventricle is one of four cavities in the heart. The wall enclosing the left ventricle (LV) is significantly thicker than other parts of the heart wall, making the LV relatively independent with regards to muscle dynamics. The LV receives oxygen-enriched blood from the lungs via the left atrium and pumps it out to the rest of the body. Therefore in the respiration process, LV is an important constituent in the heart [1]. Whenever any dysfunction in the heart seems to have occurred, radiologists first desire to observe all the activities in LV minutely. Therefore, they need some kind of inflections that express how the action or state could be conceived.

To date, there are many imaging modalities, magnetic resonance imaging (MRI) is one of them which is noninvasive in nature [2]. Some of its advantages, viz. 1) low ionizing radiation, 2) ability to provide maximum information for diagnosis by a single test and 3) less operator dependence, keep it ahead of other imaging modalities like X-ray, CT (Computed Tomography) scan and PET (Positron Emission Tomography), etc. There are several applications of MRI, viz. 1) oncologic imaging, 2) for the breast, it is a valuable adjunct to mammography to detect multifocal tumors, 3) it defines the response to chemotherapy, 4) in the liver, it is valuable in characterizing masses, and so on. CT has been popular since a long time. With emergence of MRI, in the opinion of many radiologists, MRI is superior to CT [3]. Here, a brief comparison is given in Table 1.1.

Another reason for its popularity is that it can provide a lot of information, which otherwise may require a number of tests to perform. MRI produces images of high quality, both with respect to noise and contrast. Additionally, an MRI machine can scan arbitrarily oriented planes

Table 1.1: Comparison between MRI and CT scan

Characteristics	MRI	CT scan
Scan completion time	Within 5 minutes	Around 30 minutes
Radiation exposure	None	Moderate to high radiation
Scope of application	Versatile	Outlines bone accurately
Details of soft tissues	Gives higher details in soft tissues	Gives less details in soft tissues

[4]. Because of these with other benefits, it has become a leading imaging modality for clinical diagnosis enabling cardiologists and radiologists to perform diagnostic findings at high spatial image resolution.

1.1 Cardiac Magnetic Resonance Imaging

MRI is based on the principle of nuclear magnetic resonance (NMR) [5]. The NMR phenomenon was discovered independently by Felix Bloch and Edward Purcell in 1946. After 1970s, the NMR phenomenon was applied to medical imaging by Raymond Damadian.

MRI is a very complex subject; a brief explanation of the physics behind the technology is as follows: Each nucleus has a fundamental property, viz., spin [6]. When a strong magnetic field is imposed on the region of interest, these spins align with the imposed magnetic field. Most of the spins cancel each other out because of difference of direction, but an excess spin along the applied field results a tiny net magnetization in that direction. The alignment is not exact; the nucleons precess, or wobble, about the applied magnetic field with a motion similar to that of a spinning top. If radio waves (i.e. more than 30 KHz) are applied with resonance frequency, then this energy can be absorbed by the nucleons and cause a transition to a higher spin energy level. When the radio frequency (RF) is turned off, the system returns to its original state aligning with the magnetic field. During this time the nucleons exert RF waves. These are registered and various techniques can be used to create an image from this data. The sequential procedure is given in Figure 1.1.

An MRI machine forms an image by taking readings from the nuclei of the atoms in the various parts of matter in the body. The registered data is a wide range of frequencies [7]. This

Figure 1.1: Schematic diagram for CMR data acquisition.

data is converted to digital form. Inverse Fourier transform is used to obtain the original image from the frequency data [8].

As mentioned in Table 1.1, the strength of MRI is its ability to examine soft tissue of similar density with greater detail than CT [6]. While CT and conventional X-ray imaging renders dense structures such as bones with great detail, MRI has its main contrast span in the range of soft tissue. Its resolution is similar to that of CT. Also, MRI can depict blood vessels without the use of contrast enhancers. In general, the heart, the vascular system and the thoracic region are some of the anatomical regions, of which MRI is becoming an increasingly popular examination technique. Since in this work, MRI of heart is the only concern, cardiac magnetic resonance (CMR) images will uniquely be discussed here onwards.

1.2 Need of Left Ventricle Segmentation

There are many advantages of LV segmentation in the diagnosis of cardiovascular diseases. In particular, the study of the shape and motion of the heart is important because many heart diseases are thought to be strongly correlated to the shape and motion of the heart and the segmentation provides adequate information about the shape and size of an object; some prominent examples of such heart diseases include ischemia and right ventricle (RV) hypertrophy. Also, LV segmentation is primarily motivated by the need to clinically diagnose a feature of the heart with potential problems such as:

- Left Ventricular Hypertrophy - thickening of the myocardium (muscle) of the LV of the heart;
- Ventricular Septal Defect (VSD) - the wall dividing the left and right ventricles of the heart, congenital VSDs are collectively the most common congenital heart defects;

- Atrial Septal Defect (ASD) - a form of congenital heart defect that enables blood flow between the left and right atria via the interatrial septum;
- Congenital Heart Defect (CHD) - a defect in the structure of the heart and great vessels of a newborn;
- Coronary Artery Disease (CAD) - stenosis, atresia, regurgitation, etc. are the diseases due to improper blood flow through the heart; and so on.

Moreover, the segmentation is very useful in image guided surgery, medical data visualization, measurement of ejection fraction, left ventricular mass calculation, left ventricular wall motion detection and localization of the heart chambers. Therefore, it is an important and essential step in CMR image analysis; it provides the stage for the quality interpretation. This processing either consists in partitioning an image into several regions or in detecting their frontiers. Although the field of segmentation is built on foundation of mathematical and probabilistic formulations, human intuition and analysis play a central role in the choice of one technique versus the other. This choice is often made based on subjective and visual judgments.

Segmentation of CMR data poses a challenging problem as compared to the nonmedical images. A most important factor dwelled in CMR data is noise, it is inherent in the process of acquisition [9]. The image noise originates in the patient (thermal noise) and is added during the processing of the signal in the receiver chain [10]. In the receiver chain, noise may be generated in the pre-amplifier and at the connection between the pre-amplifier and the radio frequency (RF) receiver coil. In the RF coil, which is a conductor, thermal noise is produced by the stochastic motion of free electrons. This motion is caused by the ohmic losses in the RF coil and eddy current losses in the patient. The MRI image/signal component of the measurements is present in both real and imaginary channels; each of the two orthogonal channels is affected by additive white Gaussian noise. The noise in the reconstructed complex-valued data is thus complex white Gaussian noise. Most commonly, the magnitude of the reconstructed MRI image is used for visual inspection and automatic computer analysis. Since the magnitude of the MRI signal is the square root of the sum of the squares of two independent Gaussian variables, it follows a Rician distribution. In low intensity (dark) regions of the magnitude image, the Rician distribution tends to a Rayleigh distribution and in high intensity (bright) regions it tends to a Gaussian distribution; a practical consequence is a reduced image contrast [11].

Usually, poor segmentation results from high noise level present in MR images (if proper care is not taken). Another difficulty lies in the large volume of data involved and the on-time requirement of medical applications. The time constraints vary among applications, ranging from several tens of milliseconds for online surgical monitoring, to seconds for interactive volumetric measures, to minutes or hours for off-line processing. Another major hurdle is the high variation of image properties in the data, making it hard to construct a general model. Apart from the above difficulties, the system faces other modalities, such as partial volume effects, variation in scanning protocols, and so forth.

1.3 Concept of Segmentation

Image segmentation is perceived as the partition of an image into a set of non-overlapping regions whose union is the entire image. Some rules to be followed for regions that result from an image segmentation can be expressed as [12]:

- They should be uniform and homogeneous with respect to some characteristics;
- Their interiors should be simple and without many small holes;
- Adjacent regions should have significantly different values with respect to the characteristics on which they are uniform; and
- Boundaries of each segment should be simple, not ragged, and must be spatially accurate.

A simple image can mathematically be formulated as follows:
Suppose the whole image (u) is represented by a number of partitions u_i, where i =1, 2, ..., n; n = number of partitions. These partitions are assumed to be disjoint non-empty regions of u. An ideal image to result a better segmentation should consist of the following conditions [13]:

1. $\bigcup_{i=1}^{n} u_i = u$;
   i.e. the summation of segmented regions should include all pixels in an image.

2. For all i and j, $i \neq j$, there exists $u_i \bigcap u_j = \phi$;
   i.e. different segmented regions should not overlap each other.

3. For i =1, 2, ..., n, it must have $P(u_i) = TRUE$;
   i.e. the pixels in the same segmented regions should have similar property.

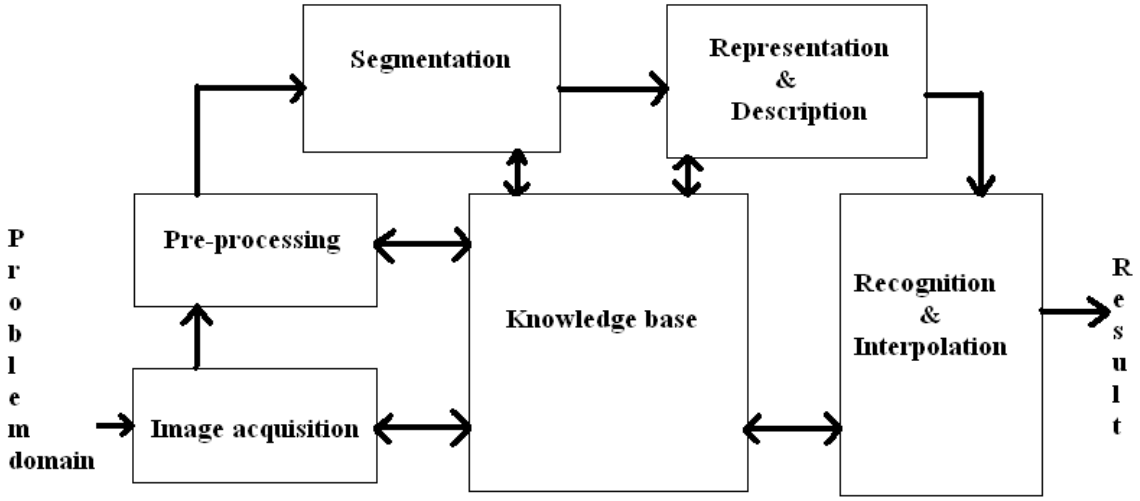

Figure 1.2: A simple block diagram explaining the processes before and after segmentation.

4. For all $i \neq j$, there exists $P(u_i \bigcup u_j) = FALSE$;
   where $P(u_i)$ is a uniformity predicate for all elements in set u_i and ϕ represents an empty set;
   i.e. the pixels belonging to different regions should have different properties.

5. For all i =1, 2, ..., n, u_i is a connected component;
   i.e. the pixels in the same segmented region are connected.

1.4 Scope of Image Segmentation

Image segmentation is often described as the process that subdivides an image into its constituent parts and extracts the parts of interest (objects). It is one of the most critical tasks in automatic image analysis because the segmentation results will affect all the subsequent processes of image analysis (as shown in Figure 1.2), such as object representation & description, feature measurement and even the following higher level tasks (e.g., object classifications & scene interpretation).

The blocks in Figure 1.2 function as follows:

- Image acquisition - It digitizes the signal produced by the sensor;
- Pre-processing - It enhances the image quality;
- Segmentation - It partitions the input image into constituent parts;

- Description/feature selection - It extracts description of image objects suitable for further computer processing;
- Recognition and interpolation - It assigns a label to the object based on the information provided by its descriptor and interpolator assigns meaning to a set of labeled objects; and
- Knowledge base - It helps for efficient processing as well as intermodule co-operation.

The interest towards segmentation geared up after the introduction of Robert operator [14] in 1965. This edge detector was the first step toward decomposing an image into its constitutional components. Since then, the dimension of research on segmentation has increased significantly, the result of much devoted effort. In the meantime, concept and scope of images have been extended greatly. The extension of 2-dimensional (2D) images to 3-dimensional (3D), still images to moving images or sequences of images (video), grey level images to color or multi band images, etc. have also helped the concepts and techniques of image segmentation expand widely. In spite of several decades of investigation, image segmentation remains a challenging research topic with growing number of types of images.

1.4.1 Dimensionality

Dimensionality refers to whether a segmentation method operates in a 2D image domain or a 3D image domain. Methods that rely solely on image intensities are independent of the image domain. However certain methods, such as deformable models, Markov random fields, and region growing, incorporate spatial information and may therefore operate differently depending on the dimensionality of the image. Generally, 2D methods are applied to 2D images and 3D methods are applied to 3D images. In some cases, however, 2D methods are applied sequentially to the slices of a 3D image [15]. This may arise because of practical reasons, such as ease of implementation, lower computational complexity, and reduced memory requirements. In addition, certain structures are more easily defined along 2D slices. Over the past decade, segmentation techniques have gained importance in the quantitative analysis of medical images and in image guided interventional procedures. The hypothesis of this research work is, whether the suitable use of an immersing environment can improve (in terms of accuracy, speed and user experience) classic 2D and 3D (i.e. 2D+time) slice-based image segmentation techniques. We talk about the environment that makes use of virtual real techniques to provide the user an improved experience.

1.5 Selected Literature Survey

Fully automatic segmentation of the LV in bright blood breath-hold CMR images is non-trivial because the image intensities of the cardiac chambers vary due to differences in blood velocity [16]. In particular, blood that flows into the ventricles produces higher intensities in the acquired image than blood which remains in the ventricles. Locating the LV endocardium is further complicated by the fact that the right ventricle and aorta often appear jointly with the LV in many images of the heart. Similarly, automatic segmentation of low signal-to-noise ratio (SNR) cardiac images (e.g. body coil MR or ultrasound) is difficult because intensity variations can often obscure the LV boundary [17].

A wide range of very specialized segmentation techniques currently exist and since the research is very active in this field, the panel of available techniques and algorithms constantly evolves. In choosing a segmentation technique for a particular task, it is important to understand the fact that there is no universally applicable segmentation technique that will work for all types of medical images and all organs. For example, the segmentation of brain tissue has different requirements from the segmentation of the liver. General imaging artifacts such as noise, partial volume effects (where multiple tissues contribute to a single pixel or voxel resulting in a blurring of intensity across boundaries), and motion can also have significant consequences on the performance of segmentation algorithms. Furthermore, each imaging modality has its own idiosyncrasies with which it is contended. There is currently no single segmentation method that yields acceptable results for every medical image. This section tries to present a simple yet homogeneous and relevant classification of the existing techniques into a number of families. For each family the general functional philosophy is analyzed and a non-extensive list of algorithms is presented, with a short explanation of the specificities and possible difficulties (while applying on CMR images) for each of them. There are numerous types of classifications proposed in the specialized literature, each of which is relevant respectively to the point of view required by the study. Since this research project deals with medical image segmentation, where a large majority of the acquired data is grey-scaled, all the techniques concerning color images are left aside.

Broadly to state, there are two types of image segmentation algorithms, viz., discontinuity based and similarity based. Therefore, the categorization may come as the following:

1. Discontinuity based approach - This type of algorithms rely on the abrupt changes (usually at the edge of the objects) in intensity in grey level images. Edge detection is a fundamental

tool used in most image processing applications to obtain information from the frames as a precursor step to feature extraction and object segmentation. Edge is a boundary between two homogeneous regions. Edge detection refers to the process of identifying and locating sharp discontinuities in an image. The following particulars are keyed out by these methods.

(a) Isolated points - The detection of isolated points in an image is straight forward by using a suitable mask; we can say that a point has been detected at the location on which the mask is centered, if response of the mask $|R| > T$, where T is the threshold and $R = -\sum_{i=1}^{n} x_i + nx_c$. The term x, n and c represent the image pixel, number of pixels inside a region of interest (equal to the mask size) and center of the mask, respectively. The idea is that the gray level of an isolated point will be quite different from the gray level of its neighbors.

(b) Lines - Let R_1, R_2, R_3, and R_4 denote the responses of four masks, and they run along the same image. Then at a certain point, one can say that the mask which has the maximum response, will make the line into its direction, i.e. if $R_2 > R_1$, R_3, R_4 then the line has the direction of R_2.

(c) Edges - The edge is the boundary between two regions with relatively distinct grey level properties. It is assumed here that the transition between two regions can be determined on the basis of grey level discontinuities alone.

An edge in an image is a significant local change in the image intensity, usually associated with a discontinuity in either the image intensity or the first derivative of the image intensity. Discontinuities in the image intensity can be either step edge, where the image intensity abruptly changes from one value on one side of the discontinuity to a different value on the opposite side, or line edges, where the image intensity abruptly changes value but then returns to the starting value within some short distance.

2. Similarity based approach - This type of algorithms group those pixels which are similar in some sense. The task of grouping is performed by the following operations.

(a) Thresholding based operations - Clustering of pixels is executed according to the threshold value taken. The pixels below or above the threshold value belong to different categories. Three types of processing for thresholding are adapted as follows:

i. Global processing - If the threshold is a function of pixel intensity.

ii. Local processing - If the threshold is a function of local property in a neighborhood centered at a pixel location and pixel intensity.

iii. Adaptive processing - If the threshold is a function of local property in a neighborhood centered at a pixel location, pixel intensity and pixel location.

(b) Knowledge based operations - The prior knowledge regarding the object in the image is used to find and tailor a general segmentation method to the specific application. Basically, there are two models:

i. Deformable models - These models provide a framework that allows the incorporation of global priors. It captures the local properties through front evolution, without the need of local primitive sampling. Such a popular model is level set method.

ii. Statistical models - Methods such as active contour shape models and active appearance models use statistical models to represent prior knowledge.

(c) Region based operations - Grouping of pixels is performed according to some criterion before hand. They are:

i. Based on primitive detection;

ii. Statistical segmentation; and

iii. Graph based - The methodology is based on graph theory. Again, it is of two types:

A. Pixel based - The image is considered as a weighted graph, whereas the nodes are the pixels in the original image. The edges together with their associated weights are defined using the local information of the pixels. Random walk approach comes under this category.

B. Region based - It requires an initial image over-segmentation that produces hierarchical top-down region based decomposition.

Manual tracing has been considered the gold-standard for cardiac output quantification in clinical practice. However, manual tracing is a labor-intensive and time consuming process that is subject to inter- and intra-observer variability. Segmentation by experts is variable up to 20 percent [18], it is therefore desirable to use algorithms that are accurate and require little user

interaction. A large class of automatic and semi-automatic segmentation methods fall into the class of variational methods, also referred to as active contour models. Active contour includes parametric active contour (or snake) and geometric active contour (or level set).

These deformable models are physically motivated for delineating region boundaries using closed parametric curves or surfaces that deform under the influence of internal and external forces. To delineate an object boundary in an image, a closed curve or surface must first be placed near the desired boundary and then allowed to undergo an iterative relaxation process. Internal forces are computed from within the curve or surface to keep it smooth throughout the deformation. External forces are usually derived from the image to drive the curve or surface towards the desired feature of interest. The main advantages of deformable models are their ability to directly generate closed parametric curves or surfaces from images and their incorporation of a smoothness constraint that provides robustness to noise and spurious edges. A disadvantage is that they require manual interaction to place an initial model and choose appropriate parameters. Snake model [19, 20] is reliable in poor resolution images but the topology is to be known in advance. When more splitting and merging occur then the problem arises in the adaptability of the algorithm in terms of its topology and regularity [21].

Level set methods [22–24] that have been extensively used in medical image segmentation overcome some of the limitations. In probabilistic methods, this is equivalent to maximizing a likelihood or a posteriori probability. Given the image u, we desire the segmentation $\widehat{x}$ such that

$$\widehat{x} = \arg \min_{x} \xi(x, u) \tag{1.5.1}$$

where ξ, the energy function, depends on the observed image u and a segmentation x. Defining an appropriate ξ is a major difficulty in designing segmentation algorithms because of the wide variety of image properties that can be used, such as intensity, edges, and texture. In addition to information derived from the image, prior knowledge can also be incorporated to further improve performance. The advantage of posing a segmentation as an optimization problem is that it precisely defines what is desirable in the segmentation. Although level set methods gained tremendous popularity, still some problems like computational complexity, re-initialization [25, 26] of the zero level set exist. In the early level set methods, the computation is carried out on the entire domain making the computation slow. Narrow band level set methods [27] restrict the computation to a narrow band around the zero level set, but it does not reduce the computational cost to a reasonable limit [28]. Active contours without edges [29] is useful in detecting the object edge

irrespective of the initial contour placement. At the same time, mean intensities of all the regions must be different for a successful segmentation.

A thresholding procedure attempts to determine an intensity value, called the threshold, which separates the desired classes [30]. The segmentation is then achieved by grouping all pixels with intensity greater than the threshold into one class, and all other pixels into another class. Thresholding is a simple yet often effective means for obtaining a segmentation in images, where different structures have contrasting intensities or other quantifiable features. The partition is usually generated interactively, although automated methods do exist [31]. Thresholding is often used as an initial step in a sequence of image processing operations. Its main limitations are that in its simplest form only two classes are generated and it can not be applied to multi-channel images (if more than one measurement is made, e.g. dual-echo MRI, the image is called a multi-channel image). In addition, thresholding typically does not take into account the spatial characteristics of an image. This causes it to be sensitive to noise and intensity inhomogeneities, which can occur in CMR images.

Classifier methods are pattern recognition techniques that seek to partition a feature space derived from the image using data with known labels [32]. Classifiers are known as supervised methods since they require training data that are manually segmented and then used as references for automatically segmenting new data. There are a number of ways in which training data can be applied in classifier methods. A simple classifier is the nearest-neighbor classifier, where each pixel or voxel is classified in the same class as the training datum with the closest intensity. The k-nearest-neighbor (kNN) classifier [33] is a generalization of this approach, where the pixel is classified according to the majority vote of the k closest training data. The kNN classifier is considered a nonparametric classifier since it makes no underlying assumption about the statistical structure of the data. Another nonparametric classifier is the Parzen window [34], where the classification is made according to the majority vote within a predefined window of the feature space centered at the unlabeled pixel intensity.

A commonly used parametric classifier is the maximum likelihood (ML) or Bayes classifier [35]. It assumes that the pixel intensities are independent samples from a mixture of probability distributions, usually Gaussian. This mixture, called a finite mixture model, is given by the probability density function

$$f\left(y_j;\theta,\pi\right)=\sum_{k=1}^{K}\pi_k f_k\left(y_j;\theta_k\right) \tag{1.5.2}$$

where y_j is the intensity of pixel j, f_k is a component probability density function parameterized by θ_k, and $\theta = [\theta_1, ...\theta_K]$. The variables π_k are mixing coefficients that weight the contribution of each density function and $\pi = [\pi_1...\pi_K]$. Training data is collected by obtaining representative samples from each component of the mixture model and then estimating each θ_k accordingly. For Gaussian mixtures, this means estimating K means, covariances, and mixing coefficients. Classification of new data is obtained by assigning each pixel to the class with the highest posterior probability. When the data truly follows a finite Gaussian mixture distribution, the ML classifier can perform well and is capable of providing a soft segmentation composed of the posterior probabilities.

Standard classifiers require that the structures to be segmented possess distinct quantifiable features. Because training data can be labeled, classifiers can transfer these labels to new data as long as the feature space sufficiently distinguishes each label as well. Being non-iterative, they are relatively computationally efficient and unlike thresholding methods, they can be applied to multi-channel images. A disadvantage of classifiers is that they generally do not perform any spatial modeling. This weakness has been addressed in recent work extending classifier methods to segmenting images that are corrupted by intensity inhomogeneities [36]. Another disadvantage is the requirement of manual interaction for obtaining training data. Training sets can be acquired for each image that requires segmenting, but this can be time consuming and laborious.

Similarly, expectation maximization (EM) [37] algorithm has the ability to estimate the parameters of different classes. Unfortunately, EM algorithm has several limitations [38]: 1) the number of the clusters has to be pre-determined; 2) the initial parameters of EM influences the performance of the algorithm; and 3) it does not work as well for the concave clusters. Stabilized inverse diffusion equations [39], being based on a simple spring-mass model experiences a tough task while defining a suitable force function. Integration of fuzzy logic with data mining techniques has become one of the key constituents of soft computing in handling the challenges posed by massive collections of natural data. The fuzzy clustering algorithms allow the clusters to grow into their natural shapes. Fuzzy c-means clustering is similar to K-means clustering in many ways but incorporates fuzzy sets concepts of partial membership and forms overlapping clusters to support it. Such a method [40] is reported to be applicable to any dimensional representation and at any resolution level of an image series. The main drawback [41] of this method is from the restriction that the sum of membership values of a data point in all the clusters must be one and this tends to give high membership values for the outlier points. So the algorithm

has difficulty in handling outlier points. Secondly, the membership of a data point in a cluster depends directly on its membership values in other cluster centers and this sometimes happens to produce unrealistic results. Thirdly, its inability to calculate the membership value if the distance of a data point is zero.

Markov random field (MRF) modeling itself is not a segmentation method but a statistical model [42] which can be used within segmentation methods. MRFs model spatial interactions between neighboring or nearby pixels. These local correlations provide a mechanism for modeling a variety of image properties [43]. In medical imaging, they are typically used to take into account the fact that most pixels belong to the same class as their neighboring pixels. In physical terms, this implies that any anatomical structure that consists of only one pixel has a very low probability of occurring under a MRF assumption. MRFs are often incorporated into clustering segmentation algorithms such as the K-means algorithm under a Bayesian prior model [44]. The segmentation is then obtained by maximizing the a posteriori probability of the segmentation given the image data using iterative methods such as iterated conditional modes or simulated annealing [45]. The segmentation is much smoother than the that of non-MRF. A difficulty associated with MRF models is proper selection of the parameters controlling the strength of spatial interactions. Too high a setting can result in an excessively smooth segmentation and a loss of important structural details [43]. In addition, MRF methods usually require computationally intensive algorithms.

Atlas-guided approaches have been applied mainly in MR brain imaging. An advantage of atlas-guided approaches is that labels are transferred as well as the segmentation. They also provide a standard system for studying morphometric properties [46]. Even with non-linear registration methods, however, accurate segmentations of complex structures is difficult due to anatomical variability. Moreover, atlas-based segmentation has been of limited use in presence of large space-occupying lesions [47]. The watershed algorithm uses concepts from mathematical morphology to partition images into homogeneous regions [48]. This method can suffer from over-segmentation, which occurs when the image is segmented into an unnecessarily large number of regions. Thus, watershed algorithms in medical imaging are usually followed by a postprocessing step to merge separate regions that belong to the same structure [49]. There are also many model based segmentation techniques [50]. One substantial limitation of such methods is that their accuracy may be restricted either by the uncertainties in image content or by the intrinsic properties by the model itself, such as prior shape constraints [51].

Segmentation with ratio cut [52] faces challenges in producing correct segmentations of blurry edged objects [53]. A discrete singular convolution based algorithm [54] effectively detects edges by varying the parameter α according to the degree of noise present in the image. This method is reported to be effective under severe Gaussian white noise; unfortunately, the method while applying on CMR images fails to produce a good result as noise distribution is Rician [9]. Moreover, this method produces multiple undesired edges inside the LV. The algorithm reported in [55] relies on the shape of the object, while the approach studied in [56] sometimes causes over segmentation. The mixture of fuzzy and EM algorithm [57] is useful for automatic LV segmentation but the complexity in validation is more; the EM algorithm has to be stopped before a deteriorating "checkerboard effect" [58] shows up. A different clustering technique [59] for multi-spectral image is effective only when applied to land cover images.

Stochastic active contour scheme (STACS) [60] for automatic image segmentation is designed to overcome the normal problems with low contrast and turbulent blood flow. The difficulty lies in the modeling, which requires the prior knowledge of the heart for a better assessment of the object boundary. The software tools are partly developed in MRI techniques. Unsupervised clustering and Canny edge detection method was applied to segment the LV cavity and myocardium by Lynch et al. [61], which may render the region-base methods unusable for those structure of discontinuous intensity and inhomogeneities. Also, the level set method used in this proficiency may require considerable thought in order to construct appropriate velocities for advancing the level set function [62]. Sum et al. have proposed an approach [63] for vessel extraction using a level set based active contour. Unfortunately, this is less capable in handling bifurcations and the sensitivity to imaging artifacts, producing discontinuities of the coronary vessels.

Graph-based methods also have been successfully employed in image segmentation without heavy reliance on explicitly learned or encoded priors. However, graph cuts algorithm [64] as a fundamentally two-label algorithm, is more susceptible to the "small cuts" problem in the presence of weak boundaries. In his work, the method can be applied only to image segmentation problems where the cost of the cut corresponds to an energy function which is globally minimized. It has been difficult to include high level information into the graph cut formulation. Presence of high noise level prevents the Normalized Cut [65] method from performing to its potential [66]. A fast and semi-automatic algorithm proposed in [67] comes under this category and is based on Random Walk. It does not suffer from the "small cut" problem and extends naturally to an arbitrary number of labels; we incline more towards this method due to various reasons as

described below.

Justification for the Random Walk based segmentation:

An automatic method is always desirable to reduce manual error. On other hand, the reduction in user's intervention is often achieved at the cost of segmentation accuracy. Therefore a semi-automatic method, though needs user's interaction, is more suitable because it is possible to guide the resulting contour in obtaining the desired output. In context with this, Random Walk based image segmentation is semi-automatic in nature and it has certain advantages which make it more suitable than other existing semi-automatic methods, some of them are: 1) noise robustness, 2) usage of only one free parameter, and 3) fast computation and editing. Moreover, it does not require any pre-assumption or knowledge of the object to be segmented. Especially, this particular aspect has attracted our attention to use it in CMR image segmentation. Its primary disadvantage is that it requires manual interaction to obtain the seed points, for example, the placement of initial seeds on various objects is a tough task in slow intensity varying CMR images. During the course of present research work, many other challenges have arisen. This thesis attempts to solve these challenges.

Random Walk has many applications nowadays not only in visual computing but also in genetics, physics, medicine, chemistry, computer science, just to cite a few. In the field of image processing, it has been used to image enhancement [68] and filtering [69]. Its use in geometry processing has been recently proposed by Sun et al. in [70], [71] for mesh denoising. The first work using random walks in computer vision is in the application of texture discrimination [72], and one reported recently in image segmentation [67].

1.6 Advantages of Random Walk for CMR Image Segmentation

Random Walk is a special case of Markov chain [73], since image is considered as a graph. Unlike a general Markov chain, Random Walk on a graph enjoys the property of time symmetry or reversibility, that means the probabilities to traverse a given path in one direction or the other have a simple connection between them. If the graph is regular, the probabilities are equal.

A practical interactive segmentation algorithm must provide four qualities: 1) Fast computation, 2) Fast editing, 3) An ability to produce an arbitrary segmentation with enough interaction,

and 4) Intuitive segmentations. The Random Walk approach introduced here exhibits all of these desired qualities. The concept of Random Walk originates from the physical and mathematical model of Brownian motion. It is the formalization of the intuitive idea of taking successive steps in random directions, like a molecule traveling in a liquid or gas. Grady [67] successfully transferred this idea to the field of image segmentation. For this purpose he transforms the image into an undirected weighted graph $G = (Nodes, Edges)$. So the Random Walk segmentation is based on graph theory. Seed points are used to indicate different objects and the method returns a probability map for each seeded region.

In contrast to several popular image segmentation algorithms (e.g., [74]), the Random Walk based segmentation approach is not derived explicitly from an image model. However, an implicit image model exists in the approach and it is therefore useful to examine the algorithm from this standpoint. In a clinical CMR data-set:

- The images are corrupted with noise;
- Neighboring (touching) objects may have the same value, resulting in low-contrast or absent boundaries; and
- Ambiguity exists when there are more piecewise constant regions than seed groups (labels) in the image.

The Random Walk approach may be viewed as a proposal to address these issues.

Noise has been a prime obstacle against any image segmentation. The assumption, "noise can only be Gaussian" may lead to a 60 percent less noise power underestimation [8]. Therefore, a robust algorithm is always desired, which can perform well despite the presence of high noise level. Some fine pieces of work [75], [67] suggest the robustness of Random Walk approach in these circumstances. Additionally, its faster performing characteristic towards segmentation reported by Grady [67] has multiplied our motivation to use this as the prime tool in our work.

1.7 Motivation and Organization of the Thesis

Usually Random Walk approach produces a very good result on clean images, as can be observed in [67]. The term "clean" here is used to convey the readers that the objects to be segmented are homogeneous and well distinct. On the other hand, the approach on ischemic CMR images

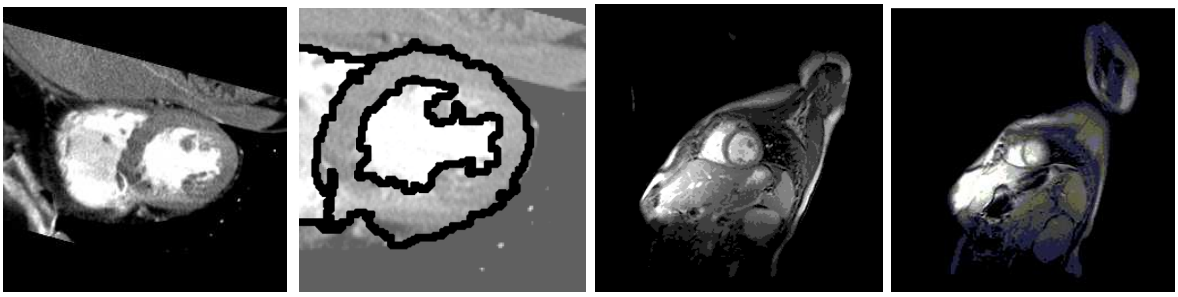

(a) (b) (c) (d)

Figure 1.3: (a) Original image. (b) Segmented image using random walks where LV is homogeneous (courtesy: Grady, 2006). (c) and (d) Real ischemic CMR images.

confronts many challenges if we consider their intensity distribution. These are elaborated in the following subsection.

1.7.1 Motivation

Many algorithms have been introduced to remove observer variation and improve time efficiency, but full automation in segmenting the LV with sufficient accuracy has yet to be achieved. Traditional segmentation algorithms use thresholding, region-growing, edge-detection, and clustering. Since each of these algorithms mostly requires significant user interaction to segment the LV, they have been combined with other segmentation techniques in hybrid schemes to minimize user intervention. Such hybrid algorithms, however, have several limitations: 1) They are reliable for mid-ventricular slices, but they generally fail at the basal and apical slices; and 2) They do not accurately segment the detailed structure of papillary muscles. Methods do exist that are more general and can be applied to a variety of data. However, methods that are specialized to particular applications can often achieve better performance by taking into account prior knowledge. Selection of an appropriate approach to a segmentation problem can therefore be a difficult dilemma. Although under the present scenario, most of the algorithms provide good performance, still there is a lot more to be improved mainly with respect to noise, input image type, and computation. Unlike other existing algorithms, utilization of random walks reduces the dilemma and fulfills the main objective to a larger extent. This method can segment all the objects when they are homogeneous (Figure 1.3(a), if there is only one object of interest) and significantly increases the performance when they are well separate (Figure 1.3(b)). In this context, objects in ischemic (some kind of disease) CMR images are neither homogeneous nor well

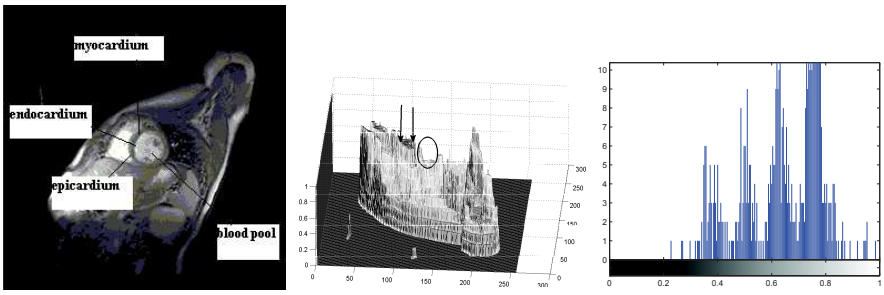

(a) (b) (c)

Figure 1.4: (a) Features in a CMR image. (b) Demarcation of left ventricle (marked as ellipse) from the rest (including right ventricle, epicardium etc.) of the CMR image (Figure (a)). (c) Histogram of the image shown in Figure 1.3(d).

distinct (Figure 1.3(c) and 1.3(d)).

Different features of interest (viz., endocardium, epicardium, blood pool, etc.) in a CMR image are shown in Figure 1.4(a). The muscular walls of the heart consist of three major "layers". The bulk of the walls is made up of a layer of cardiac muscle and is called the myocardium. The muscle is enclosed on the outside by the epicardium and on the inside by the endocardium. The difficulty arisen in distinguishing two adjacent objects is shown in Figure 1.4(b), where the intensity values in each region minutely differ from each other. The histogram (Figure 1.4(c)) clearly indicates the presence of more than one intensity region in the object (right ventricle is more clean as compared to LV) itself. From these discussions, the approach (directly without any modification) seems to fall short in achieving a proper segmentation in such conditions. In addition, complex cardiac structures such as papillary muscles make the approach difficult to accurately trace the LV margins in detail, because these features make the LV non-homogeneous further. from this view point, this thesis presents an attempt to modify the approach to get accurate segmentation of CMR images.

1.7.2 Thesis Contributions

The aim of this research work is to investigate whether building a haptically enabled medical image segmentation environment can notably improve the overall process of image segmentation. The project is split up into a set of objectives, the results of which collectively will help verify and validate the hypothesis. The objectives are:

Endocardium Extraction- Random Walk approach is utilized for blood pool/endocardial

boundary extraction. Various aspects under consideration are:

- Proposed strategy for seeds' placement using superposition theorem.
  - Superposition concept draws a single boundary on a multi-labeled object.
  - Without this concept, undesired multiple object boundaries are drawn within a multi-labeled object.
- Proposed method for seeds' selection using:
  - Heat equation;
  - Cantilever beam equation; and
  - Bending moment equation.
    These operations, along with a threshold technique, mark the locations where a change in intensity occurs (blood pool-myocardium boundary).
- Reduction of seeds to the number of labels.
  - Usually, blood pool of a LV in an ischemic CMR image is not homogeneous and furthermore, it contains many small regions of different intensities. Therefore, this scheme retains only required number of seeds such that each region contains a seed.
- β (free parameter in the approach) selection.
  - Manual selection of the value for β introduces variability in the result. Therefore, in order to avoid this, value of β is determined from the input image.

Epicardium Extraction- A proposed active contour model is used to extract the epicardial boundary that takes the blood pool boundary as its initial contour. It includes:

- Proposed method for object selection; and
- Modified active contour model.

Weighting Functions- Edge weights are the mirror of similarity between two pixels that are connected by the edge. The greater are the edge weights, better is the segmentation. The following functions are newly introduced in the above approach, they are:

- Difference of Gaussian (DoG);

- Difference of Laplacian of Gaussian (DoLoG); and
- Laplacian of Derivative of Gaussian (LoDroG).

Quantitative Evaluation of Segmentation Due to Different Weighting Functions- Some existing evaluation techniques are employed to determine the efficiency of the segmentation obtained due to various proposed weighting functions. In addition, a method is proposed that compares two different methods of segmentation.

All of these objectives are tightly linked. Therefore, they must be seen as a whole, and the fulfillment of each of them will contribute to the overall aim of the project.

The organization of this thesis is as follows:

- Chapter 2 presents in detail the background knowledge required to undertake endocardial wall detection: a review of existing segmentation techniques and a proposed approach.
- Chapter 3 presents in detail the background knowledge required to undertake epicardial wall detection: a review of existing segmentation techniques and a proposed approach.
- Chapter 4 elaborates in detail the background knowledge of weighting function in Random Walk approach and comparison among different suggested weighting functions required for a perfect segmentation.
- Chapter 5 presents the quantitative evaluation of all the the segmentation techniques discussed earlier and a proposed segmentation comparison method.
- Chapter 6 concludes the thesis with some tracks for future work.

Chapter 2

Random Walk Based Endocardial Wall Extraction

Random walk approach is based on graph theory [76]. In this approach, given a graph and a starting node, one selects one of its neighbors at random and moves to this neighbor. Then a new neighbor of this new node is selected at random and the walker moves to it. This procedure continues. The sequence of nodes selected randomly in this way is a Random Walk on the graph. In this work, image segmentation is performed on a graph (i.e. image) whose nodes are the input points (i.e. pixels), and whose links represent the connectivity between them. The chance to move from a vertex to its adjacent neighbor through an edge depends on the weight of the edge.

In this chapter, following a description on Random Walk, proposed methods for 1) placement of seeds, 2) selection of seeds and 3) determination of parameter β (needed in the process to achieve a meaningful image segmentation) are discussed.

2.1 Random Walk for Image Segmentation

When applied on an image, initially, seeds are required to be placed on different labels (homogeneous regions to be segmented) so that at least one seed must be defined for each region. If there are K number of seeds, there will a K-tuple probability vector for each pixel, given a random walker starting at this location. A final segmentation is derived from these K-tuples by selecting for each pixel the most probable seed destination for the random walker. Conceptually, the method works in the following manner:

- An image I is considered to have a similarity function w_{ij} between all pairs of pixels

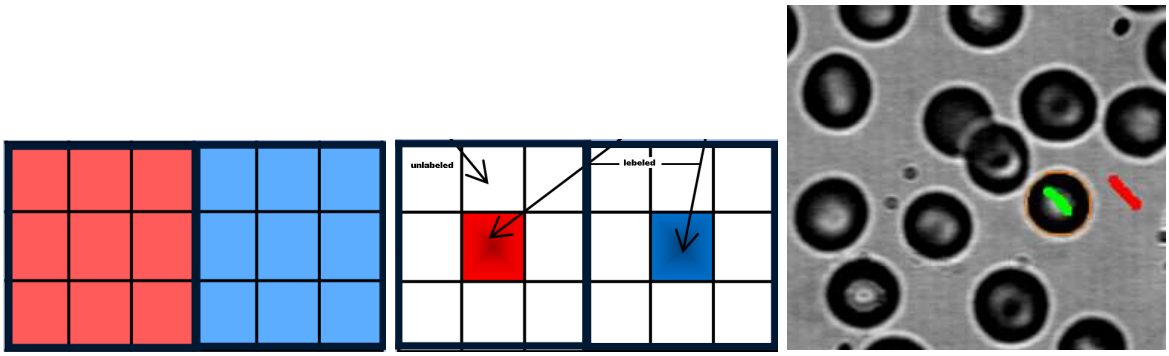

(a) (b) (c)

Figure 2.1: (a) A two-region image. (b) User-defined seeds for each region. (c) A similar image.

$(i, j) \in I$.

- I is represented as a graph, $G = (V, E)$; where V and E represent the set of vertices and edges, respectively. Additionally,
  - pixels are the nodes of the graph.
  - w_{ij} is the weight of the edge between nodes i and j.
  - degree of node i is $d_i = \sum_{j \in N_i} w_{ij}$, where N_i = neighborhood nodes of i.
  - weighting function helps in grouping all connected homogeneous pixels. It is a function of x, roughly defined as,

$$w = f(x) \tag{2.1.1}$$

    where x indicates the pixel intensity.

- Let the image consists of only two regions (shown in Figure 2.1(a) and 2.1(c)), where each region is marked separately by a seed point as shown in Figure 2.1(b). The equivalent 4-connected lattice topology and undirected weighted graph of the image (Figure 2.1(c)) are shown in Figure 2.2(b) and Figure 2.2(c), respectively.

- Pixels are grouped as distinct nodes as shown in Figure 2.2(a).

- Considering the image as an electric resistive circuit (shown in Figure 2.3(a)), one has to calculate the probability that a random walker starting at an unseeded pixel x first reaches a seed with label red, when that seed is at unit potential (shown in Figure 2.3(c)). The same procedure is applied for the other seed also (shown in Figure 2.3(b)).

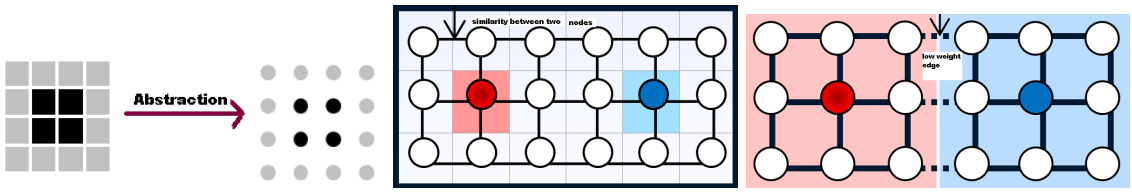

(a) (b) (c)

Figure 2.2: (a) Nodes identification from the image. (b) A 4-connected lattice topology. (c) An undirected weighted graph.

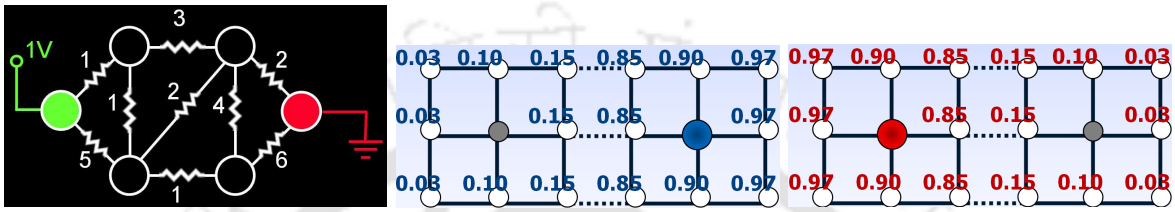

(a) (b) (c)

Figure 2.3: (a) Equivalent electric network. (b) Different probability values that a random walker starting from each unseeded node first reaches blue seed. (c) Different probability values that a random walker starting from each unseeded node first reaches the red seed.

- Each pixel is labeled with the most probable seed destination.

The probability a random walker first reaches a seed point exactly equals the solution to the Dirichlet problem [77]. The process works with boundary conditions at the locations of the seed points. If only one object is to be segmented then the user will have to assign two seed points (as shown in the above example), one on the object while the other at elsewhere in the image. The seed point on the object is fixed to unity while the other is kept at zero and then the sources are interchanged. The distribution of electric potentials on the nodes gives the solution to the combinatorial Dirichlet problem. The resistors and voltage sources (by fixing the electric potential at the seeds) represent the inverse of the weights and the "boundary conditions", respectively. While implementing on an image, one has to calculate the probability, that a random walker starting at a given pixel (node) first reaches a seed with unit probability (potential). This is obtained by solving the equivalent electric circuit to get the potential values at different nodes and the procedure corresponds to a combinatorial Dirichlet problem. The set of maximum probable pixels in the image that reach the seed first, constitute the object boundary. Suppose there are K number of seeds initially (means $K-1$ regions to be segmented), this entire process is repeated for all the remaining seeds to obtain the other object boundaries.

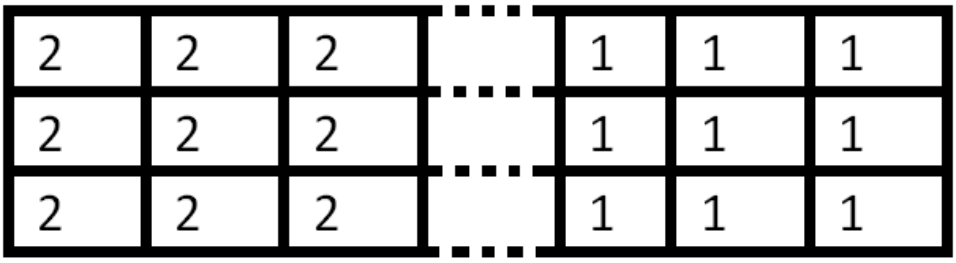

Figure 2.4: Image shown in Figure 2.1(c) in form of 1s and 2s.

We use $pixel$ to refer to the basic picture element and $node$ to graph theoretical discussions and interchange in this thesis according to the requirement.

2.1.1 Methodological Analysis

The probability that a random walker starting at a given unlabeled pixel will first reach a pixel of a particular label is computed by solving the Dirichlet problem. A Dirichlet problem is the problem of finding a harmonic function which solves a specified partial differential equation in the interior of a given region, that takes prescribed values of the boundary of the region. The harmonic function that satisfies the boundary conditions minimizes the Dirichlet integral.

A Dirichlet integral is defined as

$$D[a] = \frac{1}{2}\int_{\Omega} |\nabla a|^2 \, d\Omega \tag{2.1.2}$$

,

where a is the field, and Ω is the region. The field a is the twice differentiable boundary condition on $\partial\Omega$ and region is the domain Ω of $\mathbb{R}^n$. In the meantime, a harmonic function is a function that satisfies the Laplace equation

$$\nabla^2 a = 0 \tag{2.1.3}$$

In case of the Random Walk algorithm, the Laplacian matrix is used to model the relationship between each of the nodes on the graph. This matrix is then used to model the harmonic function that satisfies the boundary condition and in solving the Dirichlet problem. Referring to Figure 2.3(a), the edge weights model the influence of nodes upon each-other. They are stored in a Laplacian matrix, a matrix representation of the relationship between the nodes, along with a diagonal band containing the degree (number of edges incident on the node) of each node. The

0	0	nz		0	0	0
0	0	nz		0	0	0
0	0	nz		0	0	0

Figure 2.5: Gradient of the mask in Figure 2.4.

matrix is defined as

$$L_{ij} = \begin{cases} d_i, & \text{if } i = j \\ -w_{ij}, & \text{if } i \text{ and } j \text{ are adjacent} \\ 0, & \text{otherwise} \end{cases} \tag{2.1.4}$$

The steady state potential at each node (in Figure 2.3(b) and 2.3(c)) represents a probability of the node belonging to a particular label. To get the probability (potential) of each node, the linear system is solved once per label with the seed nodes of other labels grounded (i.e. the potentials of other seed nodes are fixed to zero). The node that gives the maximum probability to a particular label belongs to that label. In this way, all the nodes are assigned to various defined labels.

Once the Laplacian matrices have been obtained, the probabilities may be computed using standard linear algebra. The sequence of steps followed by the algorithm is:

- Input: The seed points are set on different labels in the image.
- Laplacian matrix is built based on the computed edge weights.
- The Laplacian matrix is partitioned, $L = \begin{pmatrix} L_m & B \\ B^T & L_u \end{pmatrix}$. Subscript m and u stand for marked (labeled) and unmarked (unlabeled) pixels, respectively. The B matrix is part of the Laplacian matrix corresponding to the labels.
- The linear system is set up, $L_u X = -B^T m$

  L_u: Edge weights for the unlabeled pixels,

  m : Set of labels for the seed points,

  B^T: Edge weights corresponding to the labels, and

  X : the probability for each pixel being a member of the labels.
- Finally, the linear system is to be solved to get X.

- The most probable pixels now are marked with label numbers. For example in Figure 2.1(c), there are only two labels, i.e. blue→1 and red→2. So the image becomes a mask of ones and twos as shown in Figure 2.4.

- Now, gradient of the image is taken which results non zero values at the intensity transition (as shown in Figure 2.5). The locations of these non zero (marked as nz in the figure) values are the object boundary pixel indices.

Using the probability obtained by solving the system of linear equations, each pixel in the image is then assigned to its corresponding labels for which it has the highest probability.

2.2 Proposed Modification for Seeds Placement

The first and foremost concern of the Random Walk based segmentation lies on the fact that the objects to be segmented in an image should be homogeneous and well separated. The images deviated from this discipline (regarding objects) may not produce an expected result. There are many difficulties while dealing with CMR images that are obtained from patients (popularly known as ischemic CMR images). In this work, since we restrict ourselves to the left ventricle (LV) only, the problems associated with LV in CMR image are briefly summarized as follows:

1. The demarcation between blood pool and the myocardium is not sharp in cardiac apex and basal slices. To carry out an accurate study, we should not limit evaluating the performance within the mid slices. In case of ischemic CMR images, this characteristic is seen in the mid slices also.

2. Comparatively, blood region in a CMR image is learnt to be homogeneous and well distinct from the myocardium. When tissues in cardiac muscles get adversely affected for a long time (in diseases like hypoglycemia, atherosclerosis, thromboembolism, etc.), they attack the adjacent tissues and make them inactive gradually. This action changes the corresponding pixel intensities to blackish. Overall, it accounts to an increased deviation from the homogeneity and well separability.

3. Noise also is a prominent obstacle in getting an appropriate segmentation.

CMR data used in this experiment have been obtained from a diagnostic hospital in Toronto. In most of these ischemic CMR images, blood pool region is quite indistinguishable from its

Table 2.1: Correlation among different pixels near the LV boundary

Sl. No.	*Sample correlation coefficients*					
1	0.978	.977	1	.977	1	1
2	.988	.988	1	.956	1	1
3	.991	.992	.992	.955	1	1
4	.993	.993	.993	.956	1	1

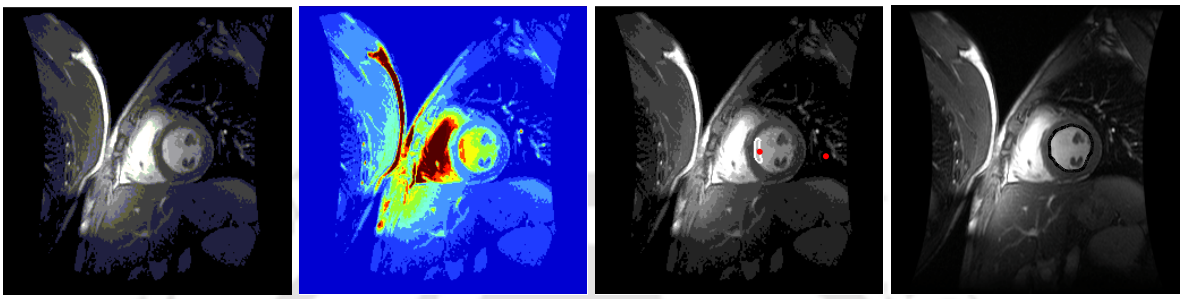

(a) (b) (c) (d)

Figure 2.6: (a) Original image. (b) Equivalent color mapped image of figure in (a). (c) Wrong LV contour extraction from the Random Walk approach with inappropriate selection of seed. (d) Ground truth image of figure shown in (a).

myocardium. The intensity gradually varies from the mid region of blood pool towards the endocardium. For instance, Table 2.1 shows correlation (sample correlation or Pearson's coefficient [78]) among the pixels nearby blood pool-myocardium boundary of an image. The strong correlation among the pixels, indicates the difficulty in distinguishing them through naked eye and placing a seed for the entire blood pool label. If at all we place a seed irrespective of the intensity distribution, a pseudo contour may be extracted. This is illustrated in Figure 2.6. Suppose the user accidentally places the initial seed point on the region marked pink (left end inside LV) in the blood pool as shown in Figure 2.6(b). Due to the characteristics of Random Walk, only segmentation of the pink region is obvious (shown in Figure 2.6(c)). Of course this result is undesirable if we examine the determined border with the ground truth image (shown in Figure 2.6(d)). The main reason of getting such an undesired contour is due to the presence of a number of small labels in the blood pool region. This type of CMR slices can be said to have multi-labeled LV image. Therefore instead of putting just one seed point on the blood pool label, we modify the strategy and place more number of seeds as many different small labels/sub-labels inside the blood pool are present.

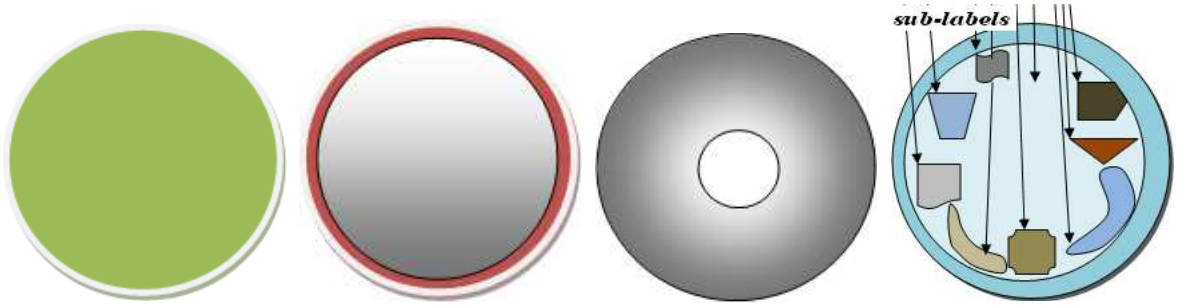

(a) (b) (c) (d)

Figure 2.7: (a) Only one homogeneous label. (b,c) Intensity varies gradually. (d) Multi-labeled image.

Figure 2.7 illustrates different possible cases with respect to intensity in an object. Figure 2.7(a) shows the presence of only one label in the object, where the Random Walk algorithm is reported to perform properly [67]. On the other hand, when the label is not well defined in terms of homogeneity (as shown in Figure 2.7(b)), a wrong contour is resulted by the algorithm (as shown in Figure 2.7(c)). Figure 2.7(d) shows the presence of various small labels in an image similar to the above described CMR image. While applying Random Walk approach, these sub-labels should be individually allocated by one seed each in order to get a meaningful segmentation, assuming all the sub-labels are at unity potential. Then the potential of all the nodes are obtained by applying superposition theorem [79]. In a similar manner, pixels corresponding to the nodes having maximum potential constitute the boundary.

Of course, placing many seeds reduces the risk of missing any sub-label, but on the other hand, it increases the computational cost. Therefore, precise number of seed points must be desirable. In addition, performance of this method depends on the weighting function, in directly on parameter β. The inappropriate selection of β also leads to a pseudo contour extraction. These facts are individually verified as shown in Figure 2.11. The main objective of this chapter is to minimize these problems simultaneously by: 1) deciding the required number of seeds and placing them at appropriate locations, and 2) selecting a suitable β from the image itself instead of doing manually.

2.3 Proposed Method for Seeds Selection

Since a long time, heat equation has been in use in different fields like mechanics, thermodynamics, etc. We have strived to find various sub-labels present (if any) in the blood pool region

with the help of this equation. The motivation in taking the help of this equation is to convert the pixel values in to a large scale so that it will be convenient while judging different sub-labels in the blood pool region by their pixel values. For completeness of the paper, its mathematical formulation is given briefly. For details, the interested readers are suggested to go through [80], [81].

The traditional heat equation is given as:

$$\frac{\partial u}{\partial t} = \frac{\partial^2 u}{\partial x^2} \tag{2.3.1}$$

where temperature u is a function of position x and time t.

Let us consider a hypothetical thin (of one particle width i.e., one dimensional) iron rod consisting of particles that have different conductivity values. On application of heat, it gives different amplitudes of heat at different positions. In this experiment, image pixels are assumed to have a direct relation with the rod particles in the following manner: higher the intensity value of a pixel towards one, lower is the corresponding particle temperature, and lower the intensity value of a pixel towards zero, higher is the corresponding particle temperature. The term particle and pixel will be interchanged while describing the mode of operation. Usually, heat equation with non-homogeneous boundary conditions is applied at the edges of the object [39]. On the other hand, non-homogeneous differential equations are difficult to solve. In this case, the homogeneous form is developed by assuming that with an infinity rise in time, the magnitude of temperature at a position becomes constant. The proposed algorithm works as follows:

1. Choose a point (b_0, g_0) anywhere in the blood pool region (preferably in the center region).

2. Place the iron rod U of length (L) on the CMR image, whose one end is hinged at (b_0, g_0). Initially U is considered of two pixel long, i.e. L equals to two pixels. The rod is assumed to contain the image pixels lying under the rod, i.e. $U = \bigcup_{i=0,j=0}^{L} V(b_i, g_j)$. The length of the rod taken at subsequent instants, gradually increases from two particles to such an extent that it covers the whole blood pool region.

3. In the next step, heat is applied on the rod and it is obvious that the temperature varies with position (shown in Figure 2.8(a)) along the rod as different positions are occupied by particles of different conductivities. The mean temperature is recorded. To make the point more clear;

   - first, consider the rod length of two pixels;

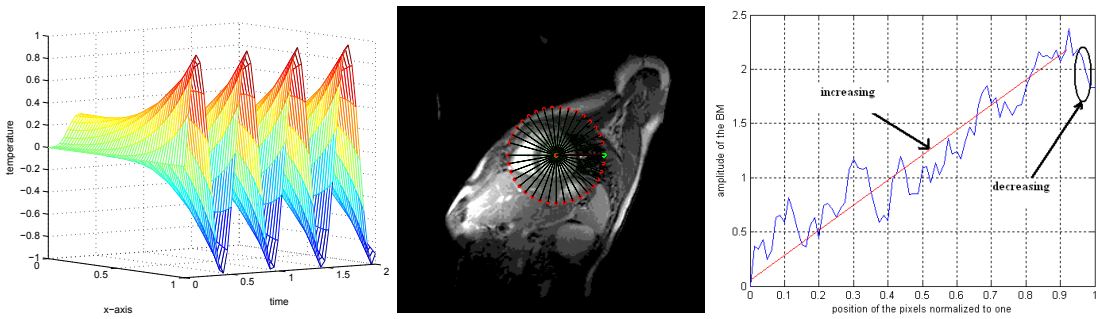

(a) (b) (c)

Figure 2.8: (a) Temperature profile obtained due to the pixels under the rod up to a certain position on the rod for a certain orientation.(b) Rod in different orientations form the wheel. (c) Temperature amplitude profile due to all the pixels on the rod.

- the rod is subjected to heat, the average temperature for that level of heat is recorded;
- increase the length by one more subsequent pixel and note down the temperature magnitude; and
- follow the above steps until the length L is covered. The temperature profile (of the average temperatures) is shown in the Figure 2.8(c). In this way, a high scale amplitude scale is created.

4. Check the position, where there is a significant change in the magnitude. This position should correspond to a point at the boundary between blood pool and the myocardium. A threshold technique is employed to get the position (we call the pixel corresponding to this position as the *stopping pixel* with co-ordinates (b_{stop}, g_{stop})). The stopping pixel is considered to belong to the blood pool label (Ł), i.e. $U(b_{stop}, g_{stop}) \in E$, where $E = \bigcup_{i,j \in Ł} V(b_i, g_j)$.
5. Rotate the rod in clockwise direction through 360 degree by a small angle (as shown in Figure 2.8(b)). Repeat the steps (1-4) at each orientation to extract all the stopping pixels. This set of pixels is taken into the consideration as initial seeds required in the process of segmentation using Random Walk.

The following subsection briefly elaborates the heat equation for a single orientation of the rod.

2.3.1 Heat Conduction Through the Rod

The geometric sinusoidal function for the calculation of heat amplitude is chosen for its monotonic increment nature in [0,π/2]. The detailed mathematical discussion is provided in [80]. In order to introduce homogeneous boundary conditions to the general boundary value problem, it is assumed that when time $t \rightarrow \infty$, the temperature in the rod does not depend on t. Using the boundary conditions in association with the method of separation of variables, we get the solution of heat equation as:

$$u\left(x,t\right) = v(x,t) + R\left(x,t\right) \tag{2.3.2}$$

where $u\left(x,t\right)$ represents the conductivity at the position x and time t. The homogeneous part is given by:

$$v\left(x,t\right) = \sum_{n=1}^{\infty} f\left(x\right) e^{c^2}\lambda_n t \tag{2.3.3}$$

$$f\left(x\right) = \Im\left[\frac{\cos\phi x}{\cos\phi}\right] \tag{2.3.4}$$

where $\phi = \sqrt{-j\omega}$ and the non-homogeneous part is given by:

$$R\left(x,t\right) = \Im\left[\frac{\cos\phi x}{\cos\phi} e^{i\omega t}\right] \tag{2.3.5}$$

The frequency ω depends on the positional amplitudes in the rod and diffusion coefficient c is supposed to be unity.

Now the next immediate step is to find the location where a significant change in conductivity in the rod appears. This helps in obtaining the *stopping pixel* in the LV image. Dynamic statistical parameters are used for estimating the threshold that separates two regions. Boribhoje et al. [82] have reported such a technique based on intensity. The dynamic statistical parameters, described in the following subsection, set a low threshold value for high intensity region and a high threshold value for low intensity region. In addition, a change detection technique [83] is used to estimate the position, where the change in intensity occurs. Both methods are combined together forming an adaptive technique to obtain the stopping pixels.

2.3.2 Adaptive Threshold Technique

As discussed in Section 2.3, a one dimensional (1D) vector is assumed to contain the values of the particles. In order to discriminate the particles owing to different regions, the individual

dynamic statistical parameters viz., mean, standard deviation (σ) and third moment (M) of all the particles are calculated.

The new particles encountered in the vector update the statistical parameters automatically indicating the change in regions. After each sample particle, a deciding function DF_f is calculated using the following formula:

$$ß_f = k_1 (\sigma_f + M_f) \tag{2.3.6}$$

The quantity defined above with subscript f gives the value of f_{th} particle. Threshold (E) is updated continuously on the basis of the deciding function and calculated using the following formula:

$$E_f = E_{f-1} - k_2 (ß_f - ß_{f-1}) E_{f-1} \tag{2.3.7}$$

where constants k_1, k_2 are determined empirically. In this way, we get as many threshold values as the number of particles are present. In order to confirm the correct threshold value at the desired location, a suitable change detection technique is applied. There are many such techniques [83–86] available to date. In the present problem, we have preferred CUSUM (cumulative sum) [83] over other approaches. It traps the position of a significant change in amplitude. The stopping particle is given by:

$$X = \min \{f : d_f \geq j\}$$

and

$$X = \min \{f : D_f \geq r_f + j\} \tag{2.3.8}$$

where D_f is the log likelihood function and $r_f = \min_{1 \leq l \leq f} D_l$. CUSUM is a comparison between cumulative sum and adaptive threshold, $r_f + j$. The threshold obtained from Equation 2.3.7 is compared with the adjacent values to deny any deviation of X from the actual position. Now, the particle corresponding to both threshold value and X is the *stopping particle*. The pixel corresponding to the stopping particle is the *stopping pixel*. This process is repeated for all the orientations. Connecting all the stopping pixels, a closed contour is obtained as shown in Figure 2.9.

Usually, less number of seeds reduce the computational complexity to a reasonable range. On the other hand, if we use smaller number of seeds than the required number, then it leads to an inaccurate output (which is shown in the next chapter). The excess number of seeds increases

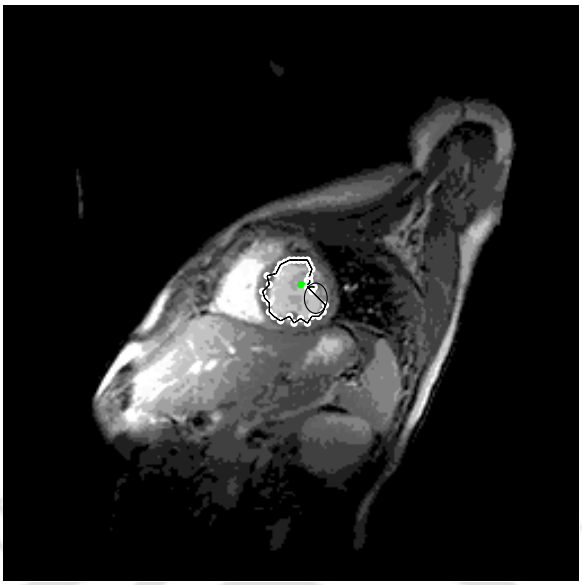

Figure 2.9: Missing of some pixels in LV contour with direct thresholding.

the complexity. In the following subsection, The effect of the number of seeds on computation is discussed.

2.3.3 Effect of Larger Number of Seeds on Computation

Conceptually on a graph, the wieghting function (random walker) depends on the spatial distance as well as node values [87]. The computational cost of a walker to reach a particular node (i.e. a seed) depends on the distance and resistance it confronts. In order to achieve one segmentation, if the same operation is performed several times as many seeds are present, obviously, the computational cost increases. An attempt has been made to present this in the following manner.

Consider a sum of N_s 2D vectors with random orientations with the plane of each vector be random. Assume N_s unit steps are taken in an arbitrary direction (with angle θ uniformly distributed in the range [0,2π]). The position z in the complex plane after N_s steps is given by:

$$z = \sum_{j=1}^{N_s} e^{i\theta_j} \tag{2.3.9}$$

$$|z| = N_s + \sum_{\substack{j,k=1 \\ j \neq k}}^{N_s} e^{i(\theta_j + \theta_k)} \tag{2.3.10}$$

Therefore,

$$\left\langle |z|^2 \right\rangle = N_s + \left\langle \sum_{\substack{j,k=1 \\ j \neq k}}^{N_s} e^{i(\theta_j + \theta_k)} \right\rangle \tag{2.3.11}$$

θ_j and θ_k are random variables with identical means of zero. Averaging over this distribution, second part of Equation 2.3.11 becomes zero. So,

$$\left\langle |z|^2 \right\rangle = N_s$$

and the root mean square distance after N_s unit steps is given by:

$$|z|_{rms} = \sqrt{N_s} \tag{2.3.12}$$

With step size l,

$$d_{rms} = l\sqrt{N_s} \tag{2.3.13}$$

In order to travel a distance d, the random walker requires N number of steps which is given by

$$N \simeq \left(\frac{d}{l}\right)^2. \tag{2.3.14}$$

This derivation clearly indicates the requirement of more resources (e.g. computation time), when a random walker moves to more number of seeds. To compensate this, we use a simple discarding scheme to choose a minimum but sufficient number of seeds from the set of initial seeds obtained in Section 2.3. First, any two consecutive seeds from the set are picked. One of these seeds is kept fixed and the second seed's intensity is compared with it. If both are found to be same, the second seed is discarded from the set. This procedure is carried out for remaining seeds in the set one after another. The resulting seeds obtained from this procedure on two CMR slices are shown in Figure 2.10(b) and 2.10(d).

Next step is to apply Random Walk on the image assuming all the sub-labels are occupied by these seeds. There are many papers reporting this method in the literature, but we restrict ourselves to the one reported in [67] which is known to yield an optimal solution. Apart from seed selection and placement, the weighting function in the approach plays a pivotal role in the process of segmentation. Therefore, its relation with CMR image must be drawn out.

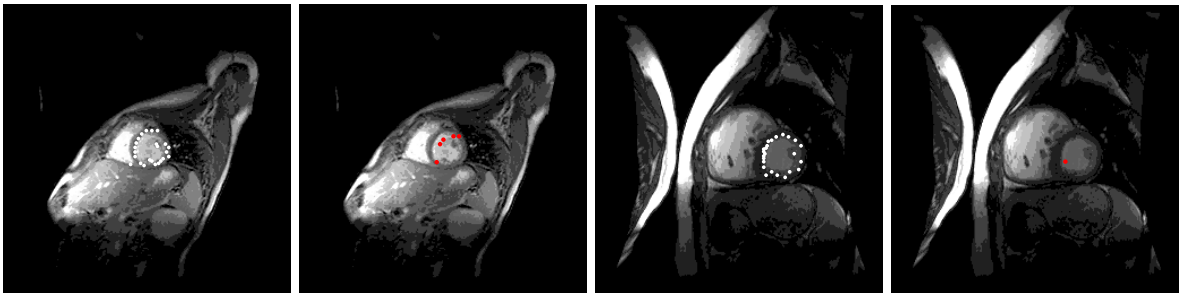

(a) (b) (c) (d)

Figure 2.10: (a,c) All seeds obtained from the adaptive thresholding. (b,d) Resulted seeds due to the discarding scheme.

2.4 Weighting Function in Random Walk Approach

In this approach, the image pixels are represented by random walker biases. These biases are edge weights and a map is defined for a pair of pixel intensities to an edge weight. The following weighting function [67] has been referred while segmenting the images where objects are homogeneous and well distinct:

$$w_{ij} = e^{-\beta(H_u - H_v)^2} \tag{2.4.1}$$

H_u and H_v indicate the image intensity at pixel u and v, respectively. The parameter, β, present in this method is decided by the user. For each label Ł, the respective contour is obtained from the solution to the Dirichlet problem as: $J_{un}\, x^{Ł} = -V^T ç^{Ł}$. Thereby J_{un} is the Laplacian matrix of the unseeded nodes $x^{Ł}$, $ç^{Ł}$ represents the seeded nodes, and V^T the corresponding Laplacian matrix.

Manual selection of parameter β (used in the weighting function in determining the adjacency matrix) introduces variability in the segmentation performance (as shown in Figure 2.11). In order to avoid this, a procedure is suggested for computing β from the input image. Let us discuss the influence of β on the performance of the algorithm and subsequently its estimation.

2.5 Dependency of Random Walk Approach Performance on β

Here the input image is considered as a weighted graph. In graph G, a walk is a sequence of vertices $(q_0, q_1 ... q_s)$ with $\{q_{i-1}, q_i\} \in Q\,(G)$ for all $1 \leq i \leq s$, and Q represents the set of edges.

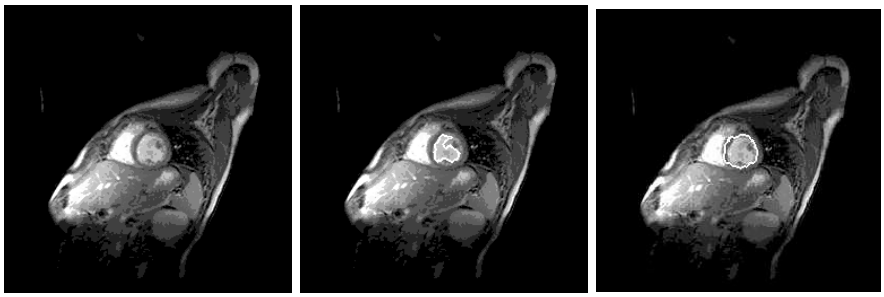

(a) (b) (c)

Figure 2.11: (a) Original image. (b,c) Segmentation due to improper β selection.

A Random Walk is determined by the transition probabilities $P(c,q) = prob(x_{i+1} = q | x_i = c)$, which are independent of i [76]. Clearly for each vertex c,

$$\sum_q P(c,q) = 1 \tag{2.5.1}$$

It should be noted that each vertex corresponds to a pixel. For any initial distribution $f : B \to \mathbb{R}$ with $\sum_q f(q) = 1$, the distribution after s steps is fP^s. The Random Walk should be ergodic and this happens when there is a unique stationary distribution $\pi(q)$ satisfying

$$\lim_{s\to\infty} fP^s(q) = \pi(q) \tag{2.5.2}$$

Necessary conditions for the ergodicity of P are [76]:

- irreducibility, for any $c, q \in B$, there exists s such that $P^s(c,q) > 0$, B represents the set of vertices.
- aperiodicity, $\{s : P^s(c,q) > 0\} = 1$.

The transition probabilities of a Random Walk on a weighted graph is given by:

$$P(c,q) = \frac{W(c,q)}{d_c} \tag{2.5.3}$$

where $d_c = \sum_z W(c,z)$ is the (weighted) degree of c. The two conditions for the ergodicity are equivalent to the condition that the graph be 1) connected and 2) non-bipartite, which is the case. A strong notion of convergence that is often used is measured by the Relative Point-wise Distance (RPD). After s steps, the RPD of P to the $\pi(c)$ is

$$\Delta(s) = \max_{c,q} \frac{|P(q,c) - \pi(c)|}{\pi(c)} \tag{2.5.4}$$

From the above equation

$$\Delta(s) \leq e^{-s(1-\overline{\lambda})} \frac{\text{vol}\, G}{\min_c d_c} \tag{2.5.5}$$

where $vol\, G = \sum_c d_c$ and $\overline{\lambda} = \max_{i \neq 0} |1 - \lambda_i|$, λ_i represents the eigen values of the Laplacian. Therefore, if we choose s such that $s \geq \frac{1}{1-\overline{\lambda}} \log \frac{\text{vol}\, G}{\varepsilon \min_c d_c}$, then after s steps, we will have $\Delta(s) \leq \varepsilon$. Equation 2.5.3 clearly demonstrates the dependency of random walker P on the edge weights and Gaussian weighting function [88] (as defined in Equation 2.4.1). In other words, the performance of the algorithm is reckoned to be much dependent on the value of β. Xianfang et al. report the value of β relies on the noise level in any Rician distributed data [71]. In this work, we take the assistance from [71] to estimate β from the available information in the CMR image itself.

2.6 Method for Selecting β

The Noise Variance (NV) plays an important role in deciding the value for β [71]. Accuracy of NV estimation depends on the region from which it is to be calculated. Presence of noise is assumed to be more prominent in the background or constant signal regions [89]. Various methods (e.g., see [90]) are available to estimate NV. Picking an algorithm is subjective in nature, depending on the type and objective of the algorithm used. When the algorithm is region based, it is a usual practice that the NV is estimated with respect to different small regions. Neglecting the residual component of the original image, different local variances are calculated. These are averaged to get the final variance. One major concern of the method is that it can not be useful for graph cut algorithms. In order to verify the fact, we have estimated the NV using this method and used the resulting variance level for calculation of β. The same β value was used in Figure 2.11(a) that ensued Figure 2.11(b). Figure 2.11(c) is also resulted by an improper value of β. Therefore, the selection of a certain method for variance estimation is crucial from the algorithm's perspective. Sijbers et al. report the background region of any data to be more suitable for NV estimation [90].

The image intensity in CMR images, in the presence of noise is governed by a Rician distribution. The noise distributions are nearly Gaussian for larger signal to noise ratio [8]. The following statistical parameters [90] viz., Mean Square Error (MSE) and Cramer-Rao Lower Bound (CRLB) are used to characterize the selection of region. Two regions, viz. 1) constant

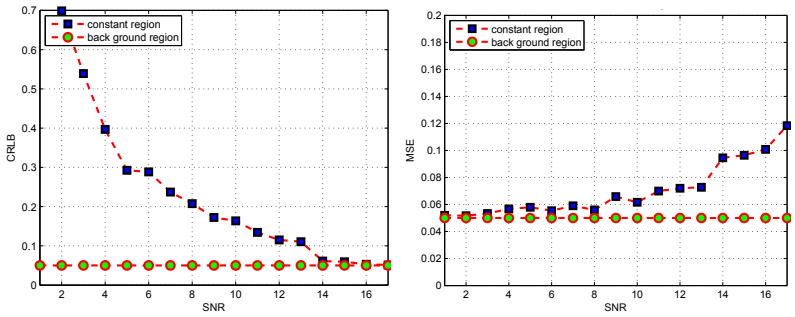

(a) (b)

Figure 2.12: From a set of CMR data (a) Cramer-Rao lower bound and (b) MSE obtained from background and constant region.

region (where the signal is non zero) and 2) background region in the CMR image, are considered for determining NV. In the next subsection, the Maximum Likelihood (ML) approximation of NV from a set of N Rician distributed data points (i_n, where $n = 1....N$) is discussed. The purpose of this is to find out which region is more suitable for NV estimation.

2.6.1 Region of Constant Amplitude

The original image $I\,(b, g)$ may be described by an array of $B \times G$ elements, where B and G are the number of rows and columns in the image. A constant region is obtained by filtering the noisy image [12] by a cascade of two lD difference operators [91], with the domains $D_1, D_2 \subset \mathbb{R} \times \mathbb{R}$ and the range $U \subset \mathbb{N}$. The first difference operation refers to vertical direction and the second to horizontal one, i.e.,

$$\begin{aligned} y_1\,(b, g) &= \frac{1}{\sqrt{2}}\,(y\,(b+1,\ g) - y\,(b,\ g)) \\ &\forall\ \ (b,\ g) \in D_1 \end{aligned} \tag{2.6.1}$$

$$\text{with } D_1 = \left\{ \begin{array}{l} (b, g)\,|b \in [1, B-1]\ \wedge \\ g \in [1, G]\,;\ \ b,\ g,\ B,\ G\ \in \mathbb{N} \end{array} \right\} \text{ and}$$

$$\begin{aligned} y_2\,(b, g) &= \frac{1}{\sqrt{2}}\,(y_1\,(b,\ g+1) - y_1\,(b,\ g)) \\ &\forall\ \ (b,\ g) \in D_2 \end{aligned} \tag{2.6.2}$$

$$\text{with } D_2 = \left\{ \begin{array}{l} (b, g)\,|b \in [1, B-1]\ \wedge \\ g \in [1, G-1]\,;\ \ b,\ g,\ B,\ G\ \in \mathbb{N} \end{array} \right\}.$$

The CRLB for the unbiased estimation of NV σ^2 is given as:

$$CRLB = \frac{1}{\det I}\begin{pmatrix} I(2,2) & -I(2,1) \\ -I(1,2) & I(1,1) \end{pmatrix} \tag{2.6.3}$$

I is the Fisher information matrix and its elements are:

$$I(1,1) = \frac{N}{\sigma^2}\left(Z - \frac{A^2}{\sigma^2}\right)$$

$$I(1,2) = I(2,1) = \frac{NA}{\sigma^2}\left(1 + \frac{A^2}{\sigma^2} - Z\right)$$

$$I(2,2) = \frac{N}{\sigma^4}\left(1 + \frac{A^2}{\sigma^2}(Z-1) - \frac{A^4}{\sigma^4}\right)$$

with matrix

$$Z = E\left[\frac{m^2}{\sigma^2}\frac{I_1^2\left(\frac{Am}{\sigma^2}\right)}{I_0^2\left(\frac{Am}{\sigma^2}\right)}\right]$$

where N, A and m represent the total number of data points that are Rician distributed, underlying signal amplitude of the data and magnitude data points with true parameter (A,σ), respectively. The value of σ^2 can be estimated as:

$$\left(\hat{A}_{ML}, \hat{\sigma^2}_{ML}\right) = \arg\left\{\max_{A,\sigma^2}(C)\right\} \tag{2.6.4}$$

where $\hat{\sigma^2}_{ML}$, $\hat{A}_{ML}$ are the maximization of the log likelihood function with respect to σ^2 and A, respectively, with log likelihood function

$$C = -N\log\sigma^2 - \sum_{n=1}^{N}\frac{i_n^2 + A^2}{2\sigma^2} + \sum_{n=1}^{N}\log I_0\left(\frac{Ai_n}{\sigma^2}\right)$$

It is difficult to solve analytically, so a two dimensional function may be used for optimization.

2.6.2 Background Region

If the data is taken from the background and it is well governed by the Rician distribution, then the CRLB for unbiased estimation of σ^2 is given by:

$$CRLB = \frac{\sigma^4}{N} \tag{2.6.5}$$

The MSE of $\hat{\sigma^2}_{ML}$ is:

$$MSE\left(\hat{\sigma^2}_{ML}\right) = \frac{\sigma^4}{N} \tag{2.6.6}$$

where the maximization of the log likelihood function:

$$\hat{\sigma^2}_{ML} = \frac{1}{2N}\sum_{n=1}^{N} i_n^2 \tag{2.6.7}$$

In this experiment we have calculated CRLB and MSE on the CMR data, which are shown in Figure 2.12(a) and 2.12(b), respectively.

The background region is verified to provide lesser MSE and smaller CRLB as compared to that of a constant region. Therefore, background region is more suitable for NV estimation.

2.6.3 Selection of β

Xianfang et al. report that β depends on the surface normals, obtained from a 3D mesh [71]. It gives a method of updating β based on one face of the mesh which is given by:

$$\beta' = \beta - Y \tag{2.6.8}$$

with

$$Y = \sum_{i \in F} \frac{\mu}{\|\widetilde{n}_i\|^3}\left((n_{io}.\widetilde{n}_i)\left(\widetilde{n}_i.\dot{\widetilde{n}}_i\right) - \left(n_{io}.\dot{\widetilde{n}}_i\right)\|\widetilde{n}_i\|^2\right)$$

where F, n_{io} and n_i are the total faces, initial noisy normal and normal of i_{th} face, respectively. The initial value of μ and β need to be initialized. As we deal with 2D mesh (from 2D CMR slice), there is only a single face. Since direct application of the above method to 2D images is not possible, the input images are triangulated [92] first to transfer into xyz coordinates. To generate the well known Delaunay triangulation, a "divide and conquer" algorithm [93] is implemented. The divide and conquer algorithm only computes the Delaunay triangulation for the convex hull of the point set. The first step is to put all of the points into order of increasing x-coordinates (when two points have the same x-coordinate, their order is determined by their y-coordinates). Once the points are ordered, the ordered set is successively divided into halves until we are left with subsets containing no more than three points. These subsets may be instantly triangulated as a segment in the case of two points and a triangle in the case of three points. From here, the triangulated subsets are recursively "merged" with their former other halves. The final product of

any merge will be a triangulation consisting of edges previously present in the left triangulation, having endpoints from the left subset (LL), edges previously present in the right triangulation, having endpoints from the right subset (RR), and new edges running between the left and right triangulations, having one endpoint from the left subset and one endpoint from the right subset (LR). To maintain Delaunayhood over the merged point subsets, deletion of LL and RR-edges may be necessary. Then the normals obtained are further used in estimating the value for β.

2.6.4 Theoretical Verification

The main objective of this section is to justify the dependency of β on the image pixels.

Property - 1

For a polygon (such as triangle), a surface normal is the vector cross product of two non parallel edges of the polygon. The cross product of any two vectors **A** and **B** is:

$$\mathbf{A} \times \mathbf{B} = |\mathbf{A}|\,|\mathbf{A}| \sin\theta \tag{2.6.9}$$

That means the product directly depends on magnitude of two vectors and if the above two vectors are non parallel then,

$$\mathbf{A} \times \mathbf{B} = |\mathbf{A}|\,|\mathbf{B}| \sin\theta_{\mathbf{u}}$$

where **u** is the unit vector. Therefore in any case, vector cross product depends on magnitudes of the individual vectors and so are the surface normals that directly depend on the elemental values.

The following property tries to outline the direct relation between variance and data points (pixels) in an image. The detailed mathematical verification is presented in the appendix.

Property - 2

For convenience, some of the necessary background and notations are as follows: if ξ is a random variable that is uniformly distributed and F is an arbitrary distribution function (df), then random variable

$$K \equiv F^{-1}(\xi)$$

has df F. When variance of K is finite ($Var[K] < \infty$) Fubini's theorem gives,

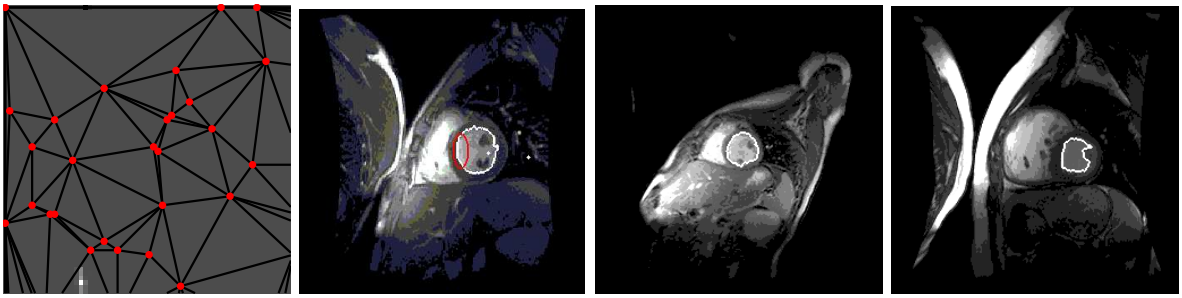

(a) (b) (c) (d)

Figure 2.13: (a) Delaunay triangulation of the back ground of the image used in Figure 2.11(a). (b,c,d) Segmentation on the image used in Figure 2.6(c), 2.11(a) and 2.10(d) from proper seed placement and β selection.

$$Var\left[K\right] = \int_{-\infty}^{\infty}\int_{-\infty}^{\infty}\left[F\left(k\Lambda y\right) - F\left(k\right)F\left(y\right)\right]dkdy \tag{2.6.10}$$

where k and y are two different variables. Already we know that,

$$Var\left[K\right] = \int_{-\infty}^{\infty}\left(k-\mu\right)^2 dF\left(k\right) \tag{2.6.11}$$

where μ is the mean of K. From Equation 7.1.5 (in the Appendix) and 2.6.11, it can be written as:

$$F\left(k\right) \propto k$$

which is verified from the property of distribution function i.e.,

$$F\left(k_1\right) > F\left(k_2\right)$$

for $k_1 > k_2$. Equation 7.1.5 shows the direct relation that exists between variance and associated df while Equation 7.1.6 indicates the relation between df and data points. The detailed analysis is given in the appendix.

From subsection 2.6.3, β seems to be dependent on the normals and the property in subsection 2.6.4 shows the dependency of a normal on data points. Similarly, property in subsection 2.6.4 shows the direct relation of variance on data points. Therefore, β can be said to have a direct relation with the data points or pixels. We have already seen the importance of background region, so the pixels from this region are responsible for estimation of β.

The combined approach is summarized as shown in Figure 2.14.

2.7 Experimental Analysis

Figure 2.15 shows the performance of the proposed algorithm. The results suggest the potential of the approach even in the presence of less homogeneity in the blood pool region. The original CMR images and their corresponding ground truth equivalents are included to have a simultaneous comparison with the determined segmentation. The data set was comprised of short and long axis cardiac MR image sequences acquired from 33 subjects. This was provided by the department of Diagnostic Imaging of the Hospital for Sick Children in Toronto, Canada. The images were scanned with a GE Genesis Signa MR scanner using the FIESTA scan protocol. Some of the subjects had a variety of heart abnormalities such as cardiomyopathy, aortic regurgitation, enlarged ventricles, etc. and a smaller number displayed a left ventricle related abnormality. All the subjects were under the age of 18. Each patient's image sequence consisted of exactly 20 frames and the number of slices acquired along the long and short axes of the subjects ranged between 8-15. Spacing-between-slices ranged between 6mm - 13mm. Each image slice consisted of 256 $\times$ 256 pixels with a pixel-spacing of 0.93mm - 1.64mm. Only grey-scale images were considered in this work. Additionally, we include some images that are derived from the data set, which look like synthetic. The purpose of doing so is to test the efficiency of the proposed algorithms in this thesis on such bad quality images.

In order to find β from the back ground of input image, first the surface normals are calculated. For this, the back ground of the input image is triangulated using the method stated in [94]. The triangulation (as shown in Figure 2.13(a)) scheme has been embedded, so that it can deal with 2D images immediately after they have been transferred into xyz coordinates. A Normal to an edge that is constituted due to two pixels, depends on their true intensity values. Gradient between this pair of pixels provides the values of the resulted normal. After getting all normals, the Equation 2.6.8 is used to get the value of β. The angle of rotation for 1D rod is taken as 15 degree. The selection of angle is optional and can be made even smaller around so that all the sub-labels present around the blood pool boundary could be covered (but computation may slightly be more). The performance will remain more or less unaffected because of the discarding scheme discussed in subsection 2.3.3 that retains the seeds in different labels. The image obtained after direct thresholding is similar to a segmented image (shown in Figure 2.9). The purpose of showing this figure is to point the inability of direct thresholding to achieve a proper segmented image. A straight line joining the two consecutive pixels at the right half of the

segmentation shows some missing pixels at the actual boundary (encircled in Figure 2.9) on the resulting contour.

For completeness of the thesis, a few more results (from the total results obtained from all the subjects) are shown in Figure 2.16. This strategy is adapted in rest of the chapters also. The complexity in blood pool segmentation arises from the level of demarcation (from myocardium) as shown in Figure 2.16. The algorithm faces difficulty when this value is low (as in Figure 2.16(a), 2.16(b), 2.16(g), 2.16(k), 2.16(l), 2.16(m), 2.16(n) and 2.16(o)). Images in Figure (2.16(c), 2.16(d), 2.16(e), 2.16(f), 2.16(h) and 2.16(p)) show a slightly significant demarcation. The effectiveness of our scheme when applied to such images (cardiac apex and basal slices) is evident from these results. Figure 2.13(c) and 2.13(b) reflect the efficiency of this algorithm by taking as minimum seeds as possible for a successful segmentation. When the blood pool is single labeled, one seed (Figure 2.10(d)) is sufficient for a successful segmentation (Figure 2.13(d)), it is also reported by Grady [67]. Figure 2.13(b) shows a better performance if it is compared with Figure 2.6(c). The red marked ellipse in Figure 2.13(b) shows the connected identical pixels adjacent to the initial seed that was defined in Figure 2.6(c).

The CMR images considered in the performance analysis belong to different subjects in the process that cover a full cycle of respiration (a single complete act of breathing in and out). Only a few images from the data set have been included that highlight the demarcation problem. The images having other peculiar characteristic (for example presence of papillary muscles) and the effect of Random Walk on segmentation are shown in the subsequent chapters.

2.8 Conclusions

While heart is one of the most important parts of the human being, the cardiac MR images are very difficult to analyze due to their complex color geometry. Knowledge of better clinical information requires a proper visual inspection. Shear volume of the medical image data requires more automatic segmentation systems to reduce the work load, manual error, etc. by reducing subject variability. The demand towards developing faster, more accurate and automated techniques has motivated us think of this work. In this chapter, the importance of seeds selection and their placement have been discussed. A method using heat equation in association with an adaptive threshold technique for initial seeds selection has been proposed. Also, the use of background region for calculating the algorithm parameter β has been discussed. The salient feature

of our algorithm is its success in multi-labeled LV images with less number of seeds [95].

The computation time is reflected by the cover time [96] of the random walker. Cover time ($\digamma$) is the average time it takes to visit the defined nodes (seeds). As the CMR image has been treated as an undirected weighted graph (electric resistive circuit), for the Random Walk, $\varpi\chi < \digamma < \mathrm{O}(\varpi R \log \varrho)$, where ϖ, ϱ represent number of edges and number of nodes respectively with χ being the maximal equivalent resistance between two nodes of the circuit. This clearly demonstrates that with decrease in number of nodes the cover time decreases. This could happen only when the candidate CMR image is free from any ischemia, i.e. normal. Therefore, the present approach is dependent on the severity of ischemia.

We have also tested with cantilever beam and bending moment equation in the place of heat equation (which are included in the Appendix) and found similar kind of performances [95]. This is because, this operation only provides the small pixel intensity values in a large scale.

The combination of the above strategies successfully segments the blood pool region of LV (endocardial wall) that consists of many sub-labels. Whenever the papillary muscles are prominent (and are present adjacent to the myocardium so that it becomes difficult to distinguish the two), the performance substantially degrades. This issue is tackled as described in later chapter (Chapter 4).

To get significant information regarding LV, the outer wall of myocardial muscle (epicardium) is as much important as the blood pool. Since the change in grey level distribution from myocardial muscle to surrounding muscles is not abrupt, it would be unworthy to use Random Walk (else it would also include the surrounding muscles). Instead, we intend to utilize the blood pool boundary to get the epicardial wall, as depicted in the next chapter.

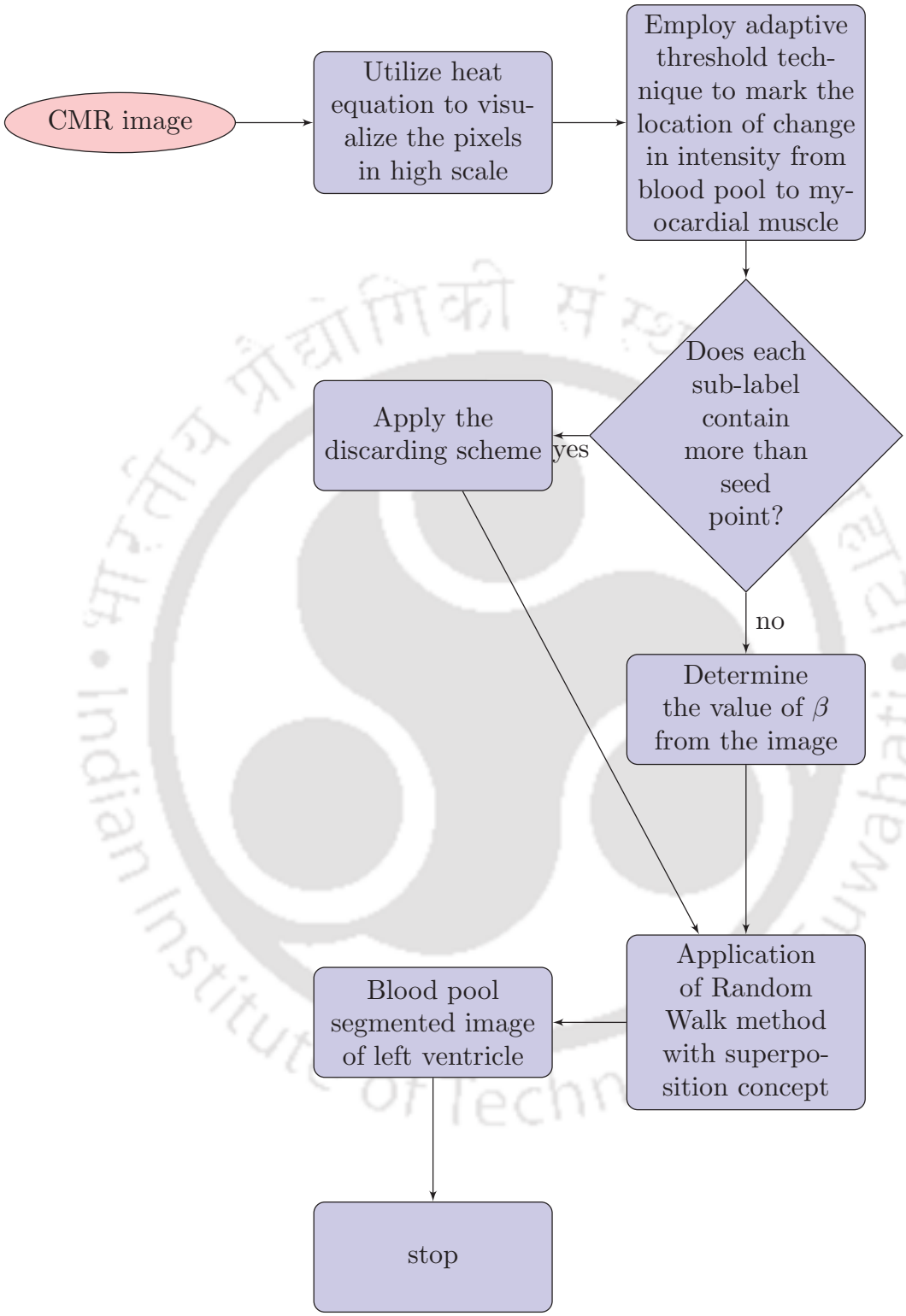

Figure 2.14: Summary of the proposed algorithm.

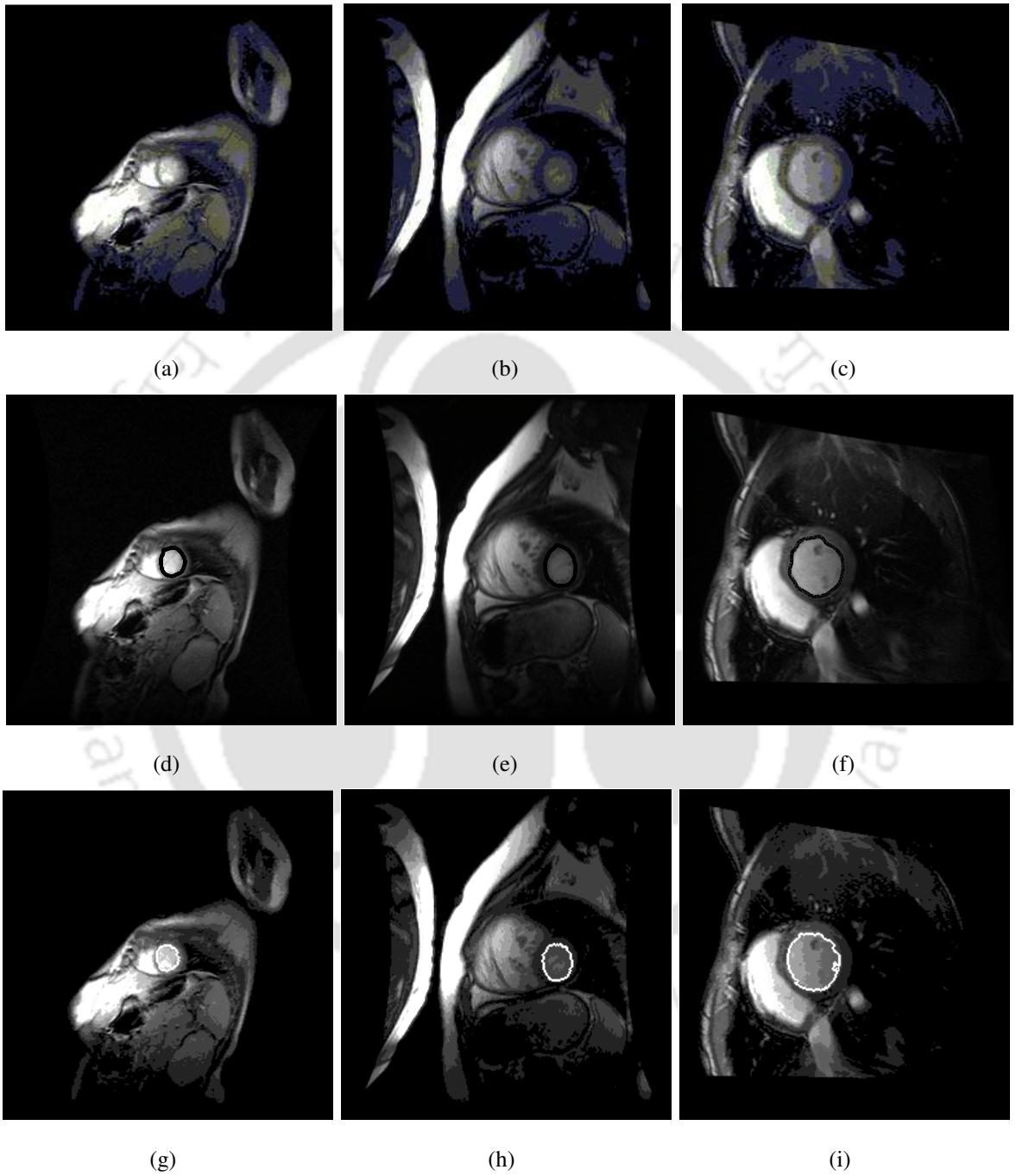

(a) (b) (c)

(d) (e) (f)

(g) (h) (i)

Figure 2.15: (a-c) Original CMR images. (d-f) Ground truth equivalents. (g-i) Determined contour extraction.

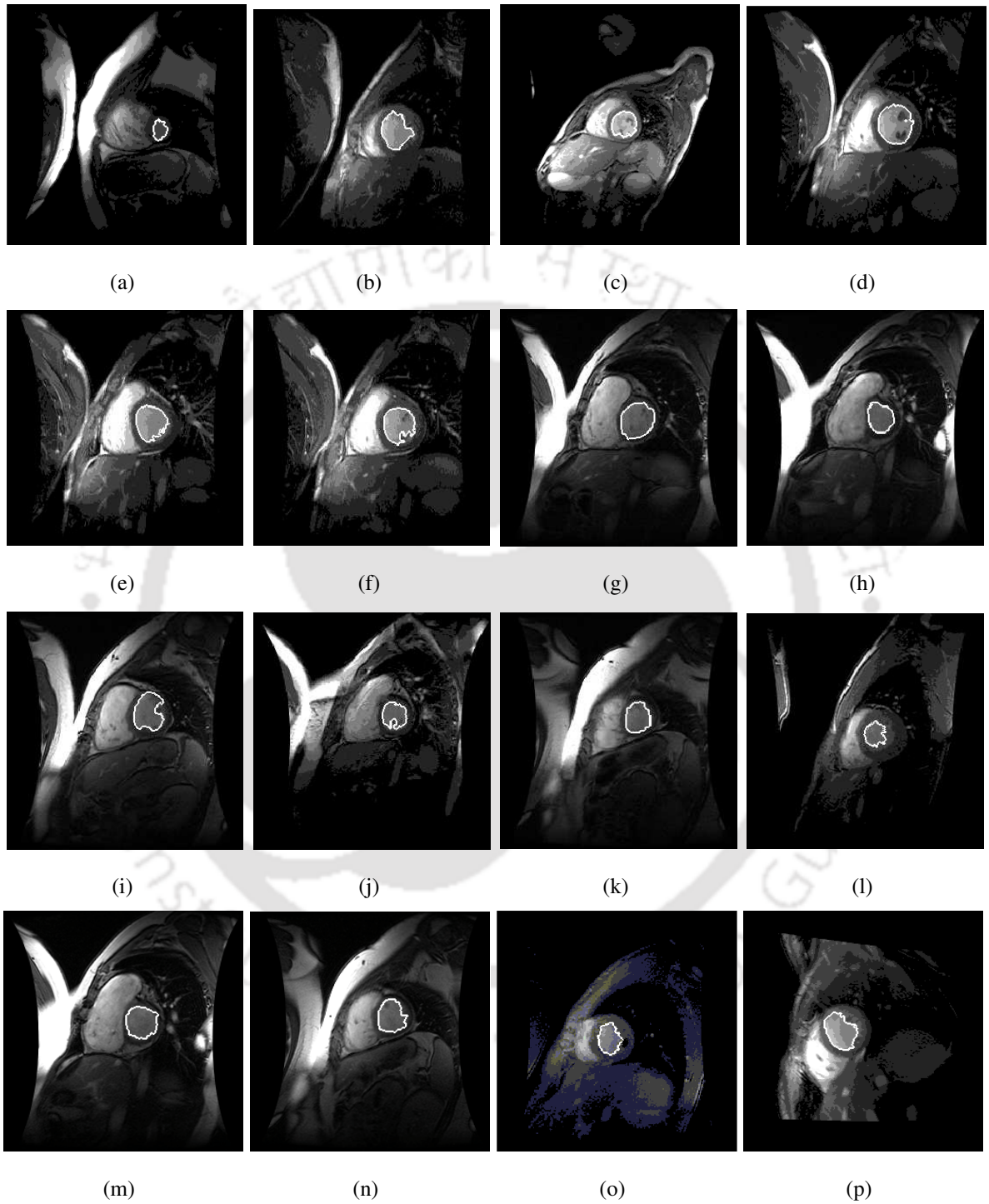

Figure 2.16: Segmented slices of subjects with (c,d,e,f,h,p) significant demarcation and (a,b,g,i,j,k,l,m,n,o) poor demarcation.

Chapter 3

Epicardial Wall Extraction Using a Modified Active Contour Model

Epicardium is the outer wall of the myocardium and similar to endocardium by characteristics. Unlike the blood pool, it is surrounded by muscles that have nearly same grey level intensity. Therefore, distinguishing the surrounding muscle from the infarcted area in the myocardium involves a major difficulty even to the experts. Following a brief literature survey, the proposed model adapted to overcome the difficulties is discussed in this chapter.

3.1 Selected Literature Survey

Several attempts towards epicardial wall detection have so far been reported in literature [97–101]. Chu and coworkers [100] apply the Laplacian of Gaussian (LoG) operator to obtain a zero-crossing map guiding the subsequent boundary searching processes. Human intervention is needed to define the center of the heart chamber and a set of search limits for both endocardial and epicardial borders. Ong and coworkers [102] report a knowledge based system which utilizes the knowledge of heart wall motion in detecting boundaries in a sequence of images. Bosch and coworkers [103] introduce a minimum-cost contour detection algorithm based on a novel iterative approach. In [97], the image is first enhanced by applying the LoG edge detector and then the center of the left ventricle is determined automatically by analyzing the original image. Next, a search process radiated from the estimated center is performed to locate the endocardial boundary by using the zero-crossing points. After this step, the estimation of the range of radius of possible epicardial boundary is carried out by comparing the high-level knowledge of intensity

changes along all directions with the actual image intensity changes. The high-level knowledge of global intensity change in the image is acquired from experts in advance and represented in the form of fuzzy linguistic descriptions and relations. Knowledge of local intensity change can therefore be deduced from the knowledge of global intensity change through fuzzy reasoning. After the comparison, multiple candidate ranges as well as the grades of membership indicating confidence levels are obtained along each direction. The most consistent range in each direction is selected to guide the epicardial boundary search. Multiple candidate epicardial boundaries are then found by locating the zero-crossing points in the range. The one with best consistency is selected as the epicardial boundary. A graph-based optimal border detection [99] determines the criterion of optimality by learning from border tracing examples. Border features employed in this designed method are selected from a predefined global set using radial-basis neural networks. Lilly and coworkers [104] exploit the model based contour definition from radiographic images. In [105], Ezekiel and coworkers introduce a cost function to measure the goodness of edge points in an automated endocardial edge detection algorithm. The proposed algorithms in [106] are Center-Based approach in which the LV center point (LVCP) is estimated using a fuzzy-Based technique and then epicardial and endocardial edge points are searched on radial lines emanating from LVCP. A basic assumption in the first algorithm is that the boundary points of LV are those with sharpest intensity changes, which can be detected as the global maximum wavelet transform modulus. In the second algorithm directional gradient with LVCP references are computed in all directions and all scales using wavelet transform. The images of gradient at different scales are then combined by logical operation to retain only possible boundary points and in this way the list goes on.

3.1.1 Motivation

The capability of most of the algorithms discussed above is limited, since local information is not integrated to form a globally consistent interpretation. As a result, the human operator is needed to provide global information and it is very well known that human operator induces variability in the performance. Therefore, its detection should be made as automatic as possible. If at all, Random walk is implemented, it is obvious that the output will be counter-productive. Since the intensity difference between the myocardial muscle and the surrounding ones is very little, the final contour must include those undesired surrounding muscles. The fact is verified

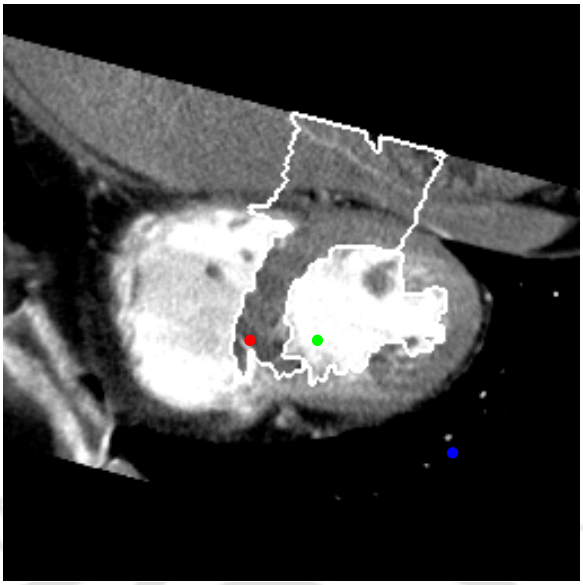

Figure 3.1: Both endo and epicardial wall detection by Random Walk method.

from the Figure 3.1, where the segmentation is carried out on a CT scan image (used by Grady, 2006 shown in Figure 1.3(a)). By putting more seeds (here marked as red) on rest of the myocardial muscle, a complete epicardial contour can be extracted. The point to be noted here is the difficulty in placing more number of seeds on (thin, blurred and indistinguishable) myocardial region in practical CMR images.

When proposing a segmentation method, one has to first clearly define the problem and the goals one wants to reach. In this context, since our objective is to segment out the epicardial wall, instead of introducing a separate method, we intend to drive the blood pool boundary to the epicardium. From literature [29], active contour is found to be an ideal choice for it. In this chapter, a requisite study on active contour model and some of its problems are discussed. Then, in order to achieve the said objective, we suggest some modifications to an existing method that uses active contour principle.

3.2 Active Contour Model

The basic idea behind active contour model is that the variable curve evolves (round the object) and moves towards the interior normal and stops at the boundary of the object. The stopping term, which is normally defined in term of image gradient, stops the curve at the boundary.

3.2.1 General Edge Detector

A general edge detector is defined by a positive and decreasing function g, depending on the gradient of the image u_0 such that

$$\lim_{z \to \infty} g(z) = 0 \tag{3.2.1}$$

For instance,

$$g(|\nabla u_0(x,y)|) = \frac{1}{1 + |\nabla G_\sigma(x,y) * u_0(x,y)|^p},\ p \geqslant 1 \tag{3.2.2}$$

where $G_\sigma(x,y) * u_0(x,y)$ is the smoother version of $u_0(x,y)$, while (x,y) represents the spatial coordinates. The value of $g(|\nabla u_0(x,y)|)$ is positive in homogeneous regions and zero at the edges.

The variable curve C is represented by the Lipschitz function ϕ and defined as $C = \{(x,y) | \varphi(x,y) = 0\}$. The evolution of the curve is given by zero level curve at time t of function $\varphi(t,x,y)$. Evolving C in normal direction with speed F amounts to solve

$$\frac{\partial \varphi}{\partial t} = |\nabla \varphi| F \tag{3.2.3}$$

The initial contour is specified at time $t = 0$ as, $\varphi(t,x,y) = \varphi_0(x,y)$. If the motion results from the mean curvature, then

$$F = div\left(\frac{\nabla \varphi(x,y)}{|\nabla \varphi(x,y)|}\right) \tag{3.2.4}$$

3.2.2 Active Contours

A classical approach consists in detecting edges and then linking them in order to determine the shape of the object. However, this approach does not make use of the knowledge that the object is simply connected. On the other hand, deformable models which incorporate knowledge about the shape of the object are widely used. With these techniques, rather than expecting desirable properties such as continuity and smoothness of the contour to emerge from the image data, those properties are imposed from the start. Deformable models encompass a variety of forms, principally active contours and deformable templates.

An active contour [19] or *snake* is a continuous curve (a set of n control points, v_i = (x_i, y_i) where $i = 0...n-1$) which has the ability to evolve in order to match an object in the image. It is initialized close to the searched contour, and it deforms according to the iterative optimization of

a numerical criterion. This criterion is usually called "energy" since it was at the origin directly interpretable in terms of physical constraints, such as rigidity, stiffness, and attraction, to the image edges. Convergence of the snake toward the searched object can then be seen as the fulfillment of a mechanical stability condition.

Formulation of Snake Energy

A snake may be thought of as an elastic curve that, through minimization of an energy functional, deforms and adjusts its initial shape on the basis of additional image information to provide a continuous boundary. The energy functional being minimized is derived from forces which are both internal and external to the snake. Internal forces are responsible for snake response, that is, its elasticity and rigidity, whereas external forces come from the image or from higher-level processes and are responsible for moving the snake toward important features in the image. One of the chief virtues of snake representations is that it is possible to specify a wide range of snake properties, through a function called the energy by analogy with physical systems. A program controlling a snake causes it to evolve so as to reduce its energy, so by specifying an appropriate energy function, we can make a snake that will evolve to have particular properties, such as smoothness. The original formulation of active contours by Kass et al. [19] is presented here. The active contour is defined as a parameter in-plane curve C:

$$\begin{aligned} [0,1] &\rightarrow R^2 \\ s \rightarrow v(s) &= \begin{bmatrix} x(s) \\ y(s) \end{bmatrix} \end{aligned} \tag{3.2.5}$$

where s denotes the curvilinear abscissa and $v(s)$ the point of co-ordinates $x(s)$, $y(s)$ on the curve. The following energy is associated with the curve C:

$$E(C) = E_{in}(C) + \gamma E_{ext}(C) \tag{3.2.6}$$

where γ is a real valued number. This energy is the weighted sum of two terms which represents two different types of constraints imposed on the active contour. By minimizing the weighted sum, one expects to get a good compromise between these constraints.

Internal Snake Energy (E_{in})

The internal energy is the part that depends on intrinsic properties of the snake, such as its length

or curvature. It is determined by the elasticity and rigidity of the snake. The first term in Equation 3.2.6 has the following expression:

$$E_{in}(C) = \int_0^1 \alpha(s) \left|\frac{\partial v}{\partial s}\right|^2 + \beta(s) \left|\frac{\partial^2 v}{\partial s^2}\right|^2 ds \tag{3.2.7}$$

This internal energy is so named since it characterizes the shape of the contour independently of grey levels in the image. The physical interpretation is described as follows: 1) The coefficient $\alpha(s)$ represents the rigidity of the curve, i.e. the cost which has to be paid to increase the length. 2) The coefficient $\beta(s)$ represents the stiffness of the curve, i.e. the cost to bend it. If $\alpha(s)$ increases, the contour will have a tendency to go back to a statistical means, ultimately to a single point. If $\beta(s)$ increases, the contour becomes smoother. Mostly, these parameters are made locally adaptive. For example, lowering $\beta(s)$ at some point will enable the contour to adapt to a sharp edge of the object.

Optimizing only the internal energy in Equation 3.2.7 will lead to a short and smooth contour, which will collapse to a single point. Therefore, one needs to balance this shrinking effect of the internal energy with an external energy which depends on the information in the image.

External Snake Energy (E_{ext})

The external energy depends on factors such as image structure, and particular constraints the user has imposed. The external energy can have contributions other than the image energy. A constraint energy is often included which is determined by constraints applied by the user. For instance the snake might be pulled to particular points as if by springs, or might be repelled by a particular point. This is valuable in the "power assist" style of operation. These determine its relationship to the image. Suppose we want a snake to latch on to bright structures in the image. Then the obvious energy function is the negative sum of the grey levels of the pixels, on top which the snake presently resides. Reducing this energy function (i.e. making it more negative) will move the snake towards brighter parts of the image.

External energy (second term of Equation 3.2.6) represents the way in which the snake energy depends on the image grey levels. The latitude is more while choosing this energy, which must be adapted to the characteristics that makes it possible to discriminate the object from the back ground. It should be noted that in the original formulation of the snake, the characteristic that is taken into account is the presence of sharp edges between the object and background regions.

Thus the following expression is proposed by Kass et al.:

$$E_{ext}(C) = -\int_0^1 |\nabla u_0(v(s))|^2 ds \tag{3.2.8}$$

where $u_0(x, y)$ represents the image and ∇u_0 represents the result of applying a gradient operator which enhances the edges present in the image. This external energy is so named since it represents the force imposed by the data to the snake. To minimize this energy, the snake will have to match as closely the point on which the gradient is high. Overall, the external energy is related to the image as follows:

- Since the snake is desired to be attracted to edges, so this energy is usually based on the image gradient.
- A high image gradient should give a low energy and vice-versa.

Numerical Aspects of Segmentation -

Optimization in this context means using mathematical techniques to find the maximum or minimum of a function, and is not to be confused with optimizing a program, which usually just means trying to make it run faster. The function to be minimized here is the total snake energy. From a numerical point of view, the segmentation problem consists in minimizing the following functional:

$$E(C) = \int_0^1 \left[\alpha(s)\left|\frac{\partial v}{\partial s}\right|^2 + \beta(s)\left|\frac{\partial^2 v}{\partial s^2}\right|^2 - |\nabla u_0(v(s))|^2\right] \tag{3.2.9}$$

where α, β and γ are real-valued coefficients which balance the different contributions to the snake energy. For the shake of simplicity, let us consider them as invariant of the curvilinear abscissa s. If the contour is assumed to be closed, annulling the derivative of this functional with respect to the contour C leads to the following Euler-Lagrange equation

$$\alpha\kappa(s)\,\overrightarrow{\mathrm{N}} + \beta\frac{\partial^4 v}{\partial s^4} - \gamma\nabla\left[|\nabla u_0(v(s))|^2\right] = 0 \tag{3.2.10}$$

When a curve is parameterized by the curvilinear abscissa, we get:

$$\frac{\partial^2 v}{\partial s^2} = \kappa(s)\,\overrightarrow{\mathrm{N}} \tag{3.2.11}$$

where $\kappa(s)$ is the local curvature and $\overrightarrow{\mathrm{N}}$ the vector normal to the curve at abscissa s. Minimization of Equation 3.2.9 with steepest gradient descent method [107] is desired in order to solve

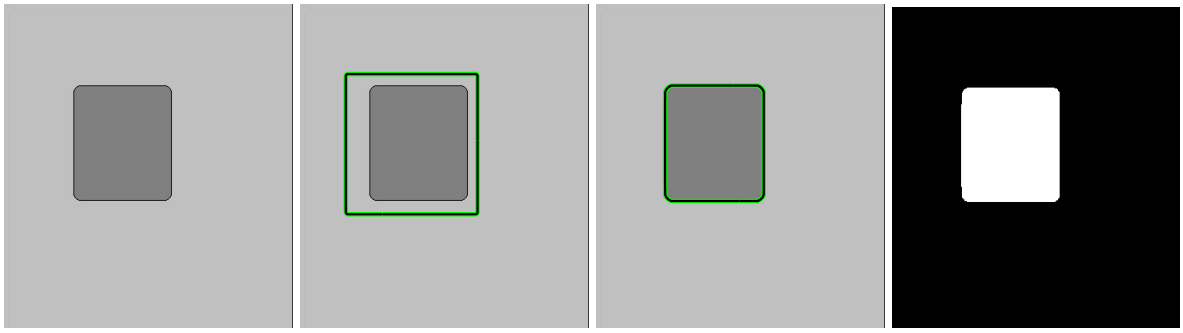

(a) (b) (c) (d)

Figure 3.2: (a) Original synthetic image. (b) Contour position at 10^{th} iteration. (c) Contour position at 140^{th} iteration. (d) Final segmented image.

Equation 3.2.10. For this, one assumes the curve depends on time t and is denoted as $v(s,t)$. The following equation is iteratively solved:

$$\frac{\partial v\left(s,t\right)}{\partial t}=\alpha\kappa\left(s,t\right)+\beta\frac{\partial^{4}v\left(s,t\right)}{\partial s^{4}}-\gamma\nabla\left[\left|\nabla I\left(v\left(s,t\right)\right)\right|^{2}\right] \tag{3.2.12}$$

Starting with the initial shape $v(s,0)$ at time $t=0$, one lets the dynamical system evolve until it stabilizes, i.e., $\frac{\partial v(s,t)}{\partial t}=0$. The entire process is explained with respect to the number of iterations as shown in Figure 3.2.

3.2.3 Geometric Active Contour Model

Geometric active contours are represented implicitly as level sets of two dimensional distance functions which evolve according to an Eulerian formulation. They are based on the theory of curve evolution implemented via level set techniques [22].

$$\frac{\partial\varphi}{\partial t}=g\left(\left|\nabla u_{0}\right|\right)\left|\nabla\varphi\right|div\left(\frac{\nabla\varphi}{\left|\nabla\varphi\right|}+v\right),v\geqslant0 \tag{3.2.13}$$

in $(0,\infty)\times\mathbb{R}^{2}$ and $\varphi\left(0,x,y\right)=\varphi_{0}\left(x,y\right)\ in\ \mathbb{R}^{2}$, where the value of p is usually set as 2; φ_0 being the initial level set function, the curve stops at the boundary where the edge function $g\left(\left|\nabla u_{0}\right|\right)$ vanishes. The constant $v\geq0$ makes the right hand term always positive. This constant may be interpreted as a force pushing the curve to the object.

3.2.4 Geodesic Active Contour Model

This framework is based on boundary based information (relies on accurately extracting the borders between different texture regions in an image), and aims at finding the best minimal

length smooth curve that takes into account the desired image properties. The objective function is defined as

$$J(C) = 2\int_0^1 |C'(s)| \, .g\left(|\nabla u_0 C(s)|\right) ds \tag{3.2.14}$$

where curve $C(s)$ is the active contour varying with abscissa. The term $g\left(|\nabla u_0 C(s)|\right)$ vanishes when the curve is at the object boundary. This model also has a level set formulation

$$\frac{\partial \varphi}{\partial t} = |\nabla \varphi| \left(div \left(g\left(|\nabla u_0|\right) \frac{\nabla \varphi}{|\nabla \varphi|} + vg\left(|\nabla u_0|\right) \right) \right) \tag{3.2.15}$$

The choice of different parameters (weighting coefficients, time and space discretization steps) is difficult and critical to the performance of the snake, as well as the choice of the initial shape. Since the image formation (gradient) which is used to drive the snake is detected edges of the objects, the classical snake model is classified in the category of edge-based segmentation approaches. This type of active contours is thus adapted to a class of problems in which the objects to segment form sharp edges with respect to the background. Moreover, they are sensitive to the choice of the initial shape and the curve will not evolve if it is not close enough to the object edges.

All these classical snakes and active contour models rely on the edge function g, which depends on the image gradient (at the so called object boundary), to stop the curve evolution. In practice, the discrete gradients are bounded and then the stopping function is never zero on the edges, and the curve may pass through the boundary. This is well known that in ischemic CMR image, the edge between myocardium and surrounding muscle is very difficult to specify. Therefore, this model in its current form is less worthy to implement on CMR images to detect the epicardium. The following section presents a modified scheme based on the active contour model [29] that extracts the outer contour without depending on the stopping function g.

3.3 Modified Active Contour Without Edges (MACWE)

Let us consider an image u_0 that consists of only two regions (u_0^i, u_0^o) of piecewise constant intensity. Suppose C_0 be the boundary of one of the regions (objects), say u_0^i as shown in Figure 3.3.

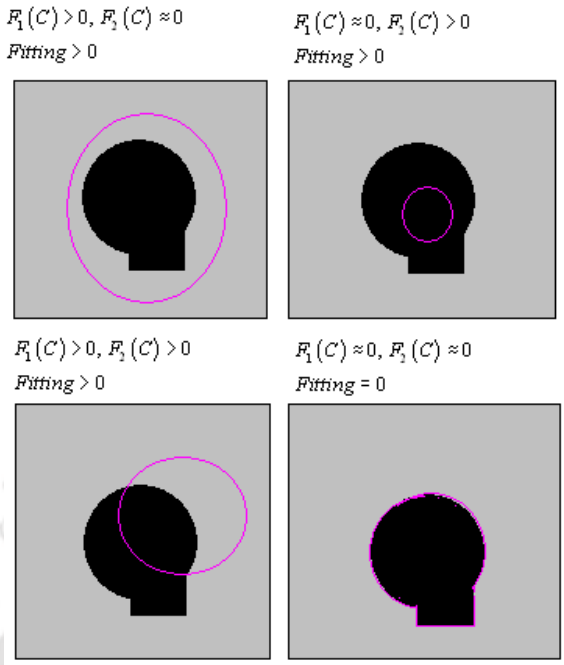

Figure 3.3: Illustration of object and curve placement in active contour model (Chan et al., 2001).

Let us consider an objective term defined as

$$F_1(C) + F_2(C) = \int_{inside(C)} |u_0(x,y) - c_1|^2 \, dxdy + \int_{outside(C)} |u_0(x,y) - c_2|^2 \, dxdy$$

where C is any other variable curve, and the constants c_1, c_2 are the averages of u_0 inside and outside C, respectively. It is obvious that there will only be at maximum four possibilities regarding the values of $F_1(C)$ and $F_2(C)$ as follows:

1. If the curve C is outside the object, then $F_1(C) > 0$ and $F_2(C) \approx 0$;
2. If the curve C is inside the object, then $F_1(C) \approx 0$ and $F_2(C) > 0$;
3. If the curve C is both inside and outside the object, then $F_1(C) > 0$ and $F_2(C) > 0$; and
4. If the curve C is on the boundary of the object, $F_1(C) \approx 0$ and $F_2(C) \approx 0$.

In the original method [29], the curve moves towards its interior normal and stops on the boundary of the object as shown in Figure 3.4. The fitting energy (Equation 3.3.1) must be minimized when the curve exactly lies on the object boundary (as shown in Figure 3.3, the fourth possibility).

Here, the object to be segmented must be homogeneous, so that $|u_0(x,y) - c_1|$ will be zero when the curve is at the exact boundary if at all we ignore the second term in the consideration.

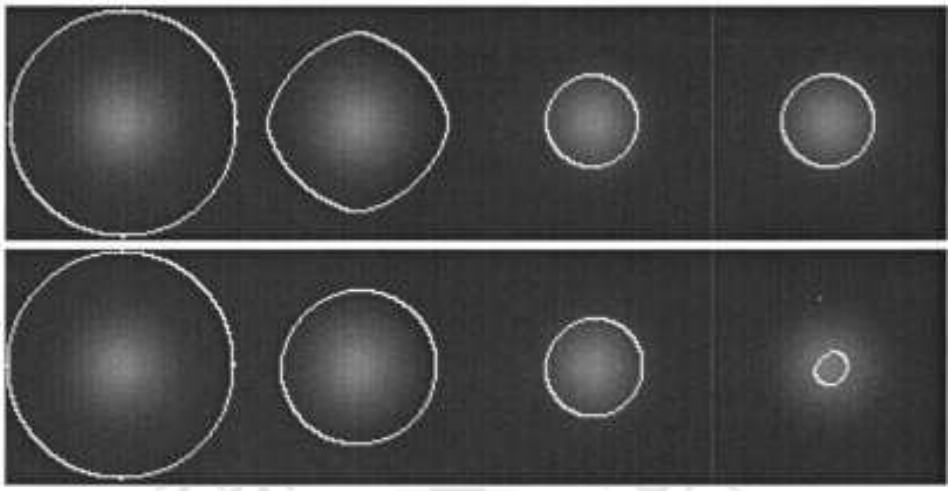

Figure 3.4: Illustration of object and curve resulting in active contour model (Chan et al., 2001).

In the context of our objective, as two different intensity regions are to be accommodated in the object i.e., blood pool and myocardium, the first possibility (in Figure 3.3) has to be satisfied. Therefore in our active contour model, we will minimize the energy term defined in Equation 3.3.1. The energy functional for this purpose is

$$F(c_1, c_2, C) = -\mu.L(C) - \lambda_1 \int_{in(C)} |u_0(x,y) - c_1|^2 \, dxdy + \lambda_2 \int_{out(C)} |u_0(x,y) - c_2|^2 \, dxdy \tag{3.3.1}$$

where $in(C)$, $out(C)$ and $L(C)$ represent inside, outside and length of the curve C, respectively; $\mu \geq 0$ and $\lambda_1 = \lambda_2 = 1$ (as defined in [29]). For level set formulation of the model, $C \subset \Omega$, C is replaced by ϕ. Using the Heaviside function (H) and Dirac measure δ_0, the energy $F(c_1, c_2, C)$ is written as

$$F(c_1, c_2, \phi) = -\mu \int_{\Omega} \delta(\phi(x,y)) |\nabla\phi(x,y)| \, dxdy - \lambda_1 \int_{\Omega} |u_0(x,y) - c_1|^2 H(\phi(x,y)) \, dxdy + \lambda_2 \int_{\Omega} |u_0(x,y) - c_2|^2 (1 - H(\phi(x,y))) \, dxdy$$

The first term corresponds to $\phi = 0$, second term for $\phi > 0$ and third term for $\phi < 0$. The terms H and δ_0 are defined as:

$$H(z) = \begin{cases} 1, & if\ z \geqslant 0 \\ 0, & if\ z < 0 \end{cases}$$

$$\delta_0(z) = \frac{d}{dz}H(z)$$

Euler-Lagrange equation for ϕ is deduced, keeping c_1 and c_2 fixed, and minimizing F with respect to ϕ. Parameterizing the ascent direction by a time t, the equation in $\phi(t,x,y)$ (with $\phi(0,x,y) = \phi_0(x,y)$ defining the initial contour) is

$$\frac{\partial\phi}{\partial t} = \partial_\varepsilon(\phi)\left[-\mu\, div\left(\frac{\nabla\phi}{|\nabla\phi|}\right) + \lambda_1(u_0 - c_1)^2 + \lambda_2(u_0 - c_2)^2\right] = 0 \ in \ (0,\infty)\times\Omega, \quad (3.3.2)$$

$$\frac{\partial_\varepsilon(\phi)}{|\nabla\phi|}\frac{\partial\phi}{\partial\overrightarrow{n}} = 0 \ on \ \partial\Omega$$

where $\frac{\partial\phi}{\partial\overrightarrow{n}}$, $\overrightarrow{n}$ denote the normal derivative of ϕ at the boundary and the exterior normal to the boundary $\partial\Omega$ respectively. Finally, The partial equation is solved in order to get the desired ϕ. The stationarity with respect to ϕ is achieved (i.e. ϕ is discretized) with the help of a finite difference scheme. Let Δt be the time step and (x_i, y_i) be the grid points for $1 \leq i, j \leq M$, where M is the total number of grid points. Let $\phi^n_{i,j} = \phi(x_i, y_j, n\Delta t)$ be an approximation of $\phi(x,y,t)$ with $n \geq 0$, $\phi^0 = \phi_0$. Finite differences are described as follows:

$$\nabla^x_- \phi_{i,j} = \phi_{i,j} - \phi_{i-1,j} \quad \nabla^x_+ \phi_{i,j} = \phi_{i+1,j} - \phi_{i,j} \quad (3.3.3)$$

$$\nabla^y_- \phi_{i,j} = \phi_{i,j} - \phi_{i,j-1} \quad \nabla^x_+ \phi_{i,j} = \phi_{i,j+1} - \phi_{i,j} \quad (3.3.4)$$

The stationarity with iteration is achieved, when one sees no change in the value of ϕ. In this way, the epicardium is extracted taking the blood pool boundary as the initial contour ϕ_0.

3.4 Presentation of Results

A set of three images, their ground truths and determined epicardial contour extraction (along with endocardial wall) are shown in Figure 3.5. In addition, some of the results shown in Chapter 2 for endocardium extraction have been taken here. The above described scheme is applied on them considering the endocardial boundary as the initial contour. Ground truth images of some CMR images are provided in Figure 3.7 to have a feel regarding the structure of the outer boundary. The results are shown in Figure 3.8 against the images in Figure 3.6. Promising results illustrate the merits of the approach irrespective of the object to be segmented. We mean to express the efficiency of the approach even on images where object boundary is no significantly different from the surrounding grey level intensity, since the initial contour is known *a priori*.

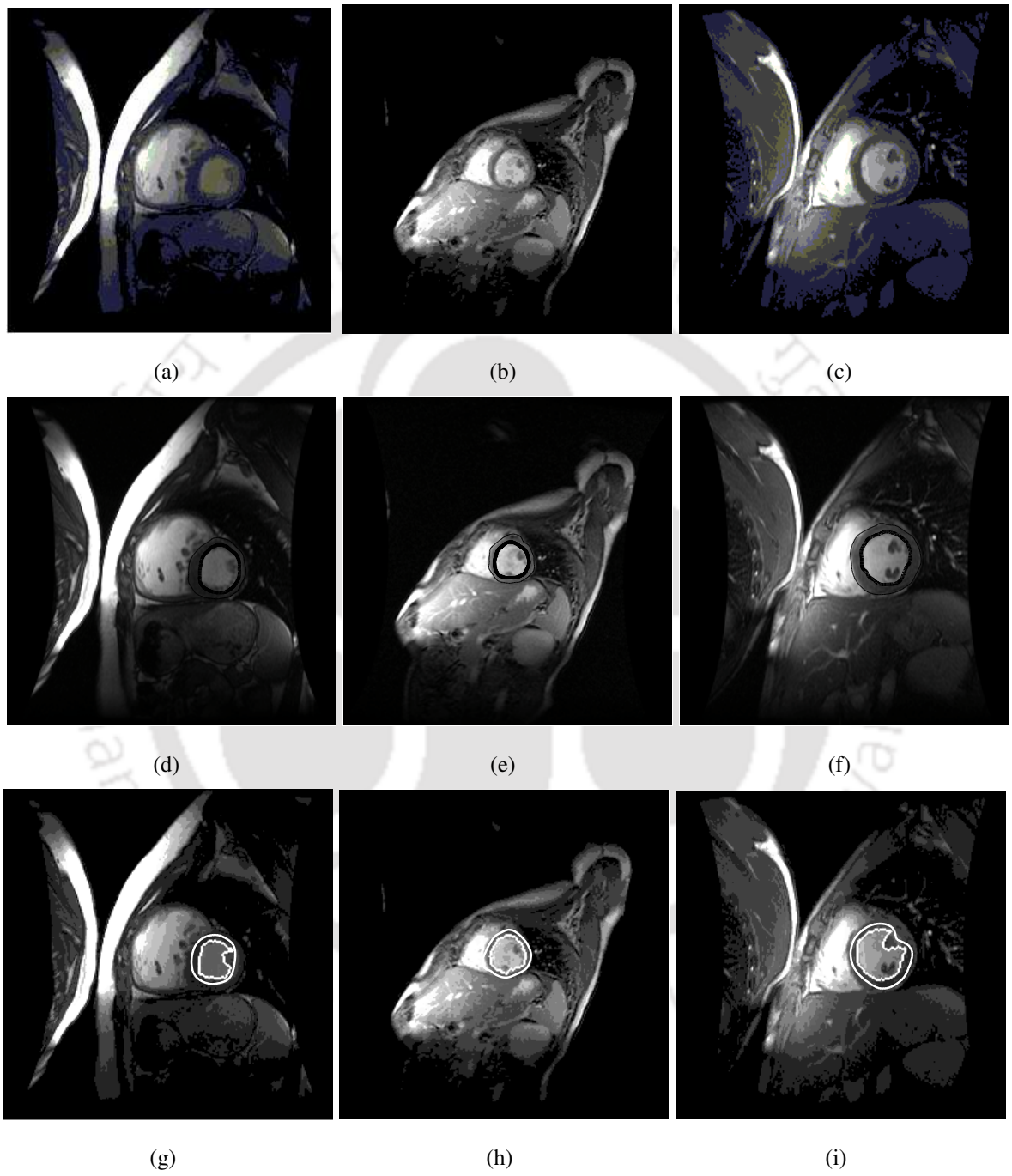

(a) (b) (c)

(d) (e) (f)

(g) (h) (i)

Figure 3.5: (a-c) Original images. (d-f) Ground truth images. (g-i) Random Walk and modified active contour model based segmentation.

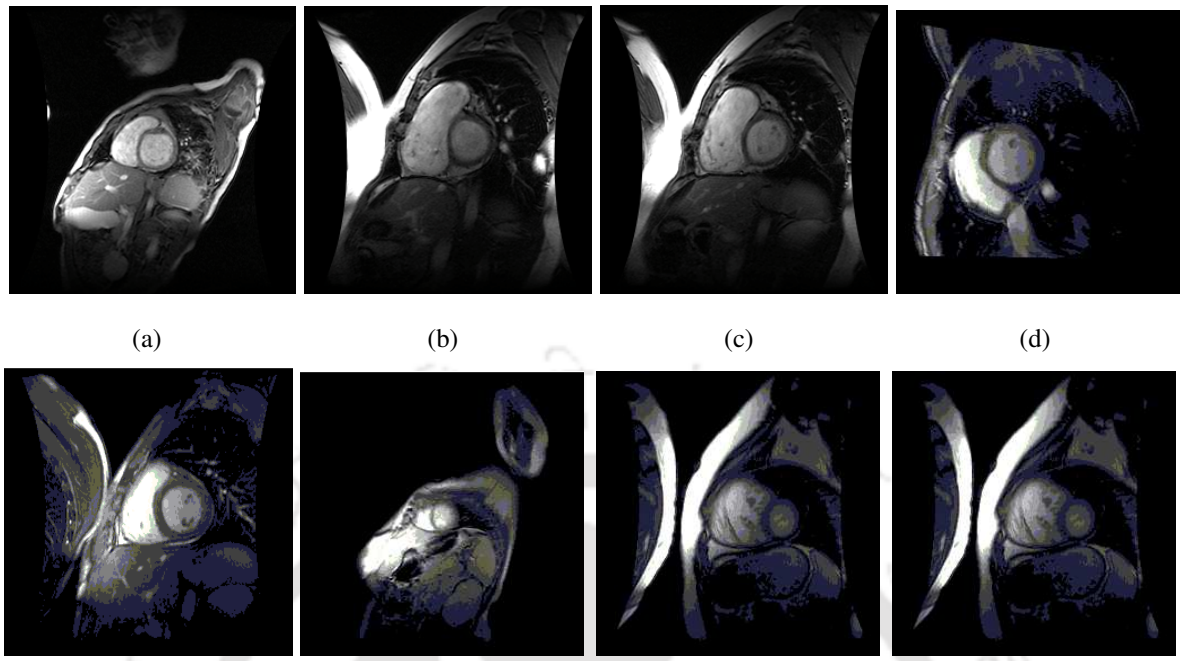

(a) (b) (c) (d)

(e) (f) (g) (h)

Figure 3.6: (a-h) Some original CMR images.

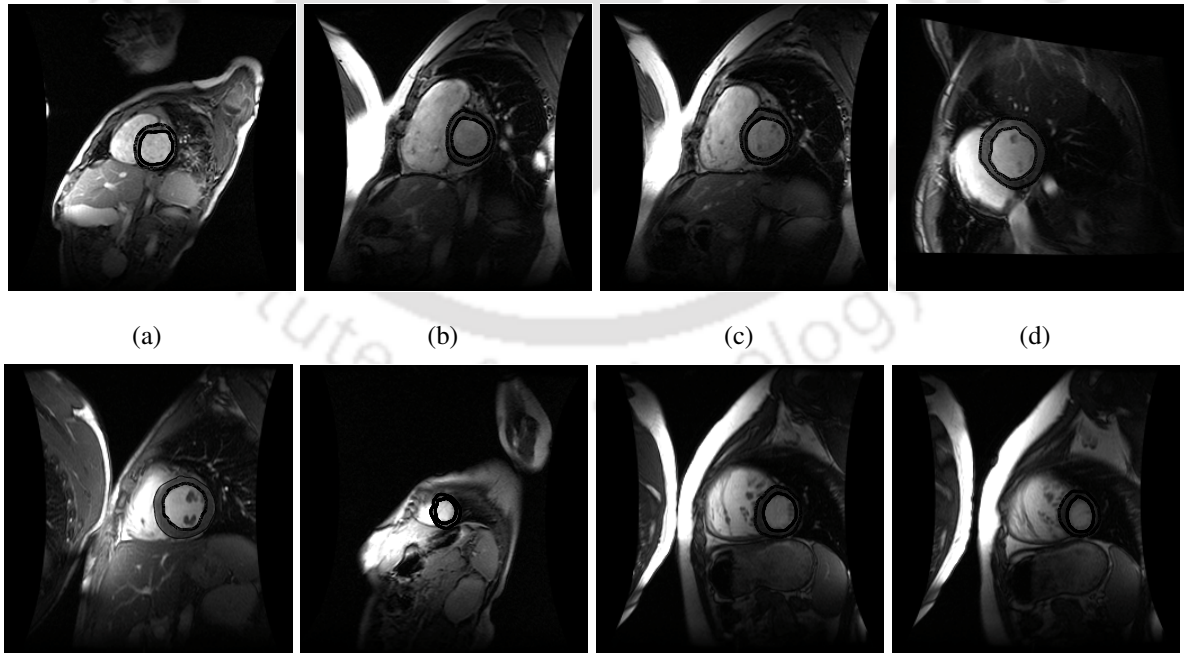

(a) (b) (c) (d)

(e) (f) (g) (h)

Figure 3.7: (a-h) Ground truth equivalents of CMR images shown in Figure 3.6.

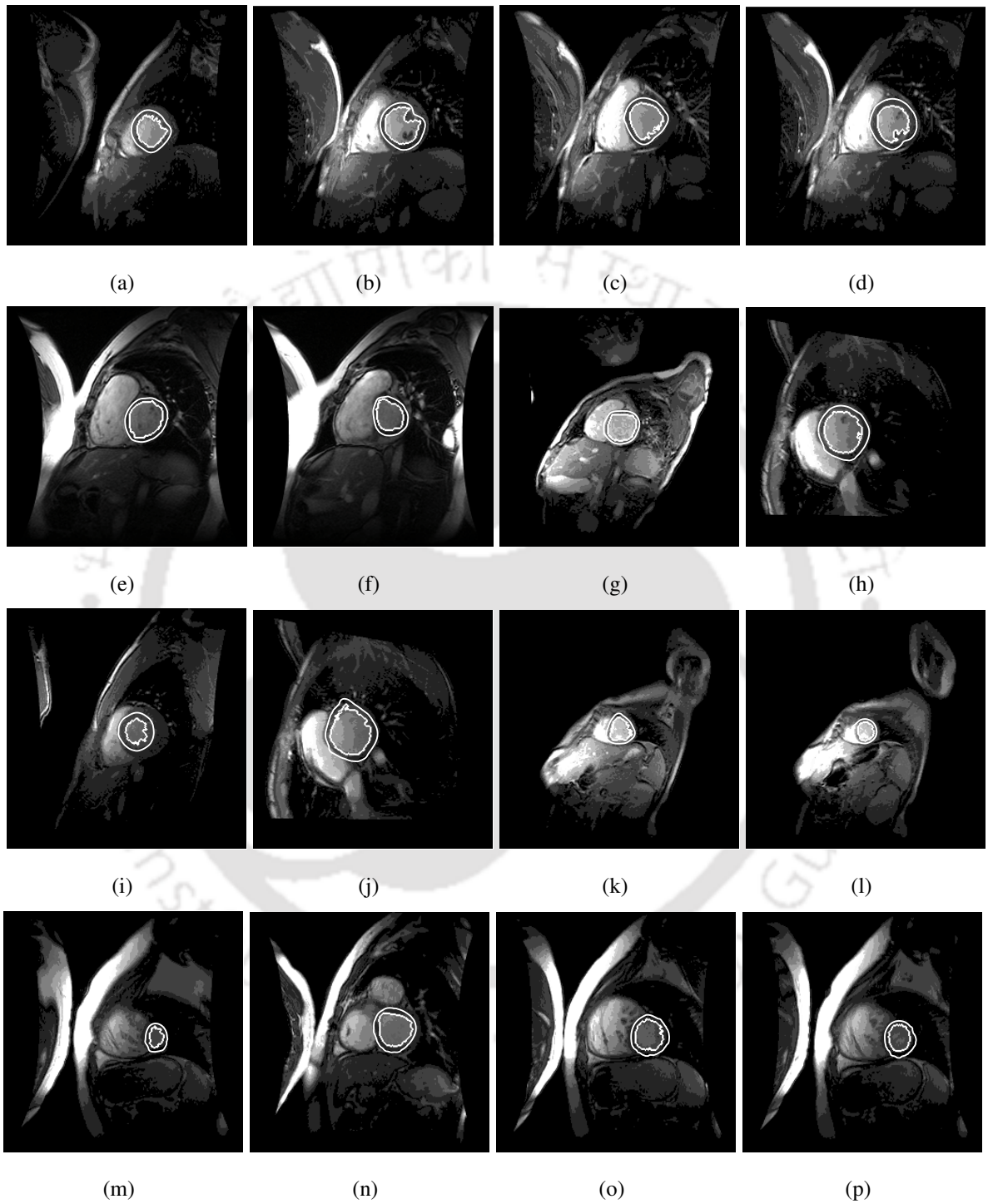

Figure 3.8: (a-p) Segmented slices of different subjects with Random Walk approach and modified active contour model.

3.5 Conclusions

Active contours or "snakes" are often used to identify boundaries within images that are too irregular or noisy to be detected reliably by conventional means. In context with ischemic CMR image, some modifications were desired in order to achieve the epicardium. A modified active contour method has helped in getting the same which takes the blood pool boundary as its initial contour. Therefore, unlike the traditional active contour method, the task of placing the initial contour has been avoided. This model is not based on an edge-function to stop the evolving curve on the desired boundary, because as discussed earlier, defining the function usually is a tough task. Also, we do not need to smooth the initial image even if it is very noisy, so the locations of boundaries are very well detected and preserved. By this model, we can detect objects whose boundaries are not necessarily defined by gradient or with very smooth boundaries, for which the classical active contour models are not applicable. The epicardial wall contour found has been judged very satisfactory [108] by a team of trained clinicians.

The resulting shape of epicardial contour depends on that of the blood pool boundary. The accurate description of the inner contour lies on the type of input image. If it belongs to a long axis CMR data, then determination of β from the adequate background region will be accurate, which in turn will lead to an appropriate blood pool segmentation, else, a pseudo contour is generated. When the background region is insufficient (in case of short axis CMR data), by following the method discussed in Chapter 2, one may not get a proper value of β. Therefore, the entire weighting function needs to be modified, which is discussed in the next chapter. This modified weighting function can well be used in long axis CMR image segmentation also.

Again, papillary muscles are important in the left ventricle. The papillary muscles play an important role in both LV and mitral valve function [109], therefore, its inclusion should not be ignored in any segmentation. Because of its nature in regard to intensity, the LV looses its homogeneity mainly due to their prominent presence. The Random Walk approach miserably fails (from results in Chapter 2) to perform satisfactorily unless proper modification is perceived. Segmentation of CMR images having papillary muscles adjacent to myocardium is furnished in the next chapter.

Chapter 4

Weighting Function in Random Walk Approach

In the process of segmentation using Random Walk, the weighting function (for determining the adjacency matrix) is used to map a change in image intensities to edge weights. Importantly, the performance of any graph based segmentation depends on the choice of this function [65]. The weighted graph is constructed by taking each pixel as a node and connecting each pair of pixels by an edge. The weight on that edge reflects the likelihood that the two pixels belong to the same object. Taking the brightness value of the pixels and their spatial location, the graph edge weight (w_{ij}) connecting the two nodes i and j is usually defined as:

$$w_{ij} = e^{-\frac{\left|D_i - D_j\right|^2}{\sigma_I^2}} * \begin{cases} e^{-\frac{\left|X_i - X_j\right|^2}{\sigma_X^2}}, & \text{if} \quad \|X_i - X_j\|_2 < r \\ 0, & \text{otherwise.} \end{cases} \tag{4.0.1}$$

where D_i and X_i represent distance and brightness, respectively. The term r, σ represent the threshold value and standard deviation, respectively.

In this chapter, the importance of weighting function is illustrated following a discussion of its usage in Random Walk based image segmentation. Though the approach is already depicted in Chapter 2, it is again elaborated giving more emphasis on the exact behavior of the weighting function. Its behavioral studies are given in later sections, complying a condensed written summary of the approach for image segmentation. Based on its analysis, we suggest the use of different weighting functions in association with Random Walk. These are intended to produce satisfactory results, particularly, on short axis CMR images.

4.1 Influence of Weighting Function in Random Walk Approach

Random walker (a subject that is assumed to walk randomly on nodes) is initialized with a set of pixels taking one of a predefined set of labels. The probability that a random walker starting at a given unlabeled pixel will first reach a pixel of a particular label is computed, based on the solution to Dirichlet problem [110]. The Laplacian matrix is used to model the relationship between the nodes; it plays an important role in the course of segmentation. The pseudo-inverse of the Laplacian matrix plays a key role and has a nice interpretation in terms of Random Walk on a graph. It has some noticeable properties [111],

- it can be interpreted as a similarity measure, and
- the inner-product-based quantities involving the Laplacian matrix provide good and stable results, therefore, it is more suitable in pattern-recognition and machine-learning tasks involving a database.

The relationship with the weight matrices in the graph is well depicted in the following section.

4.1.1 Weighting Function in the Approach

The vertices are the graph's representation of the image pixels and the edges are the representation of each pixel's relationship with its surrounding neighbors (edge weights). The Laplacian matrix that represents the graph is defined as

$$L_{ij} = \begin{cases} d_i, \text{ if } i = j \\ -w_{ij}, \text{ if } v_i \sim v_j \\ 0, \text{ otherwise.} \end{cases} \tag{4.1.1}$$

where L_{ij} refers to each entry in the Laplacian matrix. The term d_i refers to the degree of vertex i, i.e. the number of connection between that particular vertex v_i and its neighboring vertices. The term w_{ij} refers to the edge weight at the ijth position. The weighting function reflects the correlation of two nodes as its output.

The Gaussian weighting function (used to select edge weights) as reported in [67] is defined as:

$$w_{ij} = e^{-\beta(H_u - H_v)^2} \tag{4.1.2}$$

where H_u and H_v indicate the image intensity at pixel u and v, respectively.

In Equation 4.1.2, β is the parameter that is to be decided by the operator. So the risk in introducing variability in the performance is obvious. An attempt has been made (as discussed in Chapter 2) earlier to obtain its value from the background region present in the CMR image. Because of the presence of inadequate background region in short axis CMR image, it is not quite possible to get an accurate β. Additionally we know, an improper value of β leads to an incorrect segmentation. Therefore, the whole weighting function needs some sort of modification for achieving a precise segmentation.

4.1.2 Nature of Gaussian Weighting Function

According to the work reported in [67], weighting function used in this frame work, is to group the similar pixels having minimum euclidian distance and maximize the entropy. Let us briefly try to understand the role of entropy maximization in regard to image segmentation. Consider a classification problem, in which the objective is to estimate a function $class : X \rightarrow Y$, which maps an object $x \in X$ to its correct class $y \in Y$. We can implement any classifier with a conditional probability model p by simply choosing the class with the highest conditional probability:

$$class\,(x) = \arg \max_{y}\ p\,(y|x)$$

where x is an textual object and y is a class. Under the maximum entropy framework, the probability for a class y and object x depends solely on the features that are active for the pair (x, y). This procedure simply gathers all the identical pixels in meaningful groups yielding super-resolution. In the context with edge detection, the entropy is utilized efficiently as discussed by a method reported in [112]. Since edges involve abrupt changes of intensity, color, texture, motion and so on, edges can be extracted by detecting these changes. The entropy operator is used to detect these changes. This operator calculates the entropy of intensity over the region. The entropy is small (large) when the change of brightness is large (small). Then, edges may be extracted by detecting the regions where the entropy is small. Suppose g_0 a be the intensity value at center (i, j) of the window and g_i , $1 \leq i, j \leq n$, be intensity values of its neighbors, where n denotes the number of neighbors. Then the entropy H of the intensity in the region is defined as

$$H = -\sum_{i=0}^{n} \frac{p_i \log\, p_i}{\log\,(n+1)} \tag{4.1.3}$$

where the normalized intensity p_i is defined by

$$p_i = \frac{g_i}{\sum_{j=0}^{n} g_j}. \tag{4.1.4}$$

The entropy H is normalized so that $0 \leq H \leq 1$. Smooth regions give similar p_i's yielding large entropy values. This entropy value is calculated in every region and the regions where the entropy value is small are detected. The edges are detected by selecting the regions having entropy values smaller than a threshold value. value.

The performance of Gaussian weighting function [88] is perfect on clean images where the objects are homogeneous and well separated. This is also accomplished by Grady in his work. The level of precise execution is substantially reduced (as shown in Figure 2.16, particularly in Figure 2.16(f), 2.16(i), 2.16(j)) while applied on CMR slices, because objects in ischemic CMR images are neither homogeneous nor well distinct. In addition, most of the time, the edges in the images are not sharp and are rather blurred. Synthetically generated objects have very sharp transitions leading to sharp edge characteristics. On the other hand, real objects or objects in motion generate blurred transitions leading to blurred edge characteristics. The blur in cardiac images are mainly caused by motion artifacts of the heart. In this chapter, discussion on efficiency improvement of weighting function is perceived. We present a few functions for such purpose viz., Difference of Gaussian (DoG), Difference of Laplacian of Gaussian (DoLoG) and Laplacian of Derivative of Gaussian (LoDroG); those are aimed to produce good segmentation results on blurry edged CMR images. Laplacian operator is a suitable tool for edge detection, but it alone generates double edges [12]. In this work, the suggested functions (except DoG) are proved to be useful in improving the performance of Laplacian operator at the fundamental level.

From Equation 4.1.2, it is evident that if two pixels are close and identical, the value of w_{ij} will be high, i.e. 1. That means, higher the value of w_{ij}, better is the similarity between pixel i and j. When its value touches to zero, the two pixels are realized as heterogenous. If the weight of a pixel falls off with the growing in distance, pixels separated by large discontinuities in the image are down weighted. All these weighting functions bear the decreasing trend, defined on the distance function with different rate of fall-off. Only, those functions are included in this thesis which give such a characteristic (as shown here onwards).

For performance comparison of each function, we take a set of three images and show the effect of each weighting function during the course of implementation. It would be wise to first

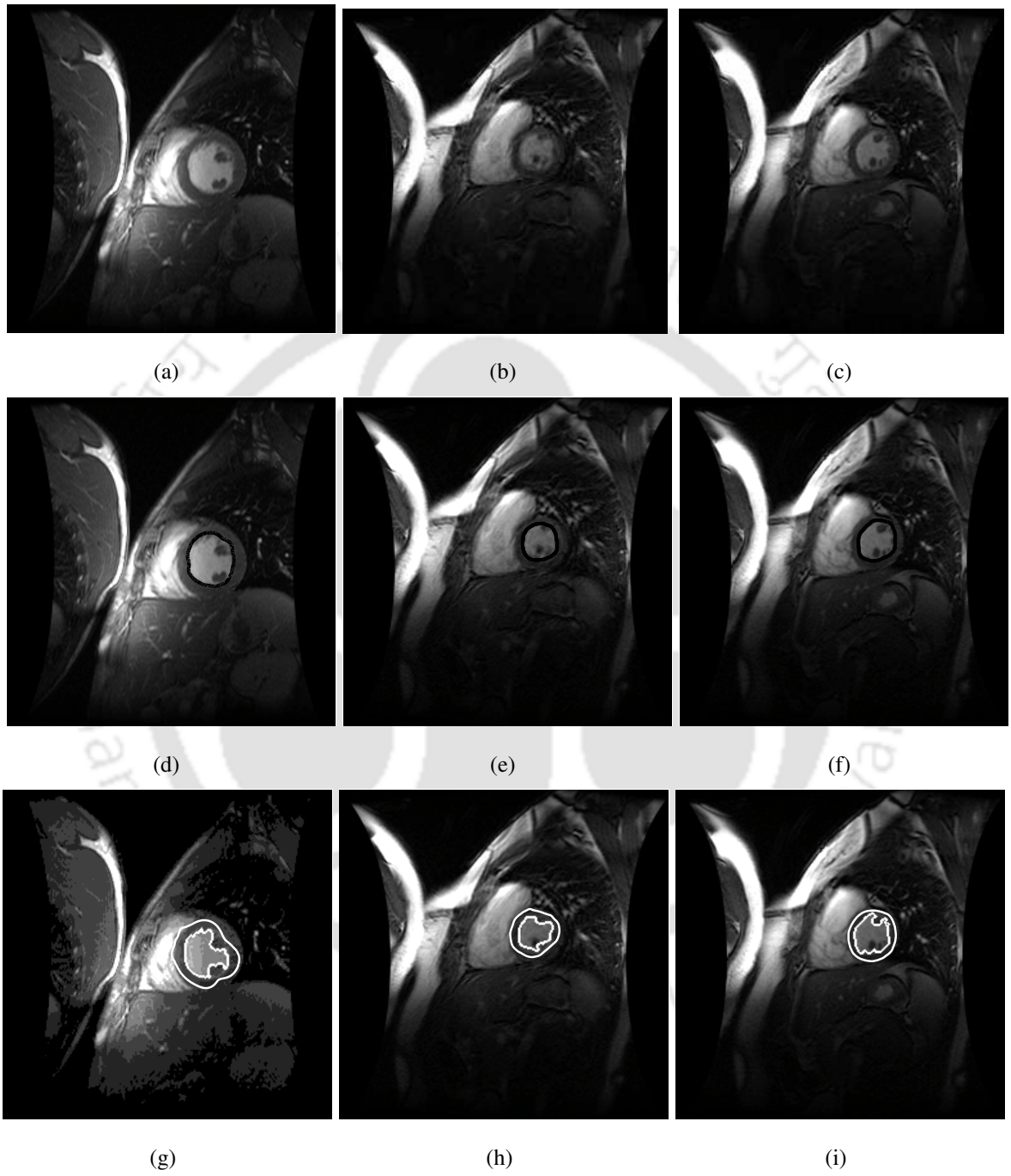

Figure 4.1: (a-c) Original CMR images. (d-f) Ground truth images. (g-i) Segmentation using Gaussian weighting function.

know the outcome of Gaussian weighting function and then one could realize the essence of any other function. Therefore, the results using this are given in Figure 4.1. The degree of realization with respect to execution of a certain weighting function is pixel intensity dependent. That means, reasonable size and contrast of LV in a CMR image leave a great impression on the reader/viewer to compare properly. Moreover, our main goal is to set up a different function other than Gaussian that could perform well in ischemic CMR images. Therefore, during the course of examination (of all the weighting functions), various CMR images apart from this three are also taken.

Mostly, difference of Gaussian function is used for the purpose of filtering. It works by performing two different Gaussian blurs on the image, with a different blurring radius for each and subtracting them to yield the result. This algorithm is very widely used in artificial vision. In this work, we use it as a weighting function instead; the analysis is described in the following section.

4.2 Difference of Gaussian Weighting Function

A blurred edge $v(x)$ can be represented by a combination of an exponential and a step function [113]:

$$v\left(x\right) = \begin{cases} e^{\left(-\frac{(x-t)^2}{2\sigma_s^2}\right)}, & x \leq t \\ 1, & x > t, \end{cases} \tag{4.2.1}$$

where t represents the width of the region of interest (ROI) and σ_s the extent of the blurring, $(0 \leqslant \sigma_s \leqslant S,\ S \in \mathbb{R})$, $\sigma_s = \begin{cases} S, & \text{blurred edge} \\ 0, & \text{sharp edge} \end{cases}$. The quantity of blurring increases with increase in S. It is known that matching (template) is often based on directly comparing grey level properties of image sub-regions. If E_c is the characteristic function of matching of an input object with the output (i.e., matching of two ROIs; due to edge and weighting function), then E_{cv}^{w} (characteristic function with respect to an edge, v, and a weighting function, w) determines if a feature is worth tracking for segmentation. A decreased magnitude of E_{cv}^{w} indicates that the edge is more likely to be segmented. In other words, the characteristic function determines the suitability of a weighting function to a particular edge for its detection.

Characteristic function : The purpose of detecting sharp changes in image brightness is to capture important events and changes in properties. Under general assumptions for an image formation model, discontinuities in image brightness are likely to correspond to various aspects

viz., discontinuities in depth, discontinuities in surface orientation, changes in material properties, variations in scene illumination, etc. Therefore, an ideal edge is modeled as unit step function. In the continuous setting, a weight is a positive measure such as $w(x)\,dx$ on some domain, which is typically a subset of a Euclidean space (presently, rather we consider pixel intensity). Here dx is Lebesgue measure [114] and is a non-negative measurable function. In this context, the weight function $w(x)$ is sometimes referred to as a density. Conceptually, the characteristic function $E_{c_v}^{w}$ is defined as:

$$E_{c_v}^{w} = \int_0^{2t} v(x)\, w(x)\, dx. \tag{4.2.2}$$

If the right hand side of Equation 4.2.2 is more, then the edge characteristic will be more dense in regard to blurring. Therefore, it must be desirable to have a lower value of $E_{c_v}^{w}$.

The Gaussian and DoG weighting function is defined as:

$$w_{Gauss}(x) = \begin{cases} \frac{1}{\sqrt{2\pi\sigma^2}} e^{\left(-\frac{x^2}{2\sigma^2}\right)}, & x \in \text{ROI} \\ 0, & \text{elsewhere,} \end{cases}$$

and

$$w_{DoG}(x) = \begin{cases} \frac{1}{\sqrt{2\pi}} \left[\frac{1}{\sigma_1} e^{-\frac{x^2}{2\sigma_1^2}} - \frac{1}{\sigma_2} e^{-\frac{x^2}{2\sigma_2^2}}\right], & x \in \text{ROI} \\ 0, & \text{elsewhere,} \end{cases} \tag{4.2.3}$$

respectively, where σ is the standard deviation. Now, the characteristic function (in 1D) due to Gaussian weighting function is

$$E_{c_v}^{Gauss} = \int_0^{2t} v(x)\, w_{Gauss}(x)\, dx. \tag{4.2.4}$$

and in case of DoG $E_{c_v}^{DoG}$ is

$$\begin{aligned} E_{c_v}^{DoG} = & \int_0^{t} \frac{1}{\sqrt{2\pi}} \left(\frac{1}{\sigma_1} e^{-\frac{x^2}{2\sigma_1^2}} - \frac{1}{\sigma_2} e^{-\frac{x^2}{2\sigma_2^2}}\right) e^{-\frac{(x-t)^2}{2\sigma_s^2}}\, dx + \\ & \int_t^{2t} \frac{1}{\sqrt{2\pi}} \left(\frac{1}{\sigma_1} e^{-\frac{x^2}{2\sigma_1^2}} - \frac{1}{\sigma_2} e^{-\frac{x^2}{2\sigma_2^2}}\right) dx \end{aligned} \tag{4.2.5}$$

where σ_1 and σ_2 represent the width of Gaussian kernel with different magnitudes. In Equation (4.2.6), σ_s is replaced by s for simplicity.

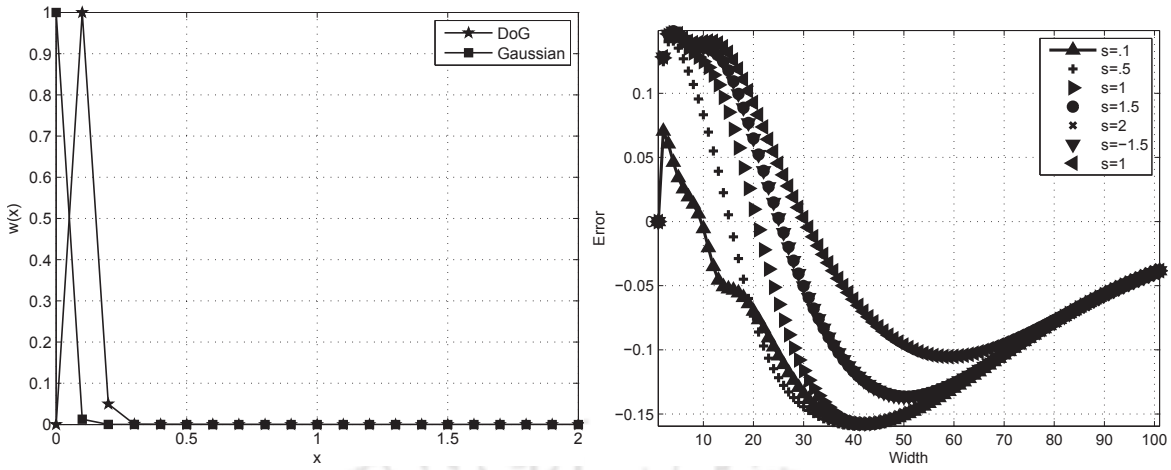

Figure 4.2: (a) Gaussian and DoG weighting function. (b) Magnitude of difference between the characteristic functions due to DoG and Gaussian weighting function.

The difference resulting between the two characteristic functions is expressed as

$$
\begin{aligned}
E_{c_v}^{DoG} - E_{c_v}^{G} \;=\; & \frac{1}{\sqrt{2\pi}\sigma_1}\left(0.5\sqrt{\frac{\pi}{\frac{1}{2s^2}+\frac{1}{2\sigma_1^2}}}e^{\frac{\left(\frac{t}{2s^2}\right)^2-\left(\frac{1}{2s^2}+\frac{1}{2\sigma_1^2}\right)\left(\frac{t^2}{2s^2}\right)}{\left(\frac{1}{2s^2}+\frac{1}{2\sigma_1^2}\right)}}\right) \\
& \left(erf\left[\sqrt{\left(\frac{1}{2s^2}+\frac{1}{2\sigma_1^2}\right)t}+\frac{\left(-\frac{t}{2s^2}\right)}{\sqrt{\left(\frac{1}{2s^2}+\frac{1}{2\sigma_1^2}\right)}}\right]-\right. \\
& \left. erf\left[\frac{\left(-\frac{t}{2s^2}\right)}{\sqrt{\left(\frac{1}{2s^2}+\frac{1}{2\sigma_1^2}\right)}}\right]\right)+\frac{1}{\sqrt{2\pi}\sigma_2}\left(0.5\sqrt{\frac{\pi}{\frac{1}{2s^2}+\frac{1}{2\sigma_2^2}}}\right. \\
& \left. e^{\frac{\left(\frac{t}{2s^2}\right)^2-\left(\frac{1}{2s^2}+\frac{1}{2\sigma_2^2}\right)\left(\frac{t^2}{2s^2}\right)}{\left(\frac{1}{2s^2}+\frac{1}{2\sigma_2^2}\right)}}\right)\left(erf\left[\sqrt{\left(\frac{1}{2s^2}+\frac{1}{2\sigma_2^2}\right)t}+\right.\right. \\
& \left.\left.\frac{\left(-\frac{t}{2s^2}\right)}{\sqrt{\left(\frac{1}{2s^2}+\frac{1}{2\sigma_2^2}\right)}}\right]-erf\left[\frac{\left(-\frac{t}{2s^2}\right)}{\sqrt{\left(\frac{1}{2s^2}+\frac{1}{2\sigma_2^2}\right)}}\right]\right)- \\
& \frac{\sqrt{\pi}\sigma\left(-erf\left[\frac{t}{\sqrt{2}\sigma}\right]\right)+erf\left[\frac{\sqrt{2}t}{\sigma}\right]}{2\sqrt{\pi\sigma^2}}-\frac{e^{-\frac{t^2}{2(s^2+\sigma^2)}}}{2\sqrt{\pi\sigma^2}} \\
& \frac{\sqrt{\pi}s\sigma}{\sqrt{s^2+\sigma^2}}\left(erf\left[\frac{st}{\sqrt{2}\sigma\sqrt{s^2+\sigma^2}}\right]+erf\left[\frac{t\sigma}{\sqrt{2}s\sqrt{s^2+\sigma^2}}\right]\right)
\end{aligned}
\tag{4.2.6}
$$

The graphical analysis of Equation (4.2.6) can be performed by varying values of t, σ, σ_1, s and σ_2. Here in order to show the effect of blurring, only σ_s is varied as shown in Figure 4.2(b). For $t \geqslant 3$, the plot shows negative values of $|E_{c_v}^{DoG} - E_{c_v}^{Gauss}|$, which means error due to DoG is less. Therefore, DoG should be considered as the better one than Gaussian for ischemic CMR image segmentation. On the other hand, as the edge variance increases (i.e. the edge becomes blurred), the plot does not show increasingly negative values of $|E_{c_v}^{DoG} - E_{c_v}^{Gauss}|$. This effect on the performance is reflected in Chapter 5 while comparing with other defined weighting functions.

Gaussian weighting function has faster decreasing rate (as shown in Figure 4.2(a)), so only close-by homogeneous points to the seed pixel are connected. On the other hand, the DoG weighting function has comparably slower decreasing rate, thereby, distant (connected nearly homogeneous) pixels are also connected [65]. For example, suppose a pixel faces expulsion from being included in the object. If we use DoG instead, it may be included, since in this case, the pixel earns more value of $weight$. All these arguments are reflected in the results as shown in the following subsection.

4.2.1 Presentation of Results

The combined segmentation (inner and outer contour) algorithm is implemented using both Gaussian and DoG weighting function. Figure 4.3 shows the improvement in segmentation using DoG. In addition, some results are shown separately in Figure 4.4 and 4.5. The performance due to DoG is surely better than that of Gaussian weighting function. The meritoriousness of DoG is significant if corresponding results in Figures 4.4(c)- 4.4(e) and 4.5(c)- 4.5(e) are compared. It may also be noted that improvement in segmentation is little possible even after the use of DoG, if the object is nearly homogeneous (for example in Figure 4.4(a) and 4.5(a)). The same criterion is also applicable to rest of the weighting functions to be discussed in this chapter. The ground truth equivalents of the test CMR images are given simultaneously (here shown in Figure 4.6) while describing other proposed functions as well. The reason of giving endocardial ground truth images lies on the fact that the shape of epicardium is based on the shape of the determined endocardium. If the inner contour is accurate, then the outer one will also be accurate (as shown in Figure 3.8). Therefore to pay more attention towards blood pool extraction, we include only endocardium ground truth images.

Still in some occasions (like in Figure 4.3(d)-4.3(f)), where papillary muscles are prominent,

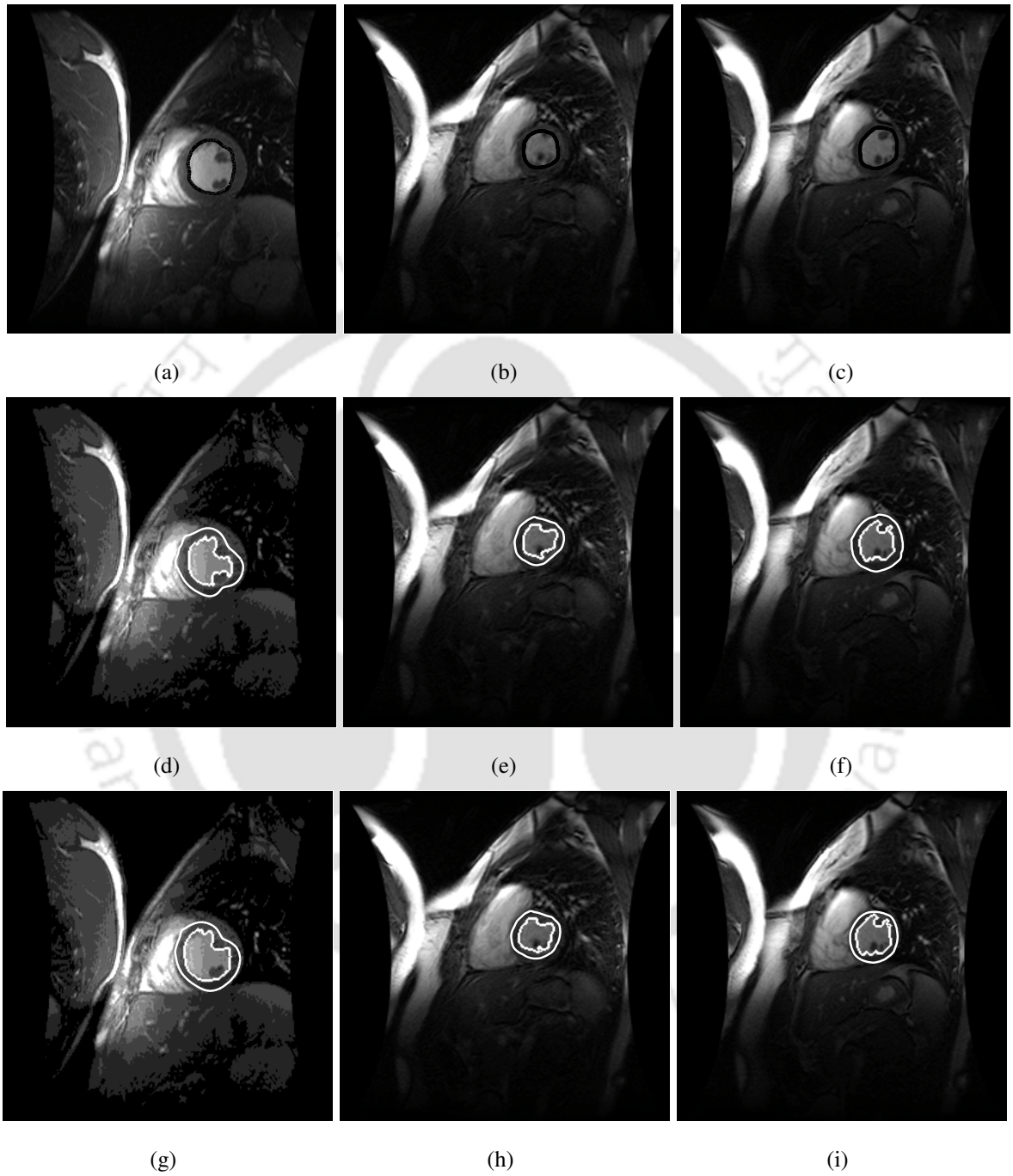

Figure 4.3: (a-c) Ground truth images. Segmentation by using (d-f) Gaussian and (g-i) DoG weighting function.

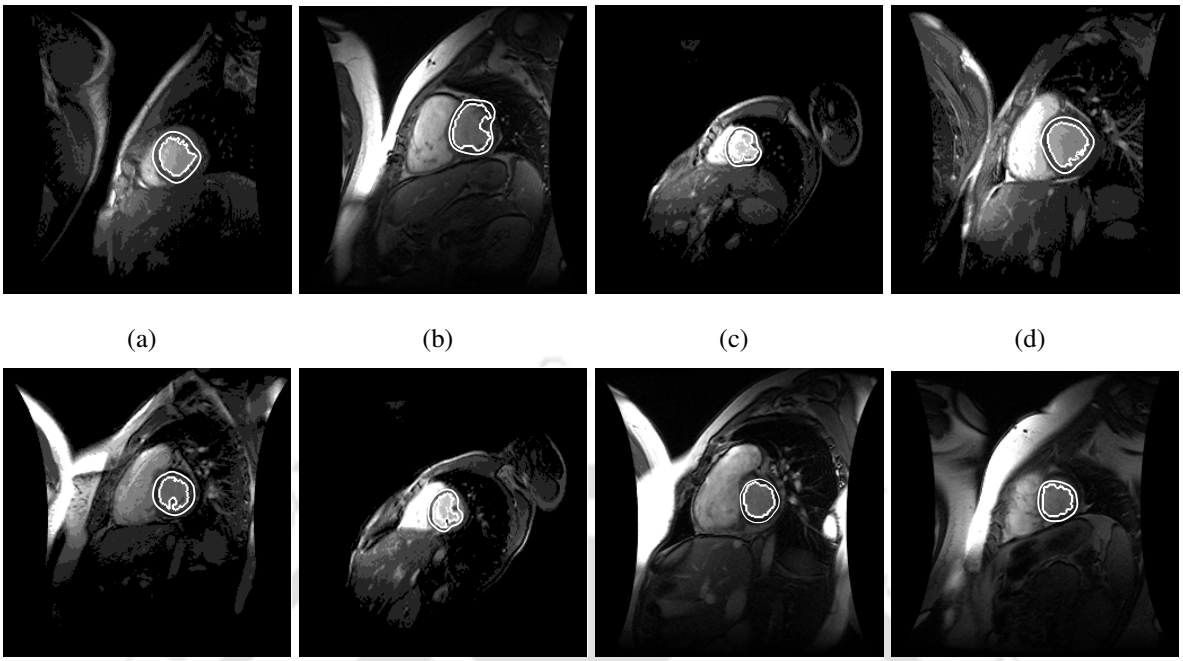

(a) (b) (c) (d)

(e) (f) (g) (h)

Figure 4.4: (a-h) Segmented slices of a subject by the combination of Random Walk approach using Gaussian weighting function and active contour model.

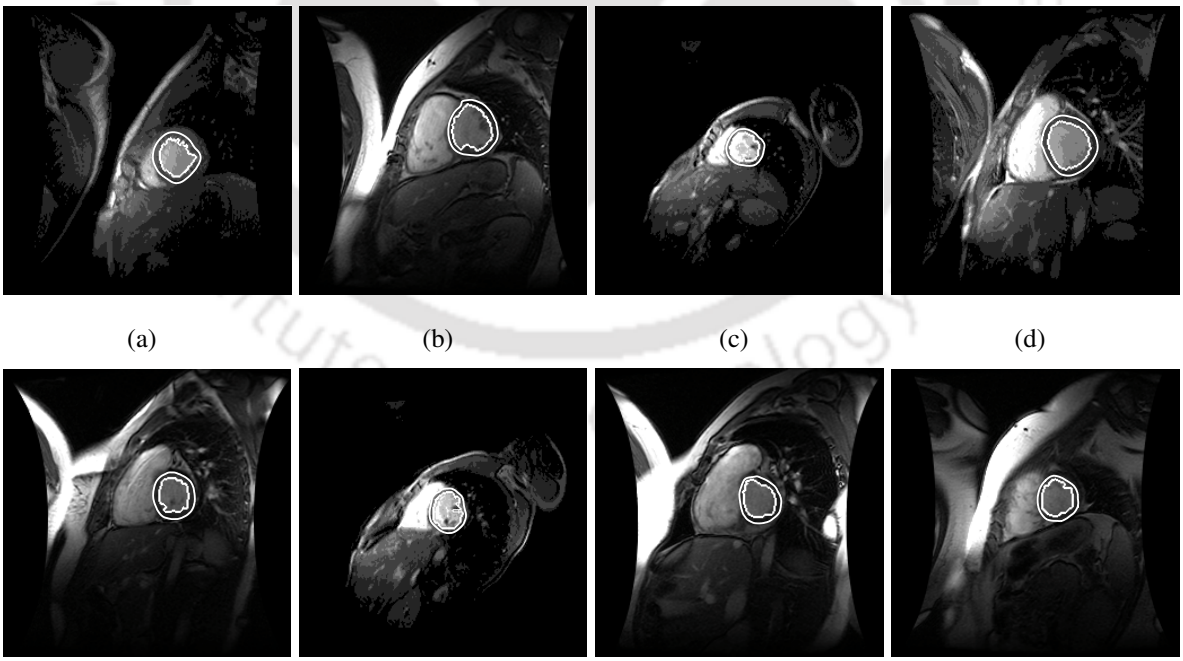

(a) (b) (c) (d)

(e) (f) (g) (h)

Figure 4.5: (a-h) Segmented slices of a subject by the combination of Random Walk approach using DoG weighting function and active contour model.

more improvement is desirable. Meanwhile, the curve (shown in Figure 4.2(b)) indicates little significant characteristic of DoG to produce a very good result, therefore, we try to opt for other possible alternative. The segmentation algorithm produces precise outputs when the value of β is accurate, whether it is obtained from the method discussed earlier or any modification (as being discussed). Sometimes, background region is insufficient in some long axis data also. Thus it is too difficult to get an accurate segmentation in such images, even if β is obtained by the method described in Chapter 2. Therefore, some long axis CMR images have also been included in this experiment as well.

The edges characterize object boundaries and are therefore useful for segmentation. Ideally, an edge is a jump in intensity. An ideal edge is a discontinuity (i.e., a ramp with an infinite slope). The first derivative assumes a local maximum at an edge. For a continuous image $I(x, y)$, two directional directives are considered. The gradient magnitude and gradient orientation can be expressed in terms of these directional derivatives. The local maxima of the gradient magnitude identify edges. When the first derivative achieves a maximum, the second derivative is zero. For this reason, an alternative edge-detection strategy is to locate zeros of the second derivatives of $I(x, y)$. The differential operator used in these so-called zero-crossing edge detectors is the Laplacian. Laplacian operator is a second derivative operator often used in edge detection, but it alone generates double edges [115]. Efficient utilization of its characteristics may be achieved, if it is further associated with DoG as described below.

4.3 Difference of Laplacian of Gaussian Weighting Function

The edges can be extracted by the detection of regions which involve abrupt changes of brightness; difference operators are usually used to detect edges. In this thesis, we employ the difference operator using entropy in association with Laplacian operator. It is well known that the Laplacian is a operator and rotation invariant. The entropy operator calculates the entropy of brightness in a local region of the picture. The entropy value is maximum when the brightness in the region is uniform, and the value is small when the brightness changes abruptly. So the regions where the entropy is small contain edges [88].

The Difference of Laplacian of Gaussian (DoLoG) weighting function is defined as

$$w_{DoLoG} \triangleq w_{LoG_{\sigma_1}} - w_{LoG_{\sigma_2}} \tag{4.3.1}$$

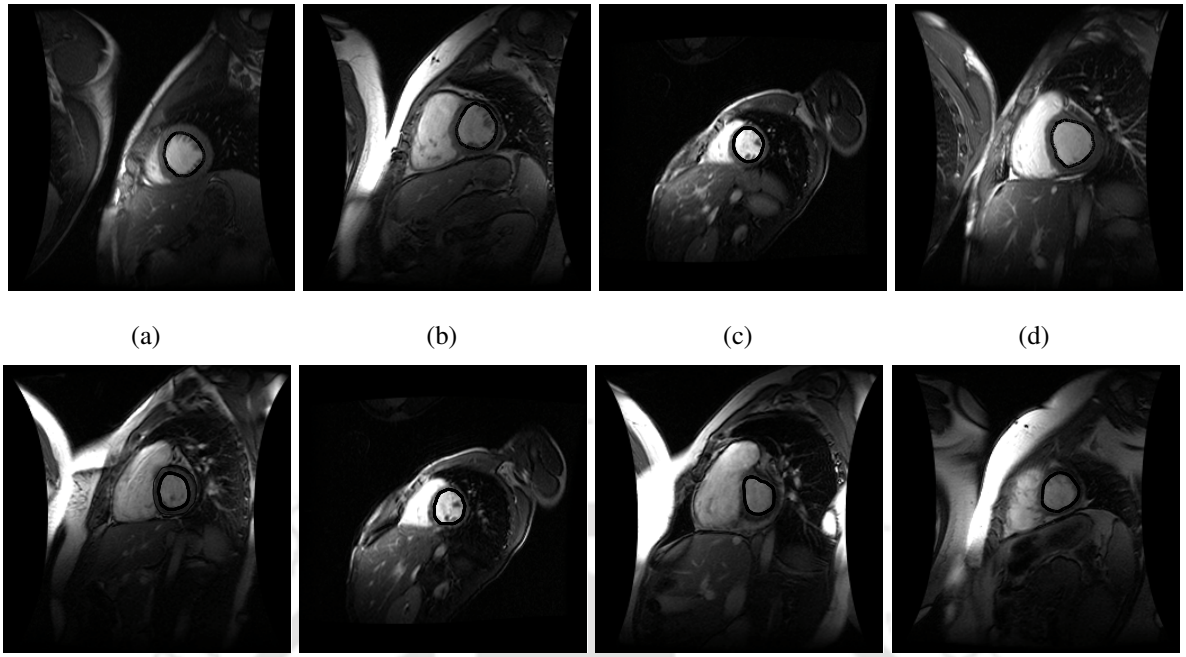

(a) (b) (c) (d)

(e) (f) (g) (h)

Figure 4.6: (a-h) Ground truth images of Figure 4.4.

where w_{LoG} is the Laplacian of Gaussian weighting function and is given by

$$w_{LoG} = w_{LoG}(x) = \frac{x^2 - 2\sigma^2}{\sigma^4} e^{-\frac{x^2}{2\sigma^2}} \tag{4.3.2}$$

So Equation 4.3.1 becomes

$$w_{DoLoG} = \frac{x^2 - 2\sigma_1^2}{\sigma_1^4} e^{-\frac{x^2}{2\sigma_1^2}} - \frac{x^2 - 2\sigma_2^2}{\sigma_2^4} e^{-\frac{x^2}{2\sigma_2^2}} \tag{4.3.3}$$

Let the characteristic function due to DoLoG weighting function be

$$E_{cv}^{DoLoG} = \int_0^{2t} v(x)\, w_{DoLoG}(x)\, dx. \tag{4.3.4}$$

The difference between the characteristic functions is expressed as

$$
\begin{aligned}
E_{cv}^{DoLoG} - E_{cv}^{Gauss} = \\
&\sqrt{\frac{1}{2\pi}}\left[\frac{1}{\sigma_1^3}\left(-2\sqrt{2\pi}\sigma_1\left\{erf\left(\frac{\sqrt{2}}{\sigma_1}t\right) - erf\left(\frac{1}{\sqrt{2}\sigma_1}t\right)\right\}\right.\right. \\
&\left.\left.+\frac{1}{\sigma_1}\sqrt{\frac{1}{2}}\left(\frac{1}{\sigma_1}\right)^{-\frac{3}{2}}\left(\Gamma\left(1.5, \frac{2t^2}{\sigma_1^2}\right) - \Gamma\left(1.5, \frac{t^2}{2\sigma_1^2}\right)\right)\right)\right. \\
&\left.-\frac{1}{\sigma_2^3}\left(-2\sqrt{2\pi}\sigma_2\left\{erf\left(\frac{\sqrt{2}}{\sigma_2}t\right) - erf\left(\frac{1}{\sqrt{2}\sigma_2}t\right)\right\}\right.\right. \\
&\left.\left.+\frac{1}{\sigma_2}\sqrt{\frac{1}{2}}\left(\frac{1}{\sigma_2}\right)^{-\frac{3}{2}}\left(\Gamma\left(1.5, \frac{2t^2}{\sigma_2^2}\right) - \Gamma\left(1.5, \frac{t^2}{2\sigma_2^2}\right)\right)\right)\right. \\
&+\frac{1}{\sigma_1^3}\left(-2\sqrt{\frac{\pi}{2\left(\frac{1}{\sigma_s^2}+\frac{1}{\sigma_1^2}\right)}}\, e^{\frac{\left(\frac{t}{\sigma_s^2}\right)^2 - \left(\frac{1}{\sigma_s^2}+\frac{1}{\sigma_1^2}\right)\left(\frac{t^2}{2\sigma_s^2}\right)}{2\left(\frac{1}{\sigma_s^2}+\frac{1}{\sigma_1^2}\right)}}\right. \\
&\left\{erf\left(\left(\sqrt{\frac{1}{2\sigma_s^2}+\frac{1}{2\sigma_1^2}}t\right) - \frac{\frac{t}{\sigma_s^2}}{\sqrt{2\left(\frac{1}{\sigma_s^2}+\frac{1}{\sigma_1^2}\right)}}\right) - \right. \\
&\left.\left.erf\left(\frac{-\frac{t}{\sigma_s^2}}{\sqrt{2\left(\frac{1}{\sigma_s^2}+\frac{1}{\sigma_1^2}\right)}}\right)\right\} + \frac{1}{\sigma_1}e^{\left(1+\frac{\ln\left(t^2-2\right) - \left(\frac{1}{\sigma_s^2}+\frac{1}{\sigma_1^2}\right)\left(\frac{t^2}{6}\right) + \frac{t^2}{4\sigma_s^2}}{te^{-\left(\frac{1}{\sigma_s^2}+\frac{1}{\sigma_1^2}\right)\frac{t^2}{2}}}\right)}\right) \\
&-\frac{1}{\sigma_2^3}\left(-2\sqrt{\frac{\pi}{2\left(\frac{1}{\sigma_s^2}+\frac{1}{\sigma_2^2}\right)}}\, e^{\frac{\left(\frac{t}{\sigma_s^2}\right)^2 - \left(\frac{1}{\sigma_s^2}+\frac{1}{\sigma_2^2}\right)\left(\frac{t^2}{2\sigma_s^2}\right)}{2\left(\frac{1}{\sigma_s^2}+\frac{1}{\sigma_2^2}\right)}}\right. \\
&\left\{erf\left(\left(\sqrt{\frac{1}{2\sigma_s^2}+\frac{1}{2\sigma_2^2}}t\right) - \frac{\frac{t}{\sigma_s^2}}{\sqrt{2\left(\frac{1}{\sigma_s^2}+\frac{1}{\sigma_2^2}\right)}}\right) - \right. \\
&\left.\left.erf\left(\frac{-\frac{t}{\sigma_s^2}}{\sqrt{2\left(\frac{1}{\sigma_s^2}+\frac{1}{\sigma_2^2}\right)}}\right)\right\} + \frac{1}{\sigma_2}e^{\left(1+\frac{\ln\left(t^2-2\right) - \left(\frac{1}{\sigma_s^2}+\frac{1}{\sigma_2^2}\right)\left(\frac{t^2}{6}\right) + \frac{t^2}{4\sigma_s^2}}{te^{-\left(\frac{1}{\sigma_s^2}+\frac{1}{\sigma_2^2}\right)\frac{t^2}{2}}}\right)}\right) \\
&-\frac{1}{\sigma}\sqrt{\frac{\pi}{2}}\left\{\sigma\left(erf\left(\frac{\sqrt{2}t}{\sigma}\right) - erf\left(\frac{t}{\sqrt{2}\sigma}\right)\right) + \sigma_s\sigma\frac{e^{-\left(\frac{t^2}{2(\sigma^2+\sigma_s^2)}\right)}}{\sqrt{\sigma^2+\sigma_s^2}}\right. \\
&\left.\left\{erf\left(\frac{t\sigma}{\sqrt{2}\sigma_s\sqrt{\sigma^2+\sigma_s^2}}\right) + erf\left(\frac{t\sigma_s}{\sqrt{2}\sigma\sqrt{\sigma^2+\sigma_s^2}}\right)\right\}\right\}
\end{aligned}
\tag{4.3.5}
$$

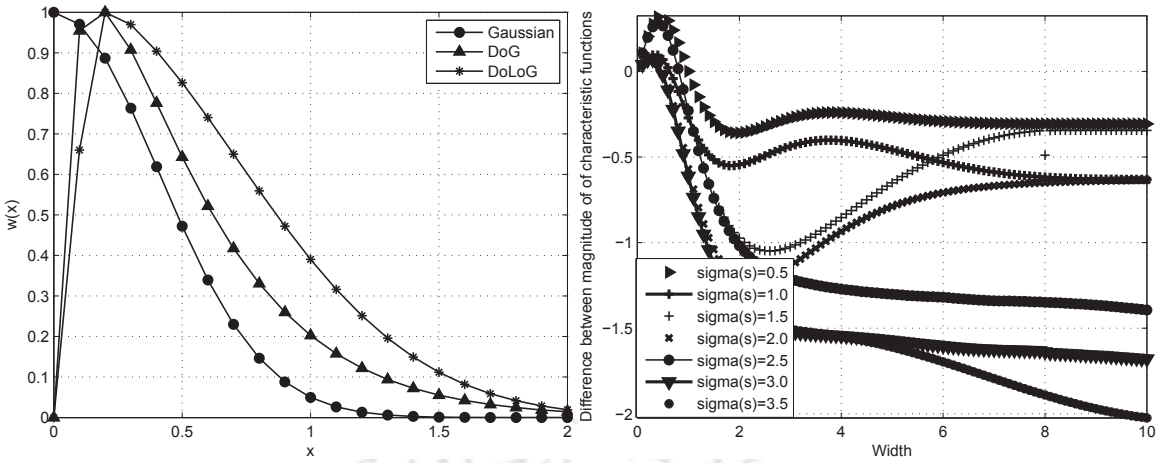

Figure 4.7: (a) Gaussian, DoG and, DoLoG weighting function. (b) Magnitude of difference between the characteristic functions due to DoLoG and Gaussian weighting function.

The evaluation of Equation (4.3.5) is necessary to ascertain the said function's performance and make an expression of demand for its use. Like DoG, all the parameters except σ_s are kept constant. In case of small values of edge variance (steeper edge) σ_s, the plot shows negative values of $\left(|E_v^{DoLoG} - E_v^{Gauss}|\right)$ when $t \geq 1$ (as shown in Figure 4.7(b)). Still, it is observed that with increase in t, the curves corresponding to lower values of σ_s, are not monotonically decreasing (shown in Figure 4.7(b)). But, this aspect is better than DoG, if the curves in this higher range of σ_s are considered. As the edge variance increases (i.e. the edge becomes blurred), for example when σ_s=2.5, 3.0 and 3.5, unlike DoG, the plot shows increasingly negative values of $\left(|E_v^{DoLoG} - E_v^{Gauss}|\right)$. This implies that DoLoG has consistently lower error values than the Gaussian weighting function if at all the quantity of blur is more. This indicates the efficiency of DoLoG on blurry edged objects.

Additionally, DoLoG has a slower decreasing rate (as shown in Figure 4.7(a)) as compared to that of Gaussian weighting function. The combination of these two factors of DoLoG dictate it to produce a better segmentation, when it is used as the desired weighting function alternative to Gaussian.

4.3.1 Presentation of Results

Figure 4.8 presents the results obtained using DoLoG function. Additionally, some other images from the data-set (ground truth equivalents) are shown in Figure 4.11. Figure 4.9(a)-4.9(h) are the results of the algorithm due to Gaussian and Figure 4.10(a)-4.10(h) are the correspond-

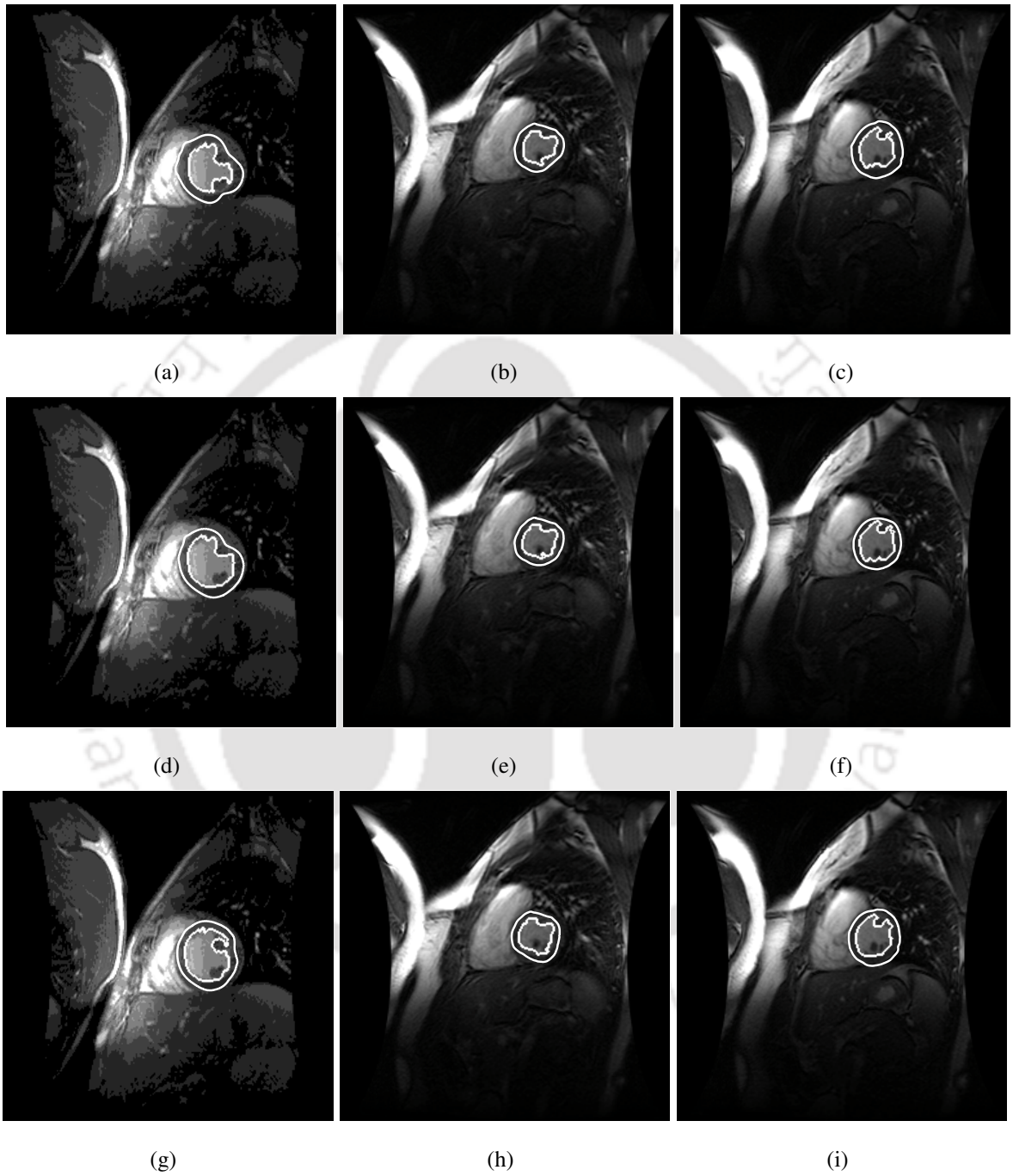

Figure 4.8: Segmentation by using (a-c) Gaussian, (d-f) DoG and (g-i) DoLoG weighting function.

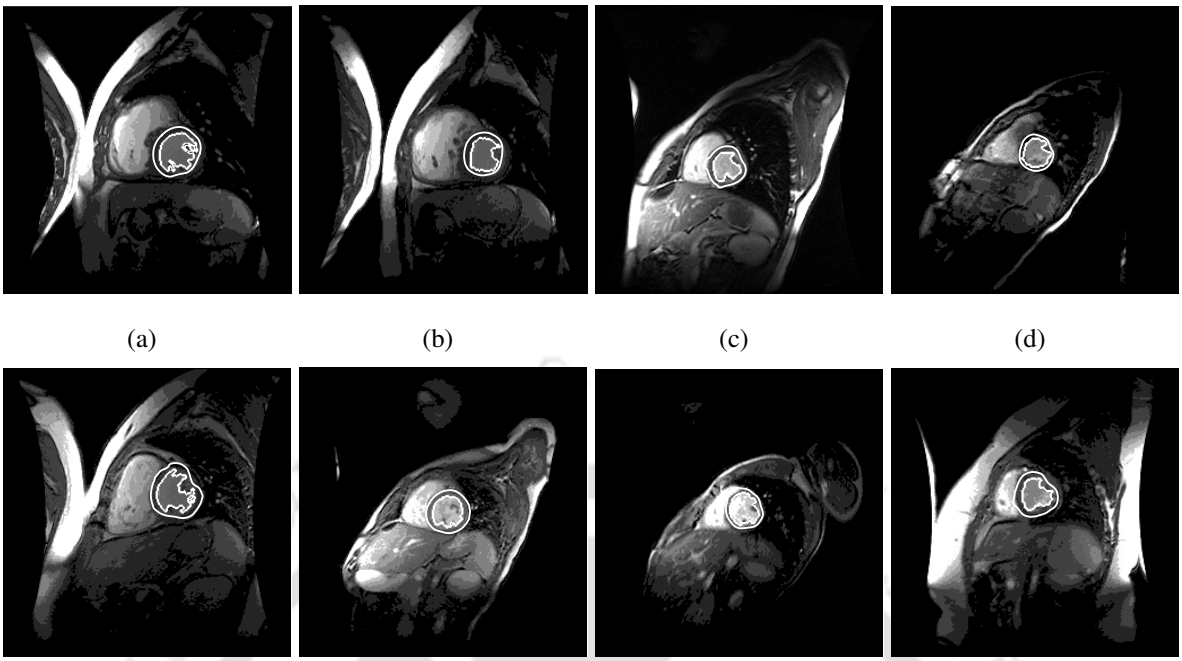

(a) (b) (c) (d)

(e) (f) (g) (h)

Figure 4.9: (a-h) Segmentation of CMR images by the proposed method using Gaussian weighting function.

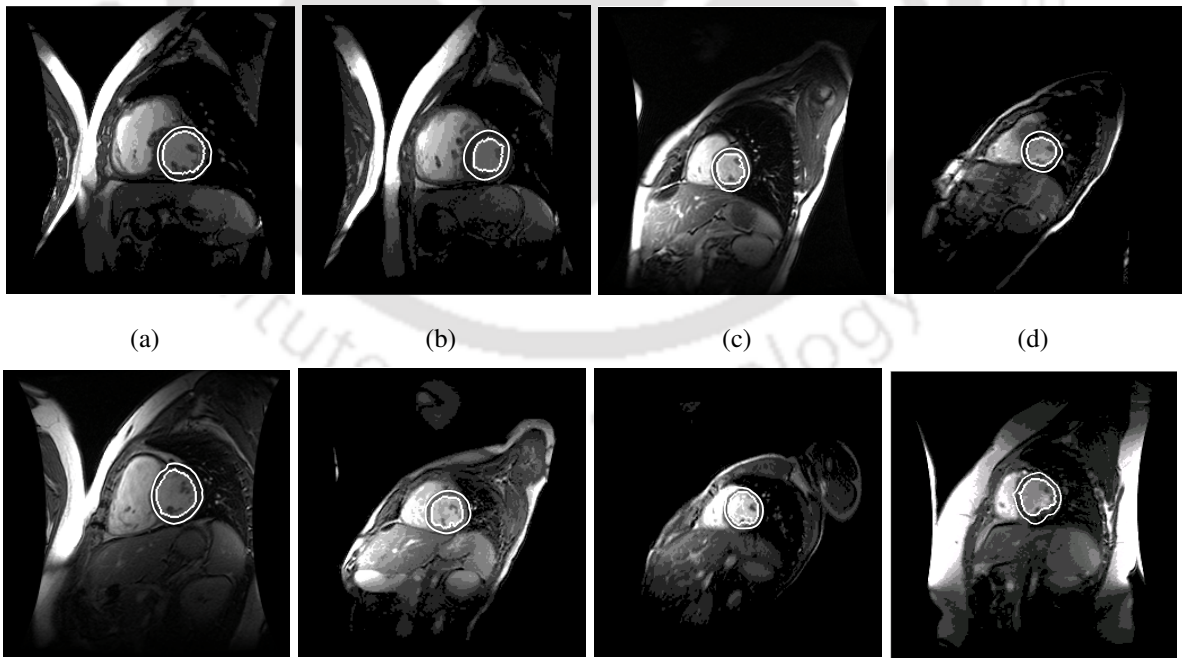

(a) (b) (c) (d)

(e) (f) (g) (h)

Figure 4.10: (a-h) Segmentation of CMR images by the proposed method using DoLoG weighting function.

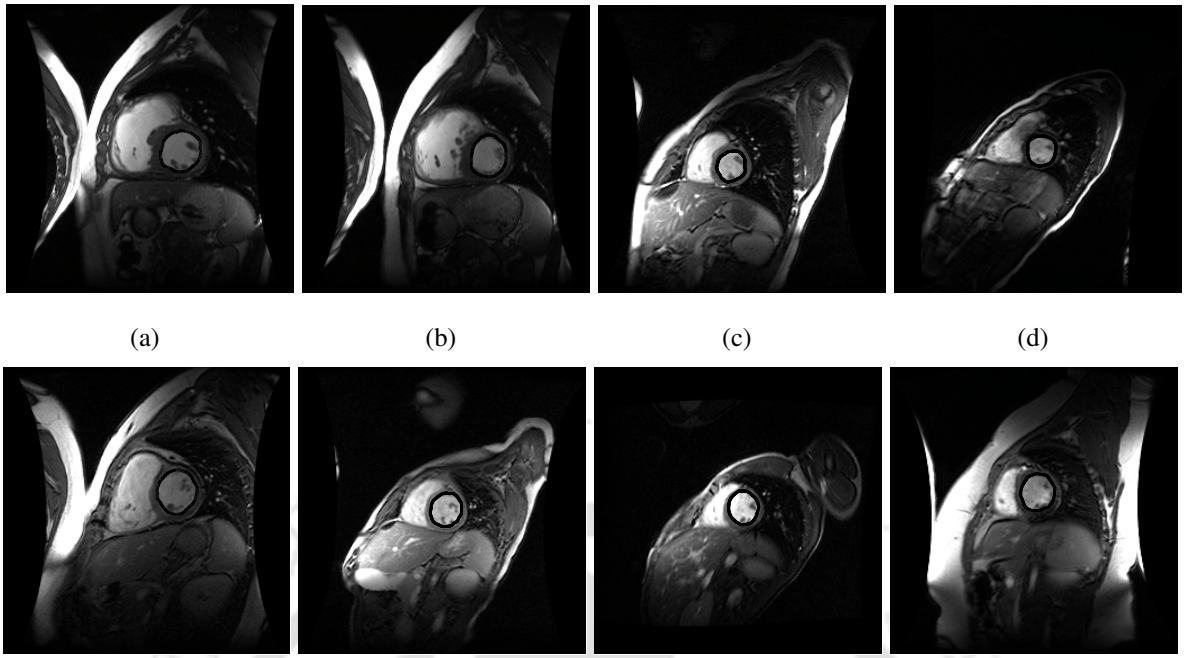

(a) (b) (c) (d)

(e) (f) (g) (h)

Figure 4.11: (a-h) Ground truth images of Figure 4.9.

ing results obtained using DoLoG weighting function. It is observed that DoloG successfully includes the papillary muscles in the blood pool unlike Gaussian weighting function.

The results of DoLoG is obviously better than that of DoG. On the other hand, looking at the ground truth equivalents of the corresponding images, more improvement is further desirable. The following weighting function serves better to a large extent.

4.4 Laplacian of Derivative of Gaussian Weighting Function

The derivative of the Gaussian function ($Gauss(x)$) with respect to x is obtained [116] by,

$$\frac{\partial^n}{\partial x^n} Gauss\,(x) = (-1)^n \frac{1}{\left(\sigma\sqrt{2}\right)^n} H_n\left(\frac{x}{\sigma\sqrt{2}}\right) Gauss\,(x) \tag{4.4.1}$$

where n is the order of the derivative and $H_n\,(x)$ is the Hermite polynomial. In this case we take $n = 1$. The Laplacian of derivative of Gaussian weighting function is

$$w_{LoDroG}\,(x) = w_{LoDroG} = \frac{1}{2\sqrt{2\pi}\sigma^3} e^{-\frac{x^2}{2\sigma^2}} \left(\frac{x^2}{\sigma^2} - 1\right) \tag{4.4.2}$$

The characteristic function due to LoDroG is

$$E_{c_v}^{LoDroG} = \int_0^{2t} v\,(x)\, w_{LoDroG}\,(x)\, dx. \tag{4.4.3}$$

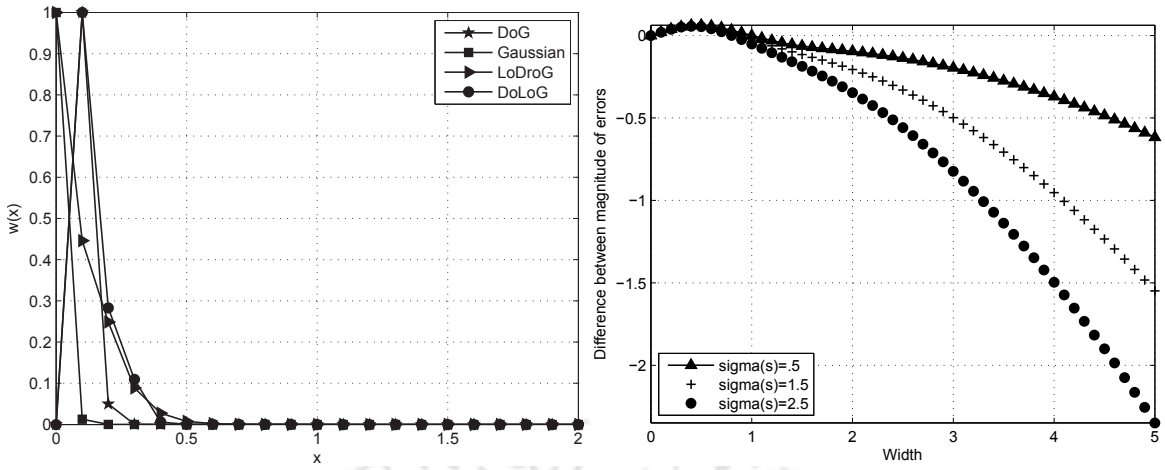

Figure 4.12: (a) Gaussian, DoG, DoLoG, and LoDroG weighting function. (b) Magnitude of difference between the characteristic functions due to LoDroG and Gaussian.

The difference between two characteristic functions is expressed as

$$
\begin{aligned}
E_{c_v}^{LoDroG} - E_{c_v}^{Gauss} = \sqrt{\frac{1}{2\pi\sigma^2}} \Bigg[& \frac{1}{\sigma^4} e^{\left(1+\frac{\ln\left(t^2-2\right)-\left(\frac{1}{2\sigma_s^2}+\frac{1}{2\sigma^2}\right)\left(\frac{t^2}{3}\right)+\frac{t^2}{4\sigma_s^2}}{e^{-\left(\frac{1}{2\sigma_s^2}+\frac{1}{2\sigma^2}\right)t^2}}\right)} - \left(\frac{\sqrt{\pi}}{2\sigma^2\left(\frac{1}{2\sigma_s^2}+\frac{1}{2\sigma^2}\right)^{\frac{3}{2}}}\right. \\
& \left(\left(\frac{t}{2\sigma_s^2}\right)^2 - \left(\frac{1}{2\sigma_s^2}+\frac{1}{2\sigma^2}\right)\frac{t^2}{2\sigma_s^2}\right)\left\{erf\left(\left(\sqrt{\frac{1}{2\sigma_s^2}+\frac{1}{2\sigma^2}}t\right)\right.\right. \\
& \left.\left.\left. - \frac{\frac{t}{2\sigma_s^2}}{\sqrt{\frac{1}{2\sigma_s^2}+\frac{1}{2\sigma^2}}}\right) - erf\left(\frac{-\frac{t}{2\sigma_s^2}}{\sqrt{\frac{1}{2\sigma_s^2}+\frac{1}{2\sigma^2}}}\right)\right\}\right)\left(1-\frac{1}{\sqrt{2\pi}}\right) + \\
& \frac{1}{2\sigma^{\frac{11}{2}}}\left(\Gamma\left(1.5,\frac{2t^2}{\sigma^2}\right) - \Gamma\left(1.5,\frac{t}{2\sigma^2}\right)\right) - \sqrt{\frac{\pi}{2}}\sigma \\
& \left\{erf\left(\sqrt{\frac{2}{\sigma^2}}t\right) - erf\left(\sqrt{\frac{1}{2\sigma^2}}t\right)\right\}\left(\frac{1}{\sigma^2}-1\right)\Bigg]
\end{aligned}
\tag{4.4.4}
$$

where $erf\,(x) = \frac{2}{\sqrt{\pi}}\int_0^x e^{-t^2}dt$, $A = \left(\frac{1}{2\sigma_s^2}+\frac{1}{2\sigma_2^2}\right)$ and $\Gamma\,(a,x) = \int_z^\infty e^{-t}t^{a-1}dt$.

Similar to previous discussions, the graphical analysis of Equation (4.4.4) is possible by varying values of t, σ, σ_1, s and σ_2. To retain the objective like previous, σ_s is varied (e.g. σ_s=0.5, 1.5 and 2.5) as shown in Figure 4.12(b). For small values of edge variance σ_s (steeper edge), the plot shows negative values of $|E_{c_v}^{LoDroG} - E_{c_v}^{Gauss}|$ when $t \geq 1$. Simultaneously, it is also observed that with increase in t, the curves corresponding to low values of σ_s are monotonically decreasing, though small. As the edge variance increases (i.e. the edge becomes blurred), the plot

shows increasingly negative values of $|E_{cv}^{LoDroG} - E_{cv}^{Gauss}|$. This implies, with a blurred edge, LoDroG has consistently lower error values than the Gaussian weighting function. Therefore, we must choose LoDroG instead of Gaussian as the weighting function for the Random Walk approach, while applying on blurry edged CMR images.

The LoDroG has moderate decreasing rate as compared to Gaussian, DoG and DoLoG weighting function (as shown in Figure 4.12(a)). Thereby, distant connected and similar pixels are also connected with the pixel marked by the initial seed. These two factors are responsible to produce a better segmentation with the use of LoDroG as the weighting function.

4.4.1 Presentation of Results

Figure 4.13(g)-4.13(i) exhibit the improved performance of LoDroG over DoLoG and DoG weighting function. Since the Gaussian function was used primarily to segment normal images (as reported in [67]), to specify the degree of superiority of LoDroG over Gaussian, the combined segmentation algorithm is implemented using both the weighting functions. Some CMR images from the data-set (ground truth equivalents) are given in Figure 4.16 in order to indicate the intensity distribution in LV. The results are shown in Figure 4.14 and 4.15, and it is quite evident that the performance due LoDroG is much better than that of Gaussian weighting function. It is also discernible that papillary muscles are well segmented indicating the efficiency of LoDroG unlike Gaussian and DoG (and to some extent DoLoG) weighting function. The combined approach is summarized as shown in Figure 4.17.

A brief discussion of Derivative of Gaussian as a weighting function is given in the Appendix. From all these above discussions, the suggested weighting functions are evident to have a significant upper edge over Gaussian. In all the result sections, the ground truth images have been included to let the readers a feel the intensity distribution and the desired boundary. The characteristic functions really depict the relative importance of each weighting function. Among all the curves, LoDroG is learnt to produce monotonically decreasing characteristic with increase in width 't' and blurring 'σ_s'. The segmentation performance of LoDroG is reckoned as best. Though at some instants, the segmentation results looked similar, if they are observed carefully, one can perceive the difference.

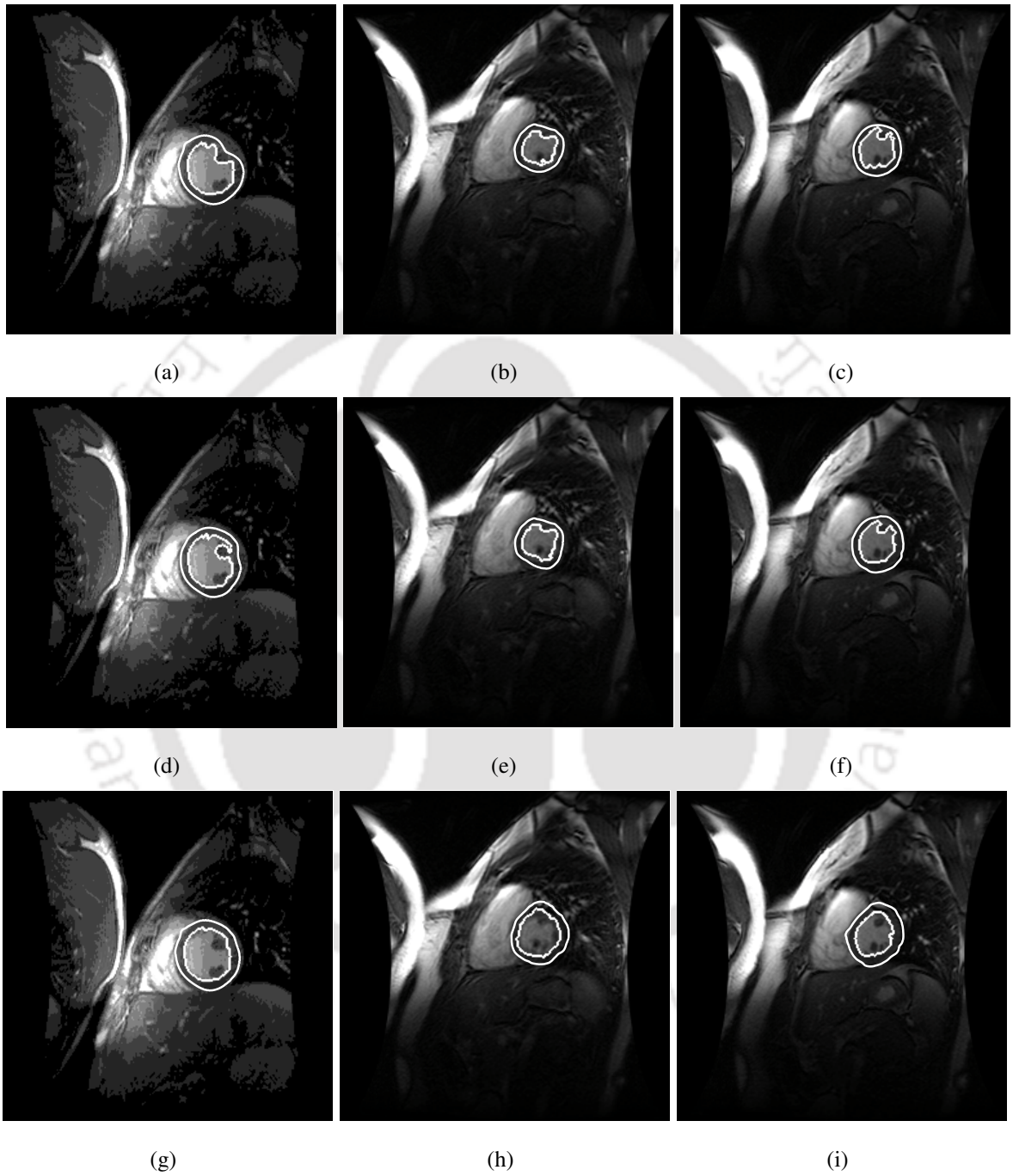

Figure 4.13: Segmentation by using (a-c) DoG, (d-f) DoLoG and (g-i) LoDroG weighting function.

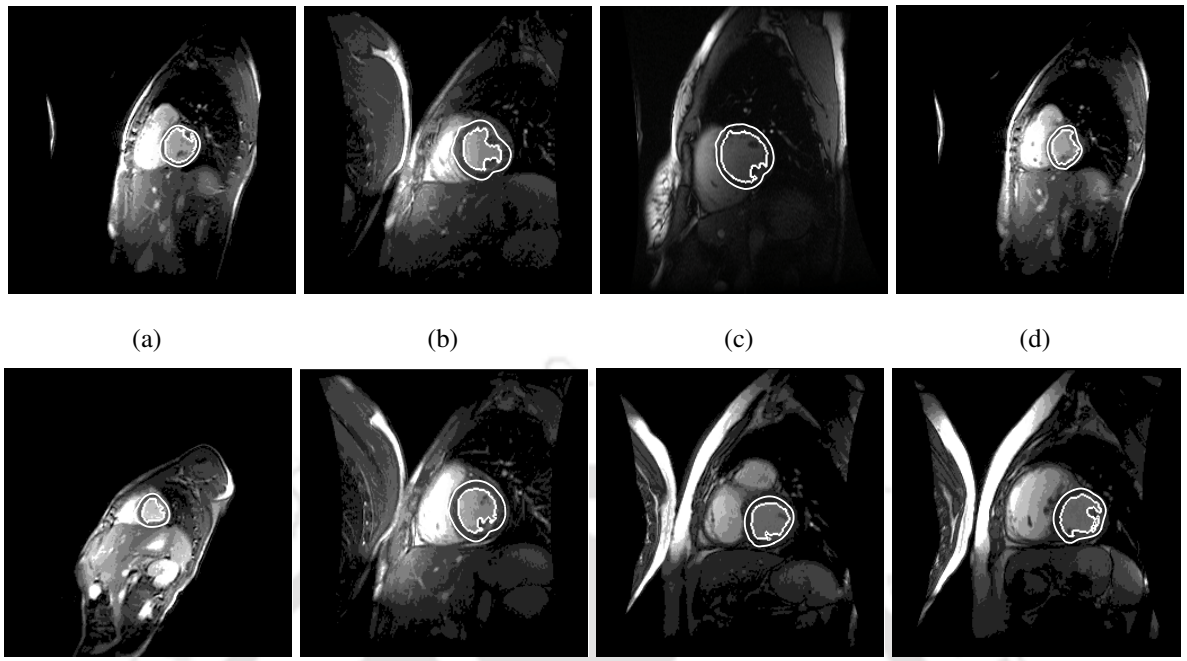

(a) (b) (c) (d)

(e) (f) (g) (h)

Figure 4.14: (a-h) Segmented slices of a subject with Random Walk approach using Gaussian weighting function and active contour model.

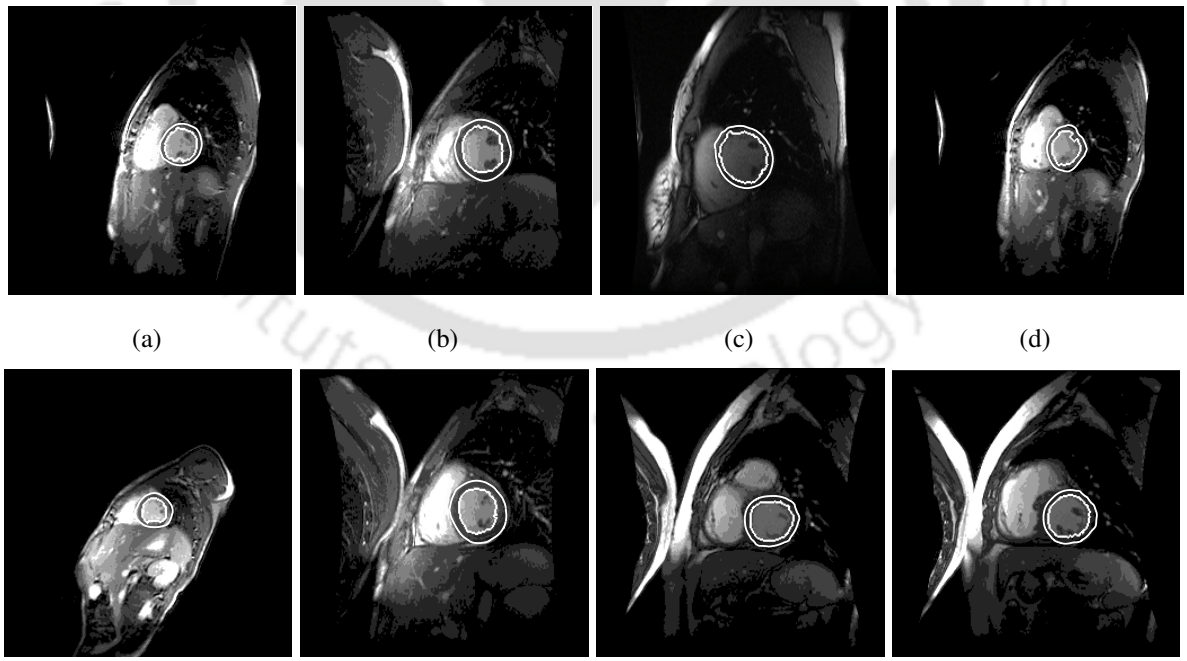

(a) (b) (c) (d)

(e) (f) (g) (h)

Figure 4.15: (a-h) Segmented slices of a subject with Random Walk approach using LoDroG weighting function and active contour model.

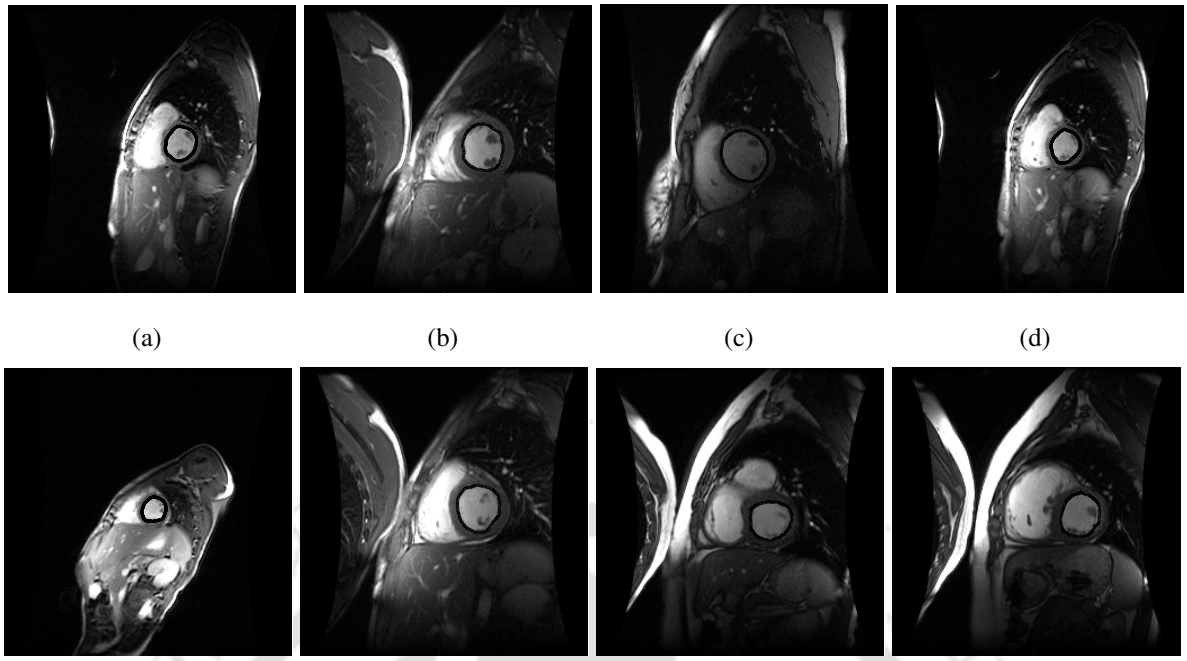

(a) (b) (c) (d)

(e) (f) (g) (h)

Figure 4.16: (a-h) Ground truth images of Figure 4.14.

4.5 Conclusions

Weighting function is an important constituent in a Random Walk based image segmentation. Gaussian function is reported as better on images, where objects are homogeneous and well distinct. On the other hand, ischemic CMR images bear neither of the two. Since background region (even the constant signal region) is insufficient in short axis CMR images, we therefore focussed mainly on weighting function. The performance of the algorithm mostly depends on the proper description of the function. In this chapter, an attempt has been made to explore its detailed aspects on segmentation performance. After a sound study on entropy, we have discussed four functions, viz. DoG, DoLoG and LoDroG in this work. The reasonable and meaningful outputs [117] describe the potential of these functions, irrespective of short or long axis CMR image, when are used with Random Walk. The quantitative evaluation of these weighting functions is performed in the next chapter (Chapter 5).

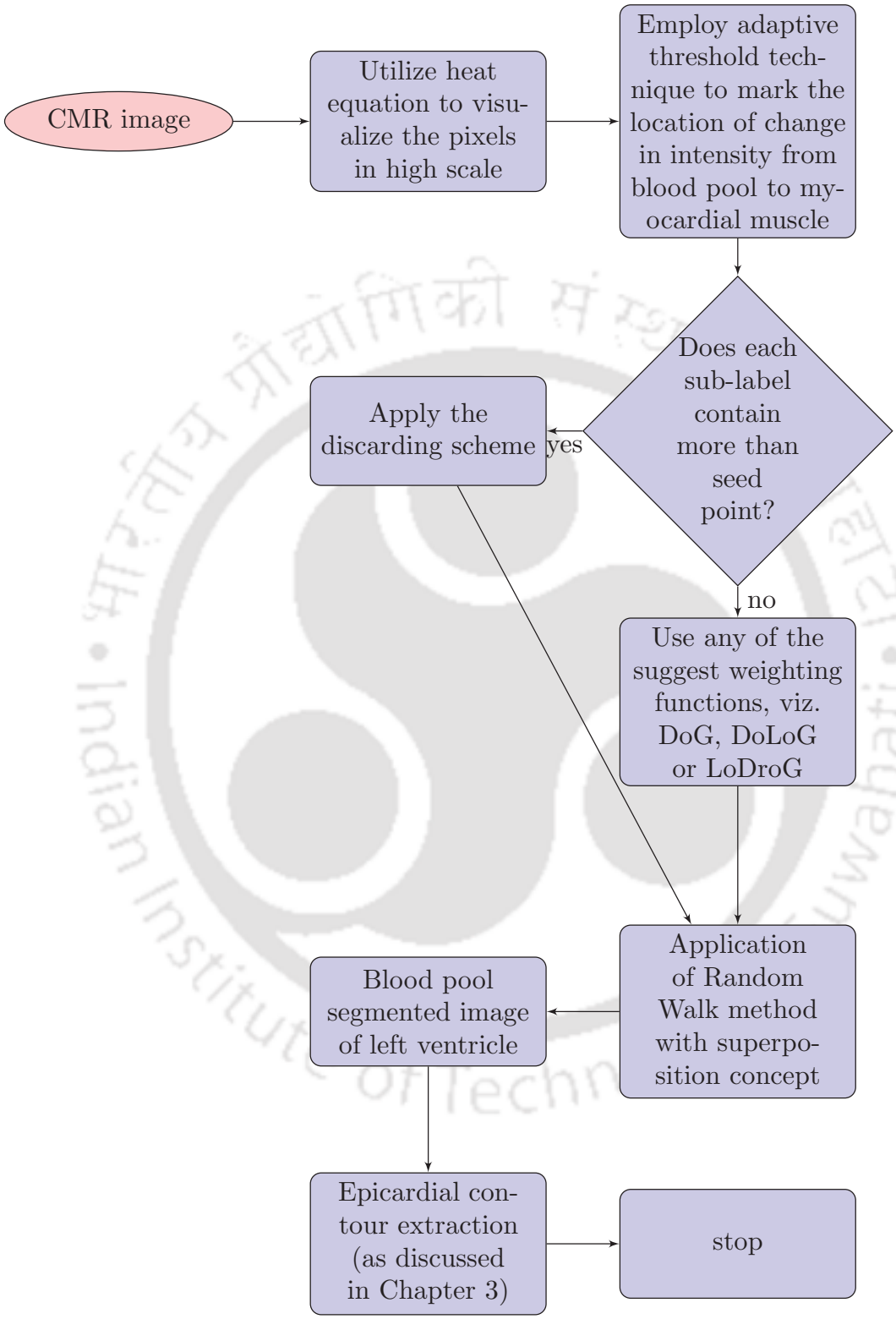

Figure 4.17: Summary of the proposed algorithm.

Chapter 5

Quantitative Evaluation of Segmentation Due to Different Weighting Functions

Quantitative evaluation of a segmentation method is necessary to find its utility in various applications. Of course, many methods have been proposed and more are coming on segmentation with increase in type of heart diseases; complexity with respect to pixel intensity in the CMR image is its result. The diversity in the types of regions composing an image is a major problem in segmentation. Mostly, an image is composed of uniform, textured or degraded regions. Good results for each type of region are obtained by a few segmentation methods. Moreover, a new segmentation method usually shows its efficiency illustrating through only a few segmentation results on benchmark images. That means, visual evaluation is still subjective that differs from person to person. Thus, the comparison of different segmentation methods is not an easy task. Moreover, despite the fact that there exists a larger number of segmentation algorithms, computer vision still suffers from an overload of written information and lack of good evaluations and comparisons. Typically, there are two reasons for this: 1) most of the algorithms are not freely available and their re-implementation is often too tedious and time-consuming, and 2) there is not a common database (rare availability of such databases publicly) used in each segmentation method, sometimes the databases are pathologically different. In order to make an objective comparison of different segmentation methods or results, some evaluation criteria have already been defined in literature.

In the course of evaluation, it is natural that a conventional thought on three basic popular edge detection algorithms, viz., 1) Prewitt [118], 2) Canny [119], and 3) Sobel [120] operator, self arises. Therefore, their performances should be considered on the experimental data-set. Since

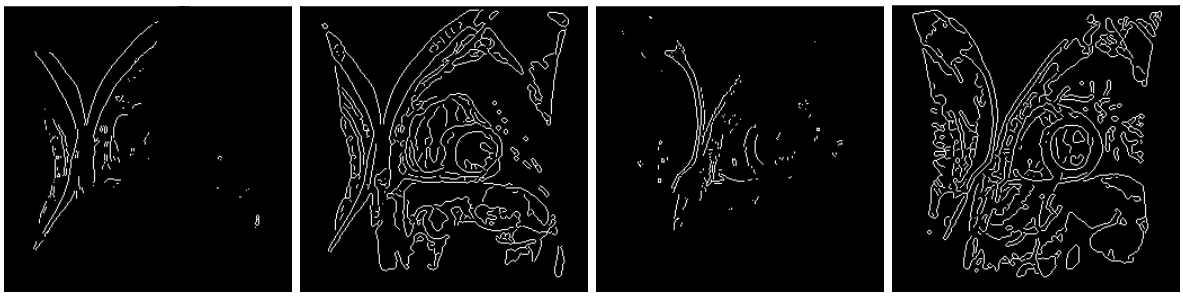

(a) (b) (c) (d)

Figure 5.1: (a,c) Segmentation of CMR images by Prewitt edge operator. (b,d) Segmentation of CMR images by Canny edge operator.

Sobel operator is less effective as compared to Prewitt in presence of high noise level [54], it has been deliberately avoided from consideration. The performances of Prewitt and Canny operator are given in Figure 5.1. Edge detection of LV by Prewitt method is viewed to be very poor (shown in Figure 5.1(a) and 5.1(c)). At the same time, though Canny operator produces a better edge detection, unfortunately, the detection is little useful from medical diagnosis perspective. If Figure 5.1(b) is considered, it may be noticed that the papillary muscle are not included. On the other hand, though Figure 5.1(d) provides a much better performance, a meaningful segmentation is not obtained, instead it yields many unwanted edges within the LV. The shapes of the LV boundary of these two CMR images can be actualized from the corresponding ground truths as shown in Figure 5.2(a) and 5.2(b), respectively. In this context, Random Walk approach is a suitable one that results a meaningful LV segmentation. Broadly, the evaluation criteria are divided in two categories, viz., 1) Supervised and 2) Unsupervised.

A global dissimilarity measure between the ground truth and segmentation result is generally computed by supervised criteria. Two components are needed in order to make this criteria function. The first one is a ground truth corresponding to the best and expected segmentation result. Usually, the ground truth is known in case of synthetic images. In other cases (natural images), an expert manually defines this ground truth [121]. Even if these images are more realistic, one problem concerns regarding the objectivity and variability of experts. The second component is the definition of a dissimilarity measure that depends on the correct classification rate of detected objects in the image [122]. This type of approach is based on local processing and is dedicated to a certain application. On the other hand, unsupervised evaluation criteria enable the quantification quality of a segmentation result without any knowledge a *priori* [123]. The computation of statistical measures on the segmentation result, such as gray level standard deviation or the

contrast of each region in the segmentation play an important role in this evaluation criteria.

These criteria can be used for various applications. Firstly, different segmentation results of a single image can be compared. The behavior of different segmentation methods could be compared in order to choose the most appropriate for a given application. Secondly, the choice of parameters of a segmentation method can be facilitated. Another application is the possibility of defining new segmentation methods by optimizing evaluation criteria. Lastly, with the use of an evaluation criterion, several segmentation results of a single image or of the different bands in the multi- component case can be fused.

There are many supervised segmentation evaluation methods, but for the completeness of this thesis, we restrict ourselves to a few of them.

5.1 Supervised Evaluation Criteria

The main principle of this approach is to measure the dissimilarity between a segmentation result and a ground truth. In case of synthetic images, the ground truths are of course, very reliable and have an extreme precision. For real-time applications, the expert ground truth is subjective and the confidence attached to this reference segmentation has to be known.

5.1.1 Pratt's Figure of Merit

Pratt's Figure of Merit is used to compare the result of an edge detection algorithm to the known ground truth [124], [125]. It returns a number between 0 and 1 based upon the quality of the edge detection, with 1 being the best. The measure is based upon three things, detection, localization and spurious response. This means that the score is based upon all edges being found, all edges being placed in the correct location and no false alarms. This criterion corresponds to an empirical distance between the ground truth contours I_t and that obtained with the chosen segmentation result I_s.

In order to compare two contours using the distances between them, the following steps are necessary:

- Find pairs of equivalent points (one from each contour);
- Determine distances between these points;

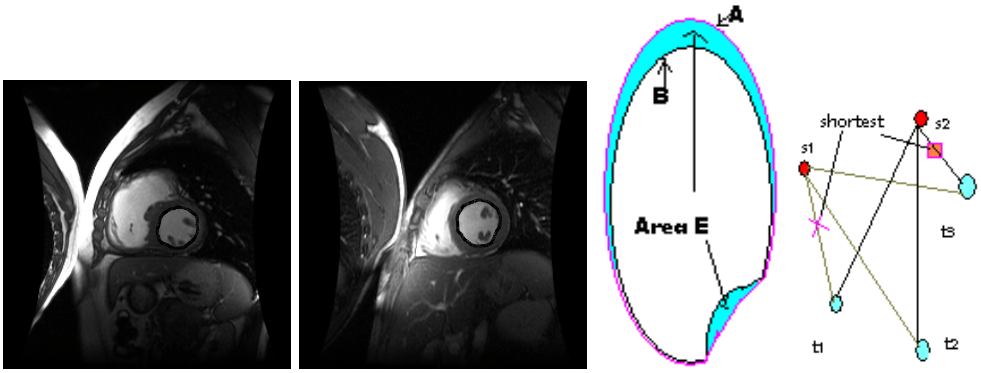

(a) (b) (c) (d)

Figure 5.2: (a,b) Ground truth images of Figure 5.1(a) and 5.1(c), respectively. Figures explaining (c) FOM and (d) Hausdorff's Distance.

- Finally, compute a global figure which characterizes the similarity of the contours.

Let A and B (shown in Figure 5.2(c)) be two similar closed lines corresponding to the contour of an object: contour A = set of n points, contour B = set of m points. Let areas C, D and E be defined as: C = area enclosed by contour A, D = area enclosed by contour B and E = C XOR D.

F is defined as a closed line existing inside area E in zones where contour A is not equal to B. Lines perpendicular to contour F are obtained for each point of this contour. The interception of each of these lines with contours A and B defines a pair of corresponding points on both contours. This completes step 1. Step 2 corresponds to the computation of Euclidean distances between all the corresponding points. Finally (as step 3), the similarity between contours A and B is assessed.

The Pratt's figure of merit is defined as:

$$FOM\left(I_t, I_s\right) = \frac{1}{Max\left\{card\left(I_t\right), card\left(I_s\right)\right\}} \sum_{i=1}^{card(I_s)} \frac{1}{1 + d^2\left(i\right)} \tag{5.1.1}$$

where $d\left(i\right)$ is the distance between the i^{th} pixel of I_s and the nearest pixel of I_t; $card$ represents cardinality. Greater the value of FOM, more the determined contour (curve B) tends towards the ground truth equivalent (curve A). This measure is one of the most used descriptors.

5.1.2 Hausdorff's Distance

Distance between features is a difficult concept which has been approximated through various indicators. Even if these measures are well adapted to the applications they are meant for (mainly

proximity and accuracy evaluations), they all lack at least one of the three prerequisites for being a true mathematical distance : that of separateness, which means that the distance between two objects is zero if and only if those objects are strictly identical. The Hausdorff distance [126] between two objects is a mathematically true distance. When both objects are punctual, it does not differ from the Euclidean distance between points; otherwise it takes into account the mutual positions of the objects relatively to each other. Its main interest for automated cartography, besides quantifying spatial relations between objects, lies in the fact that it expresses remoteness.

Suppose there are two sets of points, s and t, as shown in Figure 5.2(d). The individual distances of each point in each set are calculated. The shortest distances are determined as indicated by $cross$ and $square$ mark. The shortest among these two are finally decided, which shows the shortest distance between these two sets of points.

While applying this measure on image, this criterion measures the distance between two pixel sets: I_s=$s_1, ...s_n$ and I_t=$t_1, ...t_m$:

$$H\left(I_t, I_s\right) = Max\left(h\left(I_t, I_s\right), h\left(I_s, I_t\right)\right) \tag{5.1.2}$$

where

$$h\left(I_t, I_s\right) = Max_{t_i \in I_t} Min_{s_i \in I_s} \left\| t_i - s_i \right\| \tag{5.1.3}$$

If $H\left(I_t, I_s\right) = d$, this means that all the pixels belonging to I_t are not further than d from some pixels of I_s. This measure gives a good similarity measure between two images. Lesser the value of H, more is the accuracy of the determined border with the ground truth.

5.2 Unsupervised Evaluation Criteria

Most of these criteria compute statistics on each region in the segmentation result. The majority of these quality measurements are established in agreement with the human perception. For region segmentation, various criteria take into account the intra-region uniformity and inter-regions contrast.

5.2.1 Intra-Region Uniformity Criteria

Weszka and Rosenfeld [127] have proposed a threshold evaluation method that uses a busyness measure as the criterion to judge thresholded images. To apply the busyness measure they

assume that the images are composed of objects and background of compact shapes and not strongly textured. Under these assumptions, the thresholded images should look smooth rather than busy. In practice, they compute the amount of busyness for a thresholded image by using the grey-level co-occurrence matrix of the image. That is, those entries of the co-occurrence matrix representing the percentage of object-background adjacencies are summarized. The lower the busyness, the smoother the thresholded images and the better the segmentation result. In consequence, the better the segmentation results, the higher the performance of applied algorithm.

Similar to Weszka and Rosenfeld, Nazif and Levine (1984) also have defined a criterion that calculates the uniformity of a characteristic on a region based on the variance of this characteristic [128]:

$$U = 1 - \sum_{k=1}^{N_R} \sum_{s \in R_k} \left[I(s) - \frac{1}{A_k} \sum_{s \in R_k} I(s) \right]^2 = 1 - \sum_{k=1}^{N_R} \sigma_k^2 \tag{5.2.1}$$

where N_R, $I(s)$, and σ_k^2 indicate the number of regions, the gray level of the pixel s, and grey level variance of the region R_k and A_k, respectively. Based on the same principle, Cocquerez et al. have given another measurement of homogeneity of region:

$$\varpi = \frac{\text{Max}\,(k\sigma_k^2)}{\sum\limits_k \sigma_k^2} \tag{5.2.2}$$

where σ_k^2 is the grey level variance of the region R_k. The region R is homogeneous if $\varpi < T$, T is an arbitrary threshold. Greater the value of the intra region index, more is the homogeneity of the particular object in the image.

5.2.2 Inter-Regions Contrast

Except for intra-region uniformity, Levine and Nazif also believe that an adequate segmentation should in addition produce images having higher contrast across adjacent regions. Therefore, again they defined a grey level contrast measurement between two regions to evaluate the dissimilarity of the regions in a segmentation result. The formula of the total contrast is defined as follows [129]:

$$C = \frac{\sum\limits_{i=1}^{N_R} w_i \sum\limits_{j=1}^{N_R} \frac{l_{ij}}{l_i} \frac{|m_i - m_j|}{m_i + m_j}}{\sum\limits_{i=1}^{N_R} w_i} \tag{5.2.3}$$

where N_R, w_i, m_i, l_i, and l_{ij} indicate the number of regions, weight associated with each region that can be its surface, the average gray level of the region R_i, the length of the perimeter of the region R_i, and the length of the border between the regions between R_i and R_j, respectively.

In this work since we are interested in LV (i.e. only one region), the index for inter-regions' contrast is of little use. Therefore, only measure for Intra-Region Uniformity Criteria has been taken in account. The results of measures like Figure of Merit, Hausdorff's Distance and Intra-Region Uniformity on a set of CMR segmented images are summarized in three tables. Table 5.1, 5.2 and 5.3 compare the performance of Gaussian with DoG, DoLoG and LoDroG, respectively. The comparisons of the performance with the use of Gaussian and other described weighting functions are given individually in order to perceive a clear difference. Now, the knowledge of its (this improved algorithm) standing among other popular methods needs to be furnished. For this, we have implemented some standard methods on our experimental data set since a common data set is not present in all methods. Brief description of some common evaluation measures [130] and their values are provided in Table 5.4 and 5.5, respectively; Random Walk seems to have resulted promising figures.

Validation is typically performed using one of the two methods described above. The most straightforward approach to validation is by comparing the automated segmentations with manually obtained segmentations. This approach, besides suffering from the drawbacks outlined in the previous section, does not guarantee a perfect model since an operators performance can also be flawed. Therefore, unsupervised method can be thought as more consistent. The following section introduces a method that compares the performance of two different schemes for segmentation. Instead of taking the help of a ground truth data-base, which are usually used for measuring the degree of execution, we only compare the resulted contours of two methods. In this methodology, the user only needs to draw a rectangle outside the LV that tightly touches the myocardium/epicardium. The task of user is supposed to be not that difficult, as the myocardial muscle is quite visible.

5.3 Maximum of Minimum Distances (MMD) Method

For the sake of conveying the idea behind the method, we take only two weighting functions and suggest the same to be applied for the remaining ones. This method basically compares the performance of Random Walk approach with two different weighting functions e.g., Gaussian

Table 5.1: Evaluation of segmentation by Random Walk approach using Gaussian and DoG as the weighting function.

# Subject	Method	I_h	FOM	H_d	# Subject	Method	I_h	FOM	H_d
1	*Gaussian*	3.81	0.68	5.98	17	*Gaussian*	4.60	0.77	6.32
	DoG	3.51	0.79	5.24		*DoG*	4.10	0.84	5.70
2	*Gaussian*	5.56	0.68	6.35	18	*Gaussian*	4.61	0.76	6.32
	DoG	5.25	0.80	5.67		*DoG*	4.11	0.83	5.68
3	*Gaussian*	5.36	0.69	6.30	19	*Gaussian*	4.69	0.76	6.22
	DoG	4.95	0.81	5.62		*DoG*	4.19	0.83	5.71
4	*Gaussian*	5.62	0.70	6.29	20	*Gaussian*	4.59	0.76	6.37
	DoG	5.31	0.82	5.61		*DoG*	4.14	0.82	5.79
5	*Gaussian*	5.44	0.67	6.35	21	*Gaussian*	4.61	0.78	6.22
	DoG	5.13	0.80	5.79		*DoG*	4.09	0.83	5.73
6	*Gaussian*	5.56	0.68	6.47	22	*Gaussian*	4.69	0.76	6.38
	DoG	5.12	0.81	5.52		*DoG*	4.11	0.87	5.68
7	*Gaussian*	5.24	0.68	6.28	23	*Gaussian*	4.81	0.75	6.42
	DoG	5.21	0.81	5.65		*DoG*	4.29	0.86	5.72
8	*Gaussian*	5.67	0.67	6.46	24	*Gaussian*	4.54	0.78	6.27
	DoG	5.34	0.81	5.78		*DoG*	4.12	0.84	5.65
9	*Gaussian*	5.49	0.66	6.28	25	*Gaussian*	4.61	0.77	6.34
	DoG	5.18	0.81	5.60		*DoG*	4.11	0.84	5.72
10	*Gaussian*	5.55	0.68	6.31	26	*Gaussian*	4.59	0.71	6.31
	DoG	5.25	0.80	5.63		*DoG*	4.09	0.82	5.69
11	*Gaussian*	4.03	0.67	6.07	27	*Gaussian*	4.08	0.66	6.10
	DoG	3.56	0.82	5.31		*DoG*	3.59	0.81	5.33
12	*Gaussian*	5.36	0.69	6.15	28	*Gaussian*	4.65	0.76	6.36
	DoG	5.05	0.81	5.47		*DoG*	4.01	0.82	5.75
13	*Gaussian*	5.54	0.64	6.28	29	*Gaussian*	4.48	0.79	6.15
	DoG	5.23	0.81	5.61		*DoG*	4.00	0.85	5.55
14	*Gaussian*	4.34	0.64	6.25	30	*Gaussian*	4.52	0.61	6.55
	DoG	4.09	0.86	5.13		*DoG*	4.09	0.86	5.13
15	*Gaussian*	5.43	0.67	6.32	31	*Gaussian*	4.54	0.73	6.52
	DoG	5.12	0.80	5.64		*DoG*	4.13	0.82	5.74
16	*Gaussian*	5.20	0.69	6.21	32	*Gaussian*	4.04	0.78	6.19
	DoG	5.01	0.81	5.53		*DoG*	4.01	0.86	5.67

and DoG. The method is described as follows:

- Plot a rectangle that encircles LV and touches the endocardium as shown in Figure 5.3.
- Consider the closed contour $\mathtt{C}$ of LV consisting of $\mathtt{n}$ small curves [131] i.e., $\mathtt{C}=\mathtt{C}_1+\mathtt{C}_2+\mathtt{C}_3+\ldots+\mathtt{C}_{\mathtt{n}-1}$. These small curves are assumed to be smooth. To represent a small curve $\mathtt{C}_1$, we use a parametric notation as follows,

$$\mathtt{C}_1 : \mathtt{z}\,(t) = x\,(t) + y\,(t)\,,\ a \leq t \leq b, \tag{5.3.1}$$

Table 5.2: Evaluation of segmentation by Random Walk approach using Gaussian and DoLoG as the weighting function.

# Subject	Method	I_h	FOM	H_d	# Subject	Method	I_h	FOM	H_d
1	*Gaussian*	3.81	0.68	5.98	17	*Gaussian*	4.60	0.77	6.32
	DoLoG	3.47	0.81	5.18		*DoLoG*	4.05	0.87	5.64
2	*Gaussian*	5.56	0.68	6.35	18	*Gaussian*	4.61	0.76	6.32
	DoLoG	5.20	0.83	5.62		*DoLoG*	3.95	0.87	5.24
3	*Gaussian*	5.36	0.69	6.30	19	*Gaussian*	4.69	0.76	6.22
	DoLoG	4.84	0.86	5.41		*DoLoG*	4.10	0.85	5.59
4	*Gaussian*	5.62	0.70	6.29	20	*Gaussian*	4.59	0.76	6.37
	DoLoG	5.19	0.88	5.61		*DoLoG*	4.04	0.86	5.56
5	*Gaussian*	5.44	0.67	6.35	21	*Gaussian*	4.61	0.78	6.22
	DoLoG	4.91	0.87	5.63		*DoLoG*	3.96	0.89	5.43
6	*Gaussian*	5.56	0.68	6.47	22	*Gaussian*	4.69	0.76	6.38
	DoLoG	5.01	0.84	5.40		*DoLoG*	4.08	0.90	5.60
7	*Gaussian*	5.24	0.68	6.28	23	*Gaussian*	4.81	0.75	6.42
	DoLoG	5.18	0.83	5.62		*DoLoG*	4.27	0.87	5.69
8	*Gaussian*	5.67	0.67	6.46	24	*Gaussian*	4.54	0.78	6.27
	DoLoG	5.28	0.83	5.71		*DoLoG*	4.07	0.88	5.45
9	*Gaussian*	5.49	0.66	6.28	25	*Gaussian*	4.61	0.77	6.34
	DoLoG	5.12	0.84	5.51		*DoLoG*	4.02	0.87	5.66
10	*Gaussian*	5.55	0.68	6.31	26	*Gaussian*	4.59	0.71	6.31
	DoLoG	5.14	0.83	5.51		*DoLoG*	3.96	0.84	5.56
11	*Gaussian*	4.03	0.67	6.07	27	*Gaussian*	4.08	0.66	6.10
	DoLoG	3.52	0.85	5.25		*DoLoG*	3.52	0.84	5.19
12	*Gaussian*	5.36	0.69	6.15	28	*Gaussian*	4.65	0.76	6.36
	DoLoG	5.00	0.85	5.38		*DoLoG*	3.78	0.86	5.33
13	*Gaussian*	5.54	0.64	6.28	29	*Gaussian*	4.48	0.79	6.15
	DoLoG	5.13	0.83	5.48		*DoLoG*	3.89	0.87	5.34
14	*Gaussian*	4.34	0.64	6.25	30	*Gaussian*	4.52	0.61	6.55
	DoLoG	4.02	0.89	5.09		*DoLoG*	3.93	0.88	5.01
15	*Gaussian*	5.43	0.67	6.32	31	*Gaussian*	4.54	0.73	6.52
	DoLoG	5.05	0.83	5.54		*DoLoG*	3.99	0.84	5.65
16	*Gaussian*	5.20	0.69	6.21	32	*Gaussian*	4.04	0.78	6.19
	DoLoG	4.87	0.84	5.37		*DoLoG*	3.88	0.87	5.52

where $x(t)$ and $y(t)$ are continuous functions and $\mathtt{z}$ contained in $\mathtt{C}$ is a complex variable, $\mathtt{z} \in \mathtt{C}$. The complex valued $\mathtt{z}(t)$ is differentiable as $x(t)$ and $y(t)$ are differentiable for $a \leq t \leq b$. The angle of inclination $\theta(t)$ of the tangent vector $\mathtt{z}'(t) = \frac{y'(t_0)}{x'(t_0)}$ for all values of t is given by

$$\theta(t) = \arg[\mathtt{z}'(t)] = \arg[x'(t) + y'(t)]. \tag{5.3.2}$$

Therefore, a smooth curve has a continuously turning tangent vector. The arc length in

Table 5.3: Evaluation of segmentation by Random Walk approach using Gaussian and LoDroG as the weighting function.

# Subject	Method	I_h	FOM	H_d	# Subject	Method	I_h	FOM	H_d
1	*Gaussian*	3.81	0.68	5.98	17	*Gaussian*	4.60	0.77	6.32
	LoDroG	3.42	0.87	5.11		*LoDroG*	4.00	0.91	5.53
2	*Gaussian*	5.56	0.68	6.35	18	*Gaussian*	4.61	0.76	6.32
	LoDroG	5.14	0.89	5.53		*LoDroG*	3.87	0.92	5.19
3	*Gaussian*	5.36	0.69	6.30	19	*Gaussian*	4.69	0.76	6.22
	LoDroG	4.43	0.89	5.11		*LoDroG*	3.88	0.91	5.39
4	*Gaussian*	5.62	0.70	6.29	20	*Gaussian*	4.59	0.76	6.37
	LoDroG	4.89	0.89	5.44		*LoDroG*	3.84	0.93	5.22
5	*Gaussian*	5.44	0.67	6.35	21	*Gaussian*	4.61	0.78	6.22
	LoDroG	4.71	0.89	5.34		*LoDroG*	3.91	0.90	5.33
6	*Gaussian*	5.56	0.68	6.47	22	*Gaussian*	4.69	0.76	6.38
	LoDroG	4.80	0.87	5.13		*LoDroG*	4.01	0.95	5.51
7	*Gaussian*	5.24	0.68	6.28	23	*Gaussian*	4.81	0.75	6.42
	LoDroG	5.12	0.87	5.52		*LoDroG*	4.11	0.90	5.18
8	*Gaussian*	5.67	0.67	6.46	24	*Gaussian*	4.54	0.78	6.27
	LoDroG	5.02	0.85	5.59		*LoDroG*	4.02	0.89	5.44
9	*Gaussian*	5.49	0.66	6.28	25	*Gaussian*	4.61	0.77	6.34
	LoDroG	4.91	0.88	5.05		*LoDroG*	3.74	0.92	5.43
10	*Gaussian*	5.55	0.68	6.31	26	*Gaussian*	4.59	0.71	6.31
	LoDroG	4.85	0.88	5.23		*LoDroG*	3.66	0.93	5.12
11	*Gaussian*	4.03	0.67	6.07	27	*Gaussian*	4.08	0.66	6.10
	LoDroG	3.46	0.91	5.15		*LoDroG*	3.42	0.94	4.56
12	*Gaussian*	5.36	0.69	6.15	28	*Gaussian*	4.65	0.76	6.36
	LoDroG	4.77	0.88	5.18		*LoDroG*	3.58	0.94	4.92
13	*Gaussian*	5.54	0.64	6.28	29	*Gaussian*	4.48	0.79	6.15
	LoDroG	4.93	0.87	5.32		*LoDroG*	3.74	0.91	5.12
14	*Gaussian*	4.34	0.64	6.25	30	*Gaussian*	4.52	0.61	6.55
	LoDroG	3.95	0.94	5.01		*LoDroG*	3.81	0.89	4.78
15	*Gaussian*	5.43	0.67	6.32	31	*Gaussian*	4.54	0.73	6.52
	LoDroG	4.67	0.88	5.26		*LoDroG*	3.87	0.90	5.24
16	*Gaussian*	5.20	0.69	6.21	32	*Gaussian*	4.04	0.78	6.19
	LoDroG	4.63	0.89	5.11		*LoDroG*	3.76	0.91	5.24

$[a, b]$ is

$$\mathsf{L} = \int_a^b \sqrt{[x'(t)]^2 + [y'(t)]^2}\, dt = \int_a^b |\mathrm{z}'(t)|\, dt. \tag{5.3.3}$$

- Green's Theorem [131] states that if R is a plane region with boundary curve C directed

Table 5.4: The employed metrics for quantitative evaluation.

Measures	Definition
Hausdorff distance (H_d)	Minimum distance between two sets of points
intra-region (I_h)	Index of homogeneity
Figure of Merit (FOM)	Segmentation index of matching with ground truth equivalent
Precision	True positive/(True positive + false positive)
Accuracy	(True positive + true negative)/total samples
Mean error rate (MER)	(False positive + false negative)/total samples $\times$ 100

Table 5.5: Quantitative segmentation comparison among a few selected methods.

Serial No.	Method	I_h	FOM	H_d	Precision	Accuracy	MER
1	NCut	4.19	0.78	5.98	0.8647	0.8641	0.9881
2	Kmeans clustering	3.76	0.76	6.09	0.8520	0.8531	0.9889
3	GrowCut	3.96	0.86	5.41	0.9357	0.9334	0.8432
4	GrabCut	3.92	0.83	5.62	0.9031	0.9087	0.9231
5	**Our method**	**4.04**	**0.92**	**5.06**	**0.9533**	**0.9788**	**0.7210**

counterclockwise and $\overrightarrow{F} = [M, N]$ is a vector field differentiable throughout R, then

$$\int_C \overrightarrow{F}.\overrightarrow{T}\,ds = \iint_R \left(\frac{\partial N}{\partial x} - \frac{\partial M}{\partial y}\right) dA. \tag{5.3.4}$$

s and $\overrightarrow{T}$ denote an oriented surface with boundary curve C and the unit tangent vector to C, respectively.

A curious consequence of Green's Theorem is that the area of the region R enclosed by a simple closed curve C in the plane can be computed directly from a line integral over the curve itself, without direct reference to the interior. The reason is that if $\overrightarrow{F} = [M, N]$ is

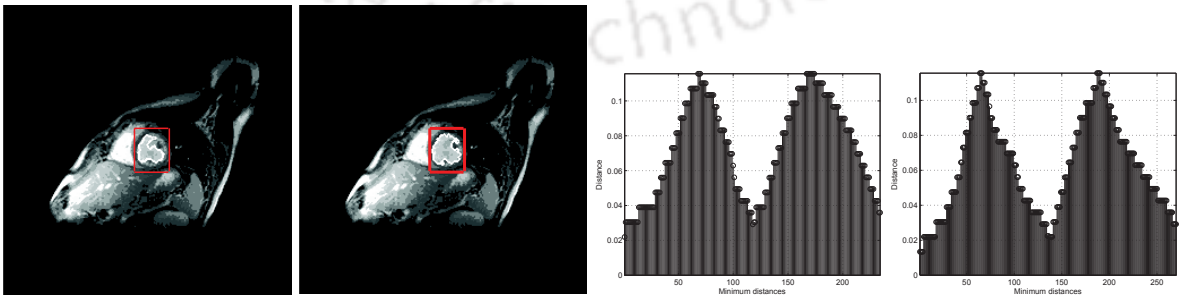

(a) (b) (c) (d)

Figure 5.3: (a-b) Placement of a rectangle surrounding the contour. (c-d) Comparison of segmentation, resulted due to Random Walk with Gaussian and DoG weighting function.

taken and M and N are chosen such that

$$\frac{\partial N}{\partial x} - \frac{\partial M}{\partial y} = 1, \tag{5.3.5}$$

then the area of R,

$$\Lambda = \iint_R d\mathsf{A} = \int_C [M, N] \,.\, \overrightarrow{T}\, d\mathtt{s}. \tag{5.3.6}$$

If Υ is the area of the rectangle, then area remaining between Υ and Λ is $\wp = \Upsilon - \Lambda$. Allocate the edges of the rectangle to each contour pixel depending on the distance from each edge of the rectangle. The edge that gives minimum distance is the corresponding edge for that pixel.

- Get all the distances of each pixel from the corresponding edges of the rectangle. The contour that gives maximum of minimum distances (M_d) is considered as the best contour in the group. In addition, this contour should have less $\wp$ and L as compared with the others in the test group.

The steps described above, should be same for all the contours to be compared.

5.4 Presentation of Results

Only the segmented output obtained using Gaussian is compared with that of DoG. The determined borders due to Gaussian and DoG are given in Figure 5.3(a) and 5.3(b), respectively. Figure 5.3(c) and 5.3(d) show M_d for Gaussian and DoG, respectively. If we compare the results of Random Walk approach using the two weighting functions individually, the performance of DoG (Figure 5.3(d)) is seen to have maximum number of M_d).

The dimension of grey marked rectangular box on LV in each image is same as shown in Figure 5.3(a) and 5.3(b). The tight rectangle is chosen to avoid any inclusion of over-segmented pixel.

Finally for the completeness of the thesis, a discussion on application of segmentation is chipped in. There are several applications in the field of segmentation especially relating to cardiology, viz. ejection fraction, heart wall motion detection, left ventricular mass detection, and measurement of tissue volumes to name a few. Apart from these, let us consider another application where a patient is assumed to be at a remote area. Suppose there comes a need to transfer

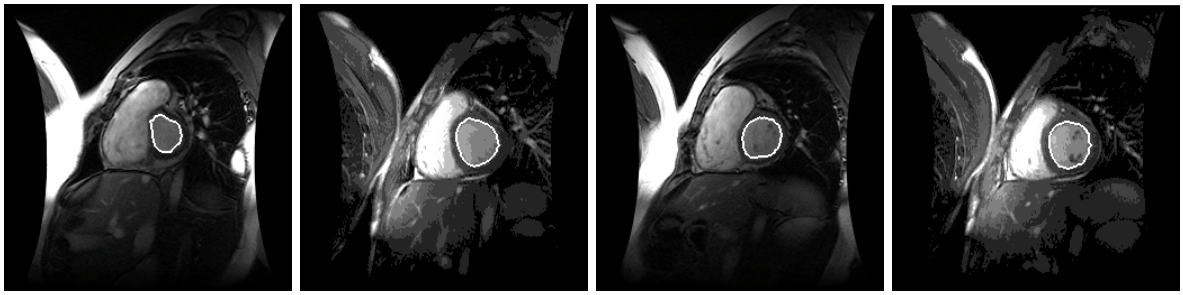

(a) (b) (c) (d)

Figure 5.4: (a-d) Some segmented images of different subjects.

the CMR data of the patient through wireless communication channel to an expert to a distant urban location. In this case, major challenges due to the growing size of 24 hour CMR data-sets as well as practical limitations in transmission bandwidth and storage space arise. One of the solutions could be if LV (blood pool) of the patient is only the concern, then transmission of CMR image where LV is fully protected will drastically reduce the memory requirement. To serve the objective, region based compression [132] carries a substantive importance. Left ventricle region should be compressed by a lossless technique, while the rest of the image by a lossy technique. There are many lossy techniques [133], [134] to date which provide a good compression ratio (approximately 50:1 or more). On the other hand, lossless techniques [135], [136], [137] result a low compression ratio (of 2:1 or 4:1). On employing a region based technique, a good compression may be obtained at the end that retains all the information in LV.

Original CMR images (with blood pool segmentation) are shown in Figure 5.4. The performance obtained from a lossy algorithm and the combination of the region based (lossy and lossless) are shown in Figure 5.5 and 5.6, respectively.

5.5 Conclusions

There are many evaluation techniques, methods and frameworks on image segmentation. Still, the search for a best method is on with the emergence of medical image varieties. In this chapter, the performance of different proposed weighting functions has been evaluated by three existing techniques. Most of the methods for evaluating the effectiveness of a segmentation method use subjective evaluation, in which a human visually compares the image segmentation results for separate segmentation algorithms. This is a tedious process and inherently limits the

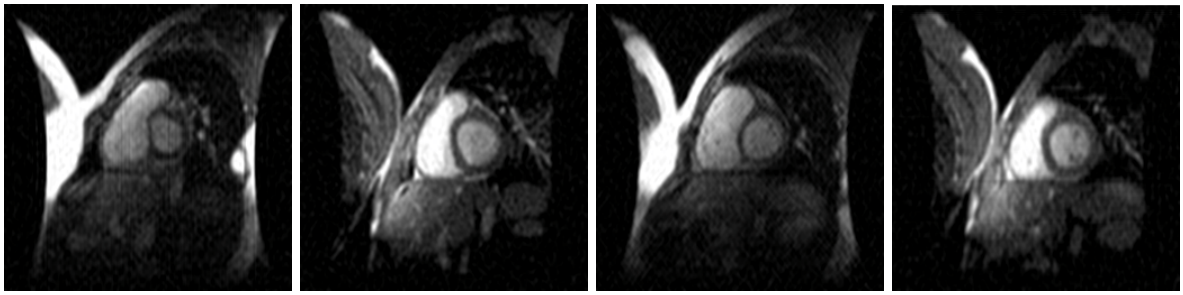

(a) (b) (c) (d)

Figure 5.5: (a-d) Corresponding lossy segmented slices in shown Figure 5.4.

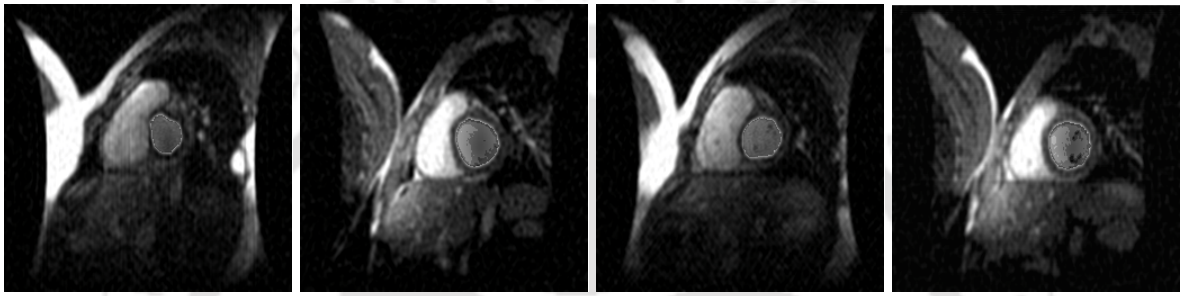

(a) (b) (c) (d)

Figure 5.6: (a-d) Corresponding region based compressed segmented slices shown in Figure 5.4.

depth of evaluation to a relatively small number of segmentation comparisons over a predetermined set of images. Considering the infeasibility of present methods in many vision applications, an unsupervised comparison technique has been proposed. The method is simple and seems to be satisfactory [138], since it requires very little user intervention.

This thesis has discussed basically the Random Walk based CMR image segmentation. There have arisen many problems and attempts have been made to solve them. In the next chapter, a summary of this work is presented.

Chapter 6

Summary and Scope for Future Work

Segmentation issues in medical images has become an active area of research in the image processing community. In the context of CMR images, segmentation of an object in the image that owes an increased importance and interest in the recent years is the left ventricle. The present research work proposes a method which 1) is automatic to a large extent; 2) can effectively segment both left ventricle endocardium and epicardium. After a thorough literature survey, we have selected Random Walk and active contour model as the suitable tools for this work. The present thesis has investigated Random Walk on image segmentation and presented some methods based on the findings. Finally, the quality of segmentation was validated by radiology technicians to ensure the reliability of the results. The main contributions of the thesis are summarized in Section 6.1 and a few tracks for future research are outlined in Section 6.2.

6.1 Summary

In this work, we have dealt with ischemic CMR images, where the objects in the image are obscure and nonhomogeneous. The first problem that has been addressed by the thesis in Chapter 2 is how to employ Random Walk in ischemic CMR images for segmenting blood pool region. Random Walk based image segmentation algorithm is a general purpose interactive segmentation method that uses "graph cuts" interface. This method works as follows:

- A user interactively labels a small number of pixels with known labels (called seeds), e.g., "object" and "background" in the image.
- The unlabeled pixels are each imagined to release a random walker.

- After the first arrival, the probability that the random walker starting at a pixel first reaches one of the seeds is computed; the pixel takes the label that gives maximum probability.
- The maximum probable pixels constitute the desired object boundary.

Intensity inhomogeneity is often seen in the left ventricle and this causes considerable difficulties in applying this segmentation algorithm on such CMR images. The left ventricle is therefore is considered as a multi-labeled object. There are mainly three challenges in the due course of its boundary extraction, 1) selection of seeds, 2) seeds' placement, and 3) determination of β (used in weighting function). The corresponding solutions proposed in this thesis are as follows:

1. Since the pixel intensity values in a CMR image are low in terms of magnitude, it is therefore difficult to exactly distinguish two separate labels with minor demarcation. A method using heat equation in association with an adaptive threshold technique has been proposed to select the seeds in each sub-label. This method leaves a possibility that a sub-label contains more than one seed, which in turn increases unnecessary computational complexity. Therefore, a discarding scheme is implemented such that each sub-label contains exactly one seed point.

2. Usually, one seed is sufficient to precisely segment a homogeneous object. On the other hand, to segment the multi-labeled left ventricle, superposition concept has been applied that draws a single boundary for the left ventricle. Otherwise, unnecessary multiple object boundaries are bound to be extracted.

3. Weighting function maps the intensity values to edge weights. It decides whether two adjacent pixels belong to the same object or not. A parameter β is used in this function which is normally determined by the operator. It is well known that user intervention often brings variability in the performance. Therefore, instead of specifying the value of β manually, a method has been suggested that ascertains the same from the input image.

Overall, the results are found to be satisfactory and clearly reflects the efficiency of the described approach. Application of this method, mostly to short axis CMR images, faces difficulty to potentially segment the blood pool region. This is because the sufficient background region must be needed to get a proper β and unfortunately it is not the case in short axis CMR images.

The above problem is tackled in Chapter 4, where some weighting functions have been suggested to be used in Random Walk based image segmentation. Difference of Gaussian (DoG),

difference of Laplacian of Gaussian (DoLoG) and Laplacian of Derivative of Gaussian (LoDroG) weighting function are demonstrated to be effective in such images. The performances of these functions, when used in Random Walk approach, prove to be more effectual as compared to Gaussian weighting function. Among these functions, LoDroG is found to be the best. The idea behind the modification of weighting function is to make the Random Walk perform accurately to segment short axis as well as long axis CMR images. Straightway Random Walk can not be used to segment the epicardium because there is very little pixel intensity difference between myocardium and surrounding muscle. Huge merits of active contour model in presence of noise has encouraged us to utilize its characteristics for the said objective. The model has been modified that takes blood pool boundary as its initial contour to extract the epicardial wall. In this way, the basic requirement to initialize the variable curve near the object boundary is avoided. The result of this approach, to some extent, depends on the shape of the blood pool contour, which is shown in Chapter 3.

Finally, Chapter 5 investigates some existing segmentation evaluation techniques and proposes a new method, Maximum of Minimum Distances (MMD), which is unsupervised in nature. Instead of taking the help of a ground truth database, which is usually employed for measuring the degree of performance, we have simply compared the resulting contours obtained from two methods. In this methodology, the user only requires to draw a rectangle outside the LV that tightly touches the epicardium. The method seems to be upright in terms of its simplicity. In the end, region based compression is given as an application of segmentation in this chapter for completeness of the thesis.

6.2 Tracks for Future Work

This Section outlines a few tracks for feature research direction.

- **Parameter selection:** It is well known that increasing the level of automation in image segmentation process could save significant time and effort. Thereby, it could enhance the precision by eliminating human subjectivity. In this context, the value of σ (used in various weighting functions in Chapter 4) may be considered to obtain from the image.

- **Epicardial contour:** The shape of epicardial wall is found to be endocardial contour dependent (as described in Chapter 3), to some extent, irrespective of the myocardium inten-

sity distribution. Suppose a need arises to segment an image having varying myocardium thickness, a proper epicardial wall may not be expected using this method in this case. A new method may be imagined of to avoid such crisis.

- **Feature detection and motion estimation:** Once the CMR image is segmented, the next two crucial steps (from clinical view point) are feature detection and motion estimation. The distinction we make between segmentation and feature detection is that feature detection is concerned with determining the presence of some image property. On the other hand, segmentation generally assumes that the property is already present and it attempts to precisely localize areas that possess the property. For example, edge detection methods can determine the location of edges in an image but without further processing, it does not necessarily extract any region of interest. Motion estimation methods often consist of applying segmentation algorithms to time sequences of images. The motion analysis of heart after segmentation is an important aspect which could be considered for future research direction because it is a major visual support for any clinician to get into the reasons behind any disease.

- **Cardiac cine MRI:** For measurement of global cardiac function, bright blood cine MRI is performed in multiple short-axis views with a multi-phase, segmented k-space and GRE sequence. However, saturation in areas of low blood velocity reduces the contrast between the ventricular cavity and the myocardium on GRE images [139]. The saturation effect hampers endocardial contour detection with automatic or semi-automatic segmentation algorithms. The segmentation of LV in cine CMR images faces challenges, some of them are: 1) the overlap between intensity distributions within the cardiac regions; 2) the lack of edge information and 3) the shape variability of endocardial and epicardial region. Since Random Walk has been proved to be effective on 2D CMR images, therefore, such type of images could be tried using this approach.

- **Classification and compression:** Heart disease is any disorder that affects the heart's ability to function normally. Various forms of heart disease include: 1) aortic regurgitation; 2) aortic stenosis; 3) arrhythmias; 4) cardiogenic shock; 5) congenital heart disease and so on. Therefore, the classification of pixels in a CMR image corresponding to the tissues in heart is required. Since the characteristics of segmentation is to group identical pixels.

This property can well be utilized in image compression.

- **Other medical images:** Several medical imaging modalities are used only to a limited extent in radiological practice or are still at the experimental stage. Positron emission tomography (PET) and single photon emission computed tomography (SPECT) belong to the former group. Magnetic resonance spectroscopy, electrical source imaging, electrical impedance tomography, magnetic source imaging and medical optical imaging belong to the latter group [140]. MRI has some distinct points with respect to noise, intensity, etc. as compared to other medical imaging modalities. Performance of the algorithm described in this thesis, may be compared by implementing it on other imaging modalities. For example, the major disadvantages of medical ultrasound imaging are the relative poor spatial image resolution due to blurring, speckle and noise in most applications. Also, the fact that ultrasound does not pass bone so several soft tissues can not be imaged routinely. Air in the lungs and thick fat layers also represent major problems for ultrasound imaging.

Chapter 7

APPENDIX

7.1 Relationship Between the Image Variance and Distribution Function

In this section, the direct relation relationship between the image variance and the candidate variable is described. If ξ be a random variable that is uniformly distributed, that means

$$\xi \cong \text{Uniform}(0,1)$$

and F is an arbitrary distribution function (df), then the random variable K satisfies

$$K = \int_{(-\infty,\infty)} k d1_{[K\leq k]} \tag{7.1.1}$$

where $1_{[K\leq k]}$ is a random df that puts mass 1 at the point k. If K has mean μ, then

$$\mu = \int_{(-\infty,\infty)} k dF(k) \tag{7.1.2}$$

It can further be written as

$$K - \mu = \int_{(-\infty,\infty)} k d\left(1_{[K\leq k]} - F(k)\right) \tag{7.1.3}$$

then by parts, it can be

$$K - \mu = -\int_{(-\infty,\infty)} \left(1_{[K\leq k]} - F(k)\right) dk \tag{7.1.4}$$

For Equation 7.1.4, $k\left[1 - F(k)\right] \leq \int_{(k,\infty)} y dF(y) \to 0$ as $k \to \infty$ if $E|K| < \infty$. Thus when Var $[K] < \infty$, Fubini's theorem gives

$$\text{Var}\,[K] = \int_{-\infty}^{\infty}\int_{-\infty}^{\infty} [F\,(k\Lambda y) - F\,(k)\,F\,(y)]dkdy \tag{7.1.5}$$

via (7.1.4). From Equation 7.1.5 and 2.6.11, it can be conceded that

$$\text{Var}\,[K] \quad \propto \quad F\,(k)$$

and

$$\text{Var}\,[K] \quad \propto \quad k$$

This clearly demonstrates the direct relation between distribution function and the variable.

7.2 Wave Propagation in a Cantilever Beam Subjecting the Impact Moment

Let an elastic beam of constant depth, initially at rest with one side hinged is suddenly subjected to load. The loads are governed by the beam points (intensity values of the pixels). The natural frequencies and mode shapes are used to compute and animate the system response produced by the beam. Similar to heat equation, solution to the differential equation formed in this case is

$$U = U_p + U_h \tag{7.2.1}$$

where $U_h = U_1 \cos(\omega t) + U_2 \sin(\omega t)$ with $U_j = (K - \omega^2 M)^{-1} F_j \quad j = 1, 2;$ K, M and ω represent stiffness matrix, elemental mass and resonant frequency, respectively. Here $K - \omega^2 M$ is assumed to be non-singular. The homogeneous equation satisfies

$$M\,U_h + \ddot{K}Y_h = 0 \tag{7.2.2}$$

with initial conditions $U_h\,(0) = U_0 - U_1$ and $\dot{U}\,(0) = V_0 - \omega U_2$. The homogeneous solution components have the form

$$U_{jh} = P_j \cos(\omega_j t + \phi_j) \tag{7.2.3}$$

where ω_j and P_j are natural frequencies and modal vectors satisfying the eigenvalue equation

$$KP_j = \omega_j^2 M P_j \tag{7.2.4}$$

The homogeneous solution completing the modal response is

$$U_h(t) = \sum_{j=1}^{n} P_j \left[\cos(\omega_j t)\, c_j + \sin(\omega_j t)\, d_j/\omega_j\right] \tag{7.2.5}$$

where c_j and d_j are computed to satisfy the initial conditions which require

$$C = P^{-1}(U_0 - U_1) \quad D = P^{-1}(V_0 - \omega U_2) \tag{7.2.6}$$

7.3 Heat Conduction Through a Slab

Let a slab is kept over a heat source whose left part is hinged, conductance is varying gradually according to $U_0 \sin(\Omega T)$, where Ω, T are frequency and time, respectively. One of the mostly used differential equation formats of heat equation is

$$u_t = c^2 u_{xx} \tag{7.3.1}$$

If the ends of the rod are kept at zero temperature, the formulated problem is said to be having homogeneous boundary conditions else it is known as non-homogeneous. This type of problem includes the initial conditions

$$u(0,t) = u(p,t) = 0 \tag{7.3.2}$$

$$u(x,0) = f(x) \tag{7.3.3}$$

The initial temperature in the slab is zero making the problem:

$$\alpha^2 \frac{\partial^2 U}{\partial X^2}(X,T) = \frac{\partial U}{\partial T}(X,T), \quad 0 < X < l,\ T > 0 \tag{7.3.4}$$

$$\cdot\frac{\partial U}{\partial X}(0,T) = 0,\ U(l,T) = U_0 \sin(\Omega T) \tag{7.3.5}$$

$$U(X,0) = 0, \quad 0 < X < l \tag{7.3.6}$$

where U, X, α, l are temperature, position, thermal diffusivity and length, respectively. The problem can be converted into dimensionless form

$$u = \frac{U}{U_0}, x = \frac{X}{l}, l = \frac{\alpha T}{l^2}, \omega = \frac{\Omega l^2}{\alpha} \tag{7.3.7}$$

Then we get

$$\frac{\partial^2 u}{\partial x^2} = \frac{\partial u}{\partial t}, \qquad 0 < x < 1,\ t > 0 \tag{7.3.8}$$

$$\frac{\partial u(0,t)}{\partial x} = 0, \quad u(1,t) = \Im\left(e^{i\omega t}\right) \tag{7.3.9}$$

$$u(x,0) = 0 \tag{7.3.10}$$

This is nonhomogeneous boundary equation. In order to introduce the homogeneous boundary conditions to the problem it is assumed that as $t \to \infty$, the temperature in the rod does not depend on t. In other words,

$$\underset{t\to\infty}{Lt} \quad u(x,t) = R(x) \tag{7.3.11}$$

where $R(x)$ is the steady state temperature. Now, the original heat equation becomes

$$u(x,t) = v(x,t) + R(x) \tag{7.3.12}$$

where $v(x,t)$ is the transient temperature. Substituting $u(x,t)$ in the general heat equation and using the boundary conditions we get

$$v(p,t) + R(p) = T_1 \tag{7.3.13}$$

where p is the length of the rod and $T_1 = \Im(e^{i\omega t})$. Now, there are two sets of problem

$$R'' = 0, \quad 0 < x < p \tag{7.3.14}$$

$$R(0) = T_0, \quad R(0) = T_1 \tag{7.3.15}$$

The other set is

$$v_t = c^2 v_{xx}, \quad 0 < x < p, \ t > 0 \tag{7.3.16}$$

$$v_x(x,0) = 0, \quad v_x(p,t) = 0, \ t > 0 \tag{7.3.17}$$

$$v(x,0) = 0 \tag{7.3.18}$$

Using the method of separation of variables and implementing the boundary conditions, we solve for the homogeneous part as

$$v(x,t) = \sum_{n=1}^{\infty} f(x)\, e^{c^2}\lambda_n t \tag{7.3.19}$$

$$f(x) = \Im\left[\frac{\cos\phi x}{\cos\phi}\right] \tag{7.3.20}$$

where $\phi = \sqrt{-j\omega}$ and the non-homogeneous part as

$$R(x,t) = \Im\left[\frac{\cos\phi x}{\cos\phi} e^{i\omega t}\right] \tag{7.3.21}$$

The solution of the heat equation thus becomes

$$u(x,t) = v(x,t) + R(x,t) \tag{7.3.22}$$

7.4 Wave propagation in a beam subjecting torque

Consider a beam of uniform cross section which is pin ended and is initially at rest. Suddenly, a harmonically varying moment $M_0 \cos(\Omega_0 T)$ is applied to the right end. Let the terms U, X and T be transverse displacement, longitudinal distance from the right end, and time, respectively. The differential equation, boundary conditions and initial conditions characterizing the problem are as follows:

$$EI\frac{\partial^4 U}{\partial X^4} = -W\rho\frac{\partial^2 U}{\partial T^2} \quad 0 < p < R,\ T > 0 \tag{7.4.1}$$

$$U(0,T) = 0,\ \frac{\partial^2 U}{\partial X^2}(0,T) = 0 \tag{7.4.2}$$

$$U(R,T) = 0,\ \frac{\partial^2 U}{\partial X^2}(R,T) = \frac{M_0}{EI}\cos(\Omega_0 T) \tag{7.4.3}$$

$$U(0,T) = 0,\ \frac{\partial U}{\partial T}(0,T) = 0 \tag{7.4.4}$$

where X is the beam length, EI is the product of elastic modulus and moment of inertia and $W\rho$ is the product of cross section area and mass density. For convenience, one may convert the variables to a standard dimensionless form as

p - position = $\frac{X}{R}$

t - time = $\left[\sqrt{(EI)/(W\rho)}\right] R^{-2}T$

u - displacement = $\left[(EI)/(M_0R^2)\,U\right]$

ω - forcing frequency = $\left[\sqrt{(W\rho)/(EI)}\right] R^2\Omega_0$

m - bending moment = $\frac{\partial^2 u}{\partial s^2}$. So the new boundary value problem is

$$\frac{\partial^4 u}{\partial p^4} = -\frac{\partial^2 u}{\partial t^2} \quad 0 < p < 1,\ t > 0 \tag{7.4.5}$$

$$u(0,t) = 0,\ \frac{\partial^2 u}{\partial p^2}(0,T) = 0 \tag{7.4.6}$$

$$u(1,t) = 0,\ \frac{\partial^2 u}{\partial p^2}(1,t) = 0 \tag{7.4.7}$$

$$u(p,0) = 0,\ \frac{\partial u}{\partial t}(p,0) = 0 \quad 0 < p < 1 \tag{7.4.8}$$

Now, the problem can be solved by combining a particular solution u_1 which satisfies the differential equation and the nonhomogeneous boundary conditions, with a homogeneous solution in series form which satisfies the differential equation and homogeneous boundary conditions. Thus we have $u = u_1 + u_2$. The particular solution is in the form of

$$u = f(p)\cos(\omega t) \tag{7.4.9}$$

where $f(s)$ satisfies $f''''(s) = \omega^2 f(s)$ and $f(0) = f''(0) = f(1)$ and $f''(1) = 1$. This ordinary equation is solvable as

$$f(p) = \sum_{v=1}^{4} c_k e^{l_v p} \tag{7.4.10}$$

where

$l_k = \sqrt{\omega}\, e^{\pi i (v-1)/2} \quad i = \sqrt{-1}$. The boundary conditions require

$$\sum_{v=1}^{4} c_v = 0, \; \sum_{v=1}^{4} c_v l_v^2 = 1 \tag{7.4.11}$$

$$\sum_{v=1}^{4} c_v e^{l_v} = 0, \; \sum_{v=1}^{4} c_v l_v^2 e^{l_v} = 0 \tag{7.4.12}$$

Solving these equations the particular solution can be determined. The particular solution satisfies the initial conditions $u_1(0,t) = f(p) = \sum_{v=-\infty}^{\infty} c_v e^{i\pi v p}$ and $\frac{\partial u_1}{\partial t}(0,t) = 0$, where $f(p)$ is expandable in a complex Fourier series as an odd valued function such that

$$f(p) = f(p+2) = -f(2-p) \quad 0 < p < 1 \tag{7.4.13}$$

This implies that $f(p)$ is represented as a sine series,

$$f(p) = \sum_{v=1}^{\infty} a_v \sin(v\pi p) \tag{7.4.14}$$

with $a_v = -2\,[\text{imag}(c_v)]$. The homogeneous solution is represented as

$$u_2(p,t) = -\sum_{v=1}^{\infty} a_v \cos\left(\pi^2 v^2 t\right) \sin(v\pi p) \tag{7.4.15}$$

so that u_1 and u_2 combine to satisfy the desired initial conditions.

7.5 Derivative of Gaussian (DroG) weighting function

The Gaussian weighting function is defined as

$$w_{Gauss}(x) = \begin{cases} \frac{1}{\sqrt{2\pi\sigma^2}} e^{\left(-\frac{x^2}{2\sigma^2}\right)}, & x \in \text{ROI} \\ 0, & \text{elsewhere,} \end{cases} \tag{7.5.1}$$

where σ is the usual standard deviation. The derivative of the Gaussian function ($Gauss(x)$) is obtained [116] by,

$$\frac{\partial^n}{\partial x^n} Gauss(x) = (-1)^n \frac{1}{\left(\sigma\sqrt{2}\right)^n} H_n\left(\frac{x}{\sigma\sqrt{2}}\right) Gauss(x) \tag{7.5.2}$$

where n is the order of the derivative and $H_n(x)$ is the Hermite polynomial. In our case, we take $n = 1$. Simplifying the above function we get,

$$w_{DroG}(x) = \frac{-x}{2\sqrt{2\pi}\sigma^3} e^{-\frac{x^2}{2\sigma^2}} \tag{7.5.3}$$

Here, we consider the absolute value of the above weighting function. The characteristic function due to Gaussian weighting function is

$$E_v^{Gauss} = \int_0^{2t} v(x)\, w_{Gauss}(x)\, dx. \tag{7.5.4}$$

and for DroG is

$$E_v^{DroG} = \int_0^t \frac{x}{2\sqrt{2\pi}\sigma^3} e^{-\frac{x^2}{2\sigma^2}} e^{-\frac{(x-t)^2}{2\sigma_s^2}} dx + \int_t^t \frac{x}{2\sqrt{2\pi}\sigma^3} e^{-\frac{x^2}{2\sigma^2}} dx \tag{7.5.5}$$

The difference between two characteristic functions is expressed as

$$E_v^{DroG} - E_v^G = \frac{1}{2\sqrt{2\pi}\sigma^3}\left[Exp\left(1 + \frac{t(\ln t - 1) - \left(\frac{1}{2\sigma^2}+\frac{1}{2\sigma_s^2}\right)\frac{t^3}{3} + \frac{t^2}{4\sigma_s^2}}{t^3 Exp\left(-\left(\frac{1}{2\sigma^2}+\frac{1}{2\sigma_s^2}\right)\right)t^2}\right) - 0.25\sigma^2\left(\Gamma\left(2, \frac{2t^2}{\sigma^2}\right) - \Gamma\left(2, \frac{t^2}{2\sigma^2}\right)\right)\right] - \frac{1}{\sqrt{2}\sigma}\left[\frac{0.5}{\left(\frac{1}{2\sigma^2}+\frac{1}{2\sigma_s^2}\right)^{\frac{3}{2}}}\left(\left(\frac{t}{2\sigma_s^2}\right)^2 - \left(\frac{1}{2\sigma_s^2+2\sigma^2}\right)\left(\frac{t^2}{2\sigma_s^2}\right)\right)\left\{erf\left(\sqrt{\frac{1}{2\sigma^2}+\frac{1}{2\sigma_s^2}}t - \frac{\frac{t}{2\sigma_s^2}}{\sqrt{\frac{1}{2\sigma^2}+\frac{1}{2\sigma_s^2}}}\right) - erf\left(\frac{\frac{-t}{2\sigma_s^2}}{\sqrt{\frac{1}{2\sigma^2}+\frac{1}{2\sigma_s^2}}}\right)\right\} + \frac{\sigma}{\sqrt{2}}\left(erf\left(\sqrt{\frac{1}{2\sigma^2}}2t\right) erf\left(\sqrt{\frac{1}{2\sigma^2}}t\right)\right)\right]$$

where erf is the error function and $\Gamma(a, x) = \int_z^\infty e^{-t} t^{a-1} dt$. Usually, for edge detection, the first derivative of the image function convolved with a Gaussian is equivalent to the image function convolved with the first derivative of a Gaussian. Therefore, it is possible to combine the smoothing and detection stages into a single convolution in one dimension, either convolving with the first derivative of the Gaussian and looking for peaks, or with the second derivative and looking for zero crossings. Meanwhile, in context with our objective, DroG is used as a weighting function.

Bibliography

[1] H. Gray, *Anatomy of the Human Body*. Lea & Febiger, 1918.

[2] A. Szeto, "Faces and places [biomedical MRI pioneer]," *Engineering in Medicine and Biology Magazine, IEEE*, vol. 23, no. 2, pp. 8 – 9, 2004.

[3] M. Maria, P. Magda, B. Florin, M. Sorin, T. Adrian, V. Ana, and S. Cristian, "Computed tomography versus magnetic resonance imaging in evaluation of head injuries," *TMJ*, vol. 53, pp. 234–240, 2003.

[4] S. Hussain and R. Semelka, "Liver masses," *Magn. Reson. Imaging Clin. N. Am.*, vol. 13, pp. 255–275, 2005.

[5] B. Bernhard, "NMR imaging of materials," *Measurement Science and Technology*, vol. 14, no. 9, p. 1739, 2003.

[6] J. Hornak, "The basics of MRI," November 2006. [Online]. Available: http://www.cis.rit.edu/htbooks/mri

[7] D. Mitchell and M. Cohen, *MRI Principles*, 2nd ed. Philadelphia, Pennsylvania 19106: Saunders: Elsevier Science, 2004.

[8] A. Macovski, "Noise in MRI," *Magnetic Resonance in Medicine*, vol. 36, no. 3, pp. 494–497, 1996.

[9] T. D. Bernstein, M. and W. Perman, "Improved detectability in low signal-to-noise ratio magnetic resonance images by means of a phase-corrected real reconstruction," *Medical Physics*, vol. 15, p. 813 817, 1989.

[10] W. Edelstein, G. Glover, C. Hardy, and R. Redington, "The intrinistic signal-to-noise ratio in NMR imaging," *Magnetic Resonance in Medicine*, vol. 3, p. 604618, 1986.

[11] A. Papoulis, *Probability, Random variables, and Stochastic Processes*. McGraw-Hill, 1984.

[12] R. Gonzalez and P. Wintz, *Digital Image Pprocessing*, 2nd ed. Addison-Wesley, 1987.

[13] A. K. Jain, *Fundamentals of Digital Image Processing*. Upper Saddle River, NJ, USA: Prentice-Hall, Inc., 1989.

[14] L. G. Roberts, "Machine perception of three dimensional solids," *International journal of Tippett et al. (Eds.), Optical and electro-optical information processing*, pp. 159–197, 1965.

[15] T. Bae, M. Giger, C. Chen, and C. Kahn, "Automatic segmentation of liver structure in CT images," *Medical Physics*, vol. 20, pp. 71–78, 1993.

[16] G. K. von Schutthess, *Morphology and Function in MRI*, 1989.

[17] A. Goshtasby and D. Turner, "Segmentation of cardiac cine MR images for extraction of right and left ventricular chambers," *IEEE Transactions on Medical Imaging*, vol. 14, no. 1, pp. 56–64, 1995.

[18] S. Warfield, J. Dengler, J. Zaers, C. Guttmann, W. Gil, J. Ettinger, J. Hiller, and R. Kikinis, "Automatic identification of grey matter structures from MRI to improve the segmentation of white matter lesions," *Journal of Image Guided Surgery*, vol. 1, no. 6, pp. 326 – 338, 1995.

[19] M. Kass, A. Witkin, and D. Terzopolous, "Snakes: Active contour models," *International journal of computer vision*, vol. 4, pp. 321–331, 1988.

[20] R. Surendra, "Contour extraction from CMRI studies using snakes," *IEEE Transactions on Medical Imaging*, vol. 14, no. 2, pp. 21–32, June 1995.

[21] R. Li, S. Brown, L. Wilson, J. Young, and S. Luo, "Progressively refined patient-specific vessel system models from generic representations," in *Digital Image Computing Techniques and Applications*, Melbourne, Australia, 2002, pp. 1–6.

[22] S. Osher and J. Sethian, "Fronts propagating with curvature dependent speed: Algorithms based on hamilton-jacobi formulation," *Journal of Computational Physics*, vol. 79, pp. 12–49, 1988.

[23] R. Malladi, J. Sethian, and B. Vemuri, "Shape modeling with front propagation: a level set approach," *IEEE Transactions on Pattern Analysis and Machine Intelligence*, vol. 17, no. 2, pp. 158–175, February 1995.

[24] J. Gomes and O. Faugeras, "Reconciling distance functions and level sets," *Journal of Visual Communication and Image Representation*, vol. 11, pp. 209–223, 2000.

[25] C. Li, C. Xu, C. Gui, and M. Fox, "Level set formulation without re-initialization: a new variational formulation," in *IEEE International Conference on Computer Vision and Pattern Recognition (CVPR)*, vol. 1, 2005, pp. 430–436.

[26] N. Paragios, "A level set approach for shape-driven segmentation and tracking of the left ventricle," *IEEE Transactions on Medical Imaging*, vol. 22, no. 6, pp. 773–776, June 2003.

[27] D. Adalsteinsson and J. Sethian, "A fast level set method for propagating interfaces," *Journal of Computational Physics*, vol. 118, pp. 169–277, 1995.

[28] R. Gonzalez, T. Deschamps, R. Idica, R. Malladi, and C. Solorzano, "Automatic segmentation of histological structures in mammary gland tissue sections," *Lawrence Berkeley National Laboratory*, pp. 1–29, 2004.

[29] T. Chan and L. Vese, "Active contours without edges," *IEEE Transactions on Image Processing*, vol. 10, no. 2, pp. 266–277, February 2001.

[30] K. V. Mardia and T. Hainsworth, "A spatial thresholding method for image segmentation," *IEEE Transactions on Pattern Analysis and Machine Intelligence*, vol. 10, pp. 919–927, 1988.

[31] S. S. Sahoo, P. and A. Wong, "A survey of thresholding techniques," *Comput. Vis. Graph. Im. Proc.*, vol. 41, pp. 233–260, 1988.

[32] R. J. Schalkoff, *Pattern Recognition: Statistical, Structural and Neural Approaches*. John Wiley and Sons, 1992.

[33] T. Cover and P. Hart, "Nearest neighbor pattern classification," *IEEE Transactionson Information Theory*, vol. 13, pp. 21–27, 1967.

[34] R. O. Duda and P. E. Hart, *Pattern Classification and Scene Analysis*. Wiley, 1973.

[35] P. Domingos and M. Pazzani, "On the optimality of the simple bayesian classiffier under zero-one loss," *Machine Learning*, vol. 29, pp. 103–130, 1997.

[36] W. Wells, W. Grimson, R. Kikins, and F. Jolesz, "Adaptive segmentation of MRI data," *IEEE Transactions on Medical Imaging*, vol. 15, p. 429 442, 1996.

[37] M. Tood, "The expectation maximization algorithm," *IEEE Signal Processing Magazine*, pp. 47–60, November 1996.

[38] Z. Yu and H. Wong, "Fema : A fast expectation maximization algorithm based on grid and PCA," in *IEEE Multimedia ans Expo*, 2006, pp. 1913 – 1916.

[39] I. Pollak, A. S. Willsky, and H. Krim, "Image segmentation and edge enhancement with stabilized inverse diffusion equations," *IEEE Transactions on Image Processing*, vol. 9, no. 2, pp. 256–266, February 2000.

[40] M. R. Rezaee, P. M. J. van der Zwet, B. P. E. Lelieveldt, R. J. van der Geest, and J. H. C. Reiber, "A multiresolution image segmentation technique based on pyramidal segmentation and fuzzy clustering," *IEEE Transactions on Image Processing*, vol. 9, no. 7, pp. 1238–1248, July 2000.

[41] R. G. Thomas, B. and S. Wangmo, "A modified fuzzy c-means algorithm for natural data exploration," *World Academy of Science, Engineering and Technology*, vol. 49, pp. 478–481, 2009.

[42] K. V. Mardia, "Special issue on statistic image analysis," *Journal of Applied Statistics*, vol. 16, 1989.

[43] S. Z. Li, *Markov Random field Modeling in Computer Vision*. Springer, 1995.

[44] T. N. Pappas, "An adaptive clustering algorithm for image segmentation," *IEEE Signal Processing*, vol. 40, pp. 901–914, 1992.

[45] S. Geman and D. Geman, "Stochastic relaxation, Gibbs distrutions, and the Bayesian restoration of images," *IEEE Transaction on Pattern Analysis and Machine Intelligence*, vol. 6, pp. 721–741, 1984.

[46] C. Davatzikos, M. Vaillant, S. Resnick, J. Prince, S. Letovsky, and R. Bryan, "A computerized method for morphological analysis of the corpus callosum," *J. Comp. Assist. Tom*, vol. 20, pp. 88–97, 1996.

[47] M. Cuadraa, M. Craeneb, V. Duaya, B. Macqb, C. Polloac, and J. Thirana, "Dense deformation field estimation for atlas-based segmentation of pathological MR brain images," *Comput. Meth. Prog. Biomed*, vol. 84, pp. 66–75, 2006.

[48] L. Vincent and P. Soille, "Watersheds in digital spaces: An efficient algorithm based on immersion simulation," *IEEE Transactions on Pattern Analysis and Machine Intelligence*, vol. 13, p. 583598, 1991.

[49] J. Sijbers, P. Scheunders, M. Verhoye, A. Linden, and D. Dyck, "Watershed-based segmentation of 3D MR data for volume quantization," *Magnetic Resonance Imaging*, vol. 15, p. 679 688, 1997.

[50] A. F. Frangi, W. J. Niessen, and M. A. Viergever, "Three-dimensional modeling for functional analysis of cardiac images, a review," *IEEE Transactions on Medical Imaging*, vol. 20, no. 1, pp. 2–5, January 2001.

[51] A. Qazi, J. D. Kim, J., and V. Pekar, "Probabilistic refinement of model-based segmentation: application to radiation therapy planning of the head and neck," in *Medical imaging and augmented reality*, ser. LNCS, vol. 6326. Springer, 2010, pp. 403–410.

[52] S. Wang and J. Siskind, "Image segmentation with ratio cut," *IEEE Transactions on Pattern Analysis and Machine Intelligence*, vol. 25, no. 6, pp. 675–690, June 2003.

[53] S. Wang, "Image segmentation with ratio cut - extended version," University of South Carolina, Columbia SC 29208 USA, Tech. Rep., 2002.

[54] Z. J. Hou and G. W. Wei, "A new approach to edge detection," *Pattern Recognition Letters*, no. 35, p. 15591570, 2002.

[55] M. E. Farmer and A. K. Jain, "A wrapper-based approach to image segmentation and classification," *IEEE Transactions on Image Processing*, vol. 14, no. 12, pp. 2060–2072, Dec. 2005.

[56] W. Vanzella and V. Torre, "A versatile segmentation procedure," *IEEE Transactions on Systems, Man, and Cybernetics, Part B: Cybernetics*, vol. 36, no. 2, pp. 366–378, April 2006.

[57] A. Pednekar, U. Kurkure, R. Muthupillai, S. Flamm, and I. Kakadiaris, "Automated left ventricular segmentation in cardiac MRI," *IEEE Transactions on Biomedical Engineering*, vol. 53, no. 7, pp. 1425–1428, July 2006.

[58] G. Herman and D. Odhner, "Performance evaluation of an iterative image reconstruction algorithm for positron emission tomography," *IEEE Transactions on Medical Imaging*, vol. 10, no. 3, pp. 336–346, September 1991.

[59] D. Nuzillard and C. Lazar, "Partitional clustering techniques for multi-spectral image segmentation," *Journal of Computing*, vol. 2, no. 10, December 2007.

[60] C. Pluempitiwiriyawej, J. Moura, W. Yi-Jen Lin, and H. Chien, "STACS: new active contour scheme for cardiac MR image segmentation," *IEEE Transactions on Medical Imaging*, vol. 24, no. 5, pp. 593–603, May 2005.

[61] M. Lynch, O. Ghita, and P. F. Whelan, "Segmentation of the left ventricle of the heart in 3-D+t MRI data using an optimized nonrigid temporal model," *IEEE Transactions on Medical Imaging*, vol. 27, no. 2, pp. 195–203, February 2008.

[62] D. Adalsteinsson and J. Sethian, "Level set methods for etching, deposition and photolithography development," in *SISPAD 96: Special Issue of IEEE Transactions on Computer-Aided-Design*, 1996.

[63] K. W. Sum and P. Y. S. Cheung, "Vessel extraction under non-uniform illumination: a level set approach," *IEEE Transactions on Biomedical Engineering*, vol. 55, no. 1, pp. 358–360, January 2008.

[64] V. Kolmogorov, "Graph based algorithms for scene reconstruction from two or more views," Ph.D. dissertation, Cornell University, 2004.

[65] S. Jianbo and J. Malik, "Normalized cuts and image segmentation," *IEEE Transactions on Pattern Analysis and Machine Intelligence*, vol. 22, no. 8, pp. 888–905, August 2000.

[66] S. P. Dakua and J. S. Sahambi, "Noise effect on LV image segmentation," in *IEEE INDICON 2009*, Gandhinagar, 2009, pp. 1–4.

[67] L. Grady, "Random walks for image segmentation," *IEEE Transactions on Pattern Analysis and Machine Intelligence*, vol. 28, no. 11, pp. 1768–1783, Nov 2006.

[68] B. Smolka and K. W. Wojciechowski, "Random walk approach to image enhancement," *Signal Processing*, vol. 81, no. 3, p. 465482, 2001.

[69] M. Szczepanski, B. Smolka, K. Plataniotis, and A. Venetsanopoulos, "On the geodesic paths approach to color image filtering," *Signal Processing*, vol. 83, no. 6, p. 13091342, 2003.

[70] X. Sun, P. L. Rosin, R. R. Martin, and F. C. Langbein, "Random walks for mesh denoising," in *SPM 07: Proceedings of the 2007 ACM symposium on Solid and physical modeling*. NY, USA: ACM, 2007, pp. 11–22.

[71] S. Xianfang, R. Paul, M. Ralph, and L. Frank, "Random walks for feature-preserving mesh denoising," *Computer Aided Geometric Design, Elsevier*, no. 25, pp. 437–456, 2008.

[72] H. Wechsler and M. Kidode, "A random walk procedure for texture discrimination," *IEEE Transactions on Pattern Analysis and Machine Intelligence*, vol. 1, no. 3, p. 272280, 1979.

[73] D. Aldous and J. Fill, *Reversible Markov Chains and Random Walks on Graphs*. University of California, Berkeley, 2002.

[74] Z. Tu and S. Zhu, "Image segmentation by data-driven markov chain monte carlo," *IEEE Transactions on Pattern Analysis and Machine Intelligence*, vol. 24, no. 5, p. 657673, 2002.

[75] B. Smolka, M. Szczepanski, K. lataniotis, and A. Venetsanopoulos, "Random walk approach to noise reduction in images," ser. LNCS, vol. 2124. Springer-Verlag, 2002, pp. 527–536.

[76] F. Chung, *Spectral Graph Theory*. Regional conference series in mathematics. Providence, R.I.: American Mathematical Society, 1997, no. 92.

[77] R. Courant and D. Hilbert, *Methods of Mathematical Physics*. Wiley and Sons, 1989, vol. 2.

[78] E. Fieller, H. Hartley, and E. Pearson, *Test for Rank Correlation Coefficients*. Biometrika, 1957, vol. 44.

[79] Boylestad, *Introductory Circuit Analysis*, 10th ed. Prentice Hall, 2002.

[80] Cooper and M. Jeffery, *Introduction to Partial Differential Equations with MATLAB*. A Birkhuser book, ISBN: 978-0-8176-3967-9, 2000.

[81] P. Perona and J. Malik, "Scale space and edge detection using anisotropic diffusion," *IEEE Transactions on Pattern Analysis and Machine Intelligence*, vol. 12, no. 7, pp. 888–905, Jul. 1990.

[82] F. Boribhoje and P. Alex, "An adaptive real-time ECG compression algorithm with variable threshold," *Biomedical Engineering, IEEE Transactions on*, vol. 35, no. 6, 1988.

[83] E. Page, *Continuous Inspection Schemes*. Biometrika, 1954, vol. 41.

[84] L. Bruzzone and D. Prieto, "An adaptive parcel-based technique for unsupervised changedetection," *International journal of Remote Sensing*, vol. 21, no. 4, pp. 817–822, 2000.

[85] T. Carvalho, L. Fonseca, F. Murtagh, and J. Clevers, "Digital changedetection with the aid of multi-resolution wavelet analysis," *International journal of Remote Sensing*, vol. 22, no. 18, pp. 3871–3876, 2001.

[86] T. Fung, "An assessment of TM imagery for land-cover change detection," *IEEE Transactions on Geoscience and Remote Sensing*, vol. 28, no. 4, pp. 681–684, Jul 1990.

[87] S. Jianbo and J. Malik, "Normalized cuts and image segmentation," *IEEE Transactions on Pattern Analysis and Machine Intelligence*, vol. 22, no. 8, pp. 888–905, August 2000.

[88] X. Zhu, J. Lafferty, , and Z. Ghahramani, "Combining active learning and semi-supervised learning using gaussian fields and harmonic functions," in *ICML 2003 workshop on The Continuum from Labeled to Unlabeled Data in Machine Learning and Data Mining*, 2003, pp. 58–65.

[89] G. Healey and R. Kondepudy, "Radiometric ccd camera calibration and noise estimation," *IEEE Transactions on Pattern Analysis and Machine Intelligence*, vol. 16, no. 3, pp. 267–276, Mar 1994.

[90] J. Sijbers and A. Dekker, "Maximum likelihood estimation of signal amplitude and noise variance from mr data," *Magnetic Resonance in Medicine*, vol. 51, no. 3, pp. 586–594, 2004.

[91] H. Voorhees and T. Poggio, "Detecting blobs as textons in natural images," in *Image Understanding Workshop*. Los Angeles: Portal, ACM, 1987, pp. 892–899.

[92] D. Dobkin, S. Friedman, and K. Supowit, "Delaunay graphs are almost as good as complete graphs," *Discrete and Computational Geometry*, vol. 5, no. 4, pp. 399–407, 1990.

[93] L. Guibas and J. Stolfi, "Primitives for the manipulation of general subdivisions and the computation of voronoi diagrams," *ACM Transactions on Graphics*, vol. 4, pp. 74–123, 1985.

[94] X. S., P. Rosin, R. Martin, and F. Langbein, "Fast and effective feature-preserving mesh denoising," *IEEE Transactions on Visualization and Computer Graphics*, vol. 13, no. 5, pp. 925–938, Sept.-Oct. 2007.

[95] S. P. Dakua and J. S. Sahambi, "Automatic left ventricular contour extraction from cardiac magnetic resonance images using cantilever beam and random walk approach," *Cardiovascular Engineering, Springer*, vol. 10, pp. 30–43, 2009.

[96] A. Chandra, P. Raghavan, W. Ruzzo, R. Smolensky, and P. Tiwari, "The electrical resistance of a graph captures its commute and cover times," *Computational Complexity*, vol. 6, pp. 312–340, 1996/1997.

[97] C. L. W. Fen, J. and C. Chen, "Automatic left ventricular boundary detection in digital two-dimensional echocardiography using fuzzy reasoning techniques," in *Biomedical Image Processing, SPIE*, vol. 192, anta Clara, CA, USA, 1990.

[98] W. Liang, P. Kanani, J. Allan, R. Kerber, C. McKay, and S. M., "Left ventricle myocardial border detection in three-dimensional intracardiac ultrasound images," in *Medical Imaging*

1997: Physiology and Function from Multidimensional Images, SPIE, vol. 316, Newport Beach, CA, USA, 1997.

[99] M. Brejl and M. Sonka, "Medical image segmentation: Automated design of border detection criteria from examples," *J. Electron. Imaging*, vol. 8, no. 54, 1999.

[100] D. E. Chu, C. and A. Buda, "Detecting left ventricular endocardial and epicardial boundaries by digital two-dimensional echocardiography," *IEEE Transactions on Medical Imaging*, vol. 7, pp. 81–90, 1988.

[101] L. W. Feng, J. and C. Chen, "Epicardial boundary detection using fuzzy reasoning," *IEEE Transactions on Medical Imaging*, vol. 10, pp. 187–199, 1991.

[102] K. Ong and A. Foong, "A knowledge-based approach to the analysis of cardiac images in digital echocardiography," in *IEEE International Conference on Image Processing*, vol. 1, Singapore, 1989, pp. 141–145.

[103] J. Bosch, J. Reiber, G. Burken, J. Gussenhoven, N. Bom, and J. Roelandt, "Automated endocardial contour detection in short-axis 2-D echocardiograms; Methodology and assessment of variability," in *Comput. Cardiology*, Washington, D.C., 1988, pp. 137–140.

[104] J. J. Lilly, P. and P. Bourdillon, "Automatic contour definition on left ventriculograms by image evidence and a multiple template based model," *IEEE Transactions on Medical Imaging*, vol. 8, pp. 173–185, 1989.

[105] G. E. A. J. Ezekiel, A. and S. Corday, "Automatic and intelligent left ventricular contour detection from twodimensional echocardiograms," in *Computer Cardiology*. Linkoping, Sweden: IEEE Computer Society, 1985, pp. 261–264.

[106] M. Hassanzadeh, "Two new methods for finding endocardial and epicardial boundaries in echocardiographic images using wavelet analysis," *European Journal of Scientific Research*, vol. 27, pp. 264–274, 2009.

[107] M. Fedoryuk, *Method of Steepest Descent*, ser. Encyclopaedia of Mathematics. Springer, ISBN 978-1556080104, 2001.

[108] S. P. Dakua and J. S. Sahambi, "A strategic approach for left ventricular cardiac MR image segmentation," *Cardiovascular Engineering, Springer*, vol. 10, pp. 163–168, 2010.

[109] R. Fasol, W. T., B. Pfannmuller, J. Stumpf, and R. Hacker, "Papillary muscle shortening for mitral valve reconstruction in patients with ischaemic mitral insufficiency," *European Heart Journal*, vol. 19, p. 17301734, 1998.

[110] G. P. Axler, S. and K. Voss, "The Dirichlet problem on quadratic surfaces," *Mathematics of Computation*, vol. 73, pp. 637–651, 2004.

[111] F. Fouss, A. Pirotte, J. Renders, , and M. Saerens, "Random walk computation of similarities between nodes of a graph with application to collaborative recommendation," *IEEE Transactions on Knowledge and Data Engineering*, vol. 19, pp. 355–369, 2007.

[112] A. Shiozaki, "Edge extraction using entropy operator," *Computer Vision, Graphics and Image Processing*, vol. 36, pp. 1–9, 1986.

[113] M. M. Singh, M. and A. Basu, "Gaussian and Laplacian of Gaussian weighting functions for robust feature based tracking," *Pattern Recognition Letters*, p. 19952005, 2005.

[114] M. Pertti, *Geometry of Sets and Measures in Euclidean Spaces: Fractals and Rectifiability*. Cambridge: Cambridge University Press, 1995.

[115] X. Wang, "Laplacian operator-based edge detectors," *IEEE Transactions on Pattern Analysis and Machine Intelligence*, vol. 29, pp. 886–890, 2007.

[116] L. Liu and G. Wang, "Recursive formulae for Hermite polynomial approximations to rational Bezier curves," *Geometric Modeling and Processing Theory and Applications*, vol. 2, pp. 190–197, 2000.

[117] S. P. Dakua and J. S. Sahambi, "Modified active contour model and random walk approach for left ventricular cardiac MR image segmentation," *International Journal for Numerical Methods in Biomedical Engineering, Wiley*, 2010 (Accepted), DOI: 10.1002/cnm.

[118] J. Prewitt, "Object enhancement and extraction," *Picture Processing and Psychopictorics, Academic Press*, 1970.

[119] J. Canny, "A computational approach to edge detection," *IEEE Transactions on Pattern Analysis and Machine Intelligence*, vol. 8, p. 679698, 1986.

[120] I. Sobel and G. Feldman, "A 3*3 isotropic gradient operator for image processing," 1968, presented at a talk at the Standford Artifial Project in 1968.

[121] C. Olsen and F. Georgsson, "Assessing ground truth of glandular tissue," *Digital Mammography, Lecture Notes in Computer Science, 2006, Volume 4046/2006, 10-17*, vol. 4046, pp. 10–17, 2006.

[122] R. Unnikrishnan, P. Caroline, and M. Hebert, "Toward objective evaluation of image segmentation algorithms," *IEEE Transactions on Pattern Analysis and Machine Intelligence*, vol. 29, pp. 929–944, 2007.

[123] S. Chabrier, B. Emile, H. Laurent, C. Rosenberger, and P. March, "Unsupervised evaluation of image segmentation application to multi-spectral images," *Pattern Recognition, International Conference on*, vol. 1, pp. 576–579, 2004.

[124] W. K. Pratt, *Digital Image Processing*. New York: John Wiley & Sons, 1991.

[125] F. O. Pratt, W. and A. Gagalowicz, "Visual discrimination of stochastic texture fields," *IEEE Trans. on Syst., Man, and Cyber.*, vol. 8, pp. 796–804, 1978.

[126] K. G. Huttenlocher, D. and W. Rucklidge, "Comparing images using the Hausdorff distance," *IEEE Transactions on Pattern Analysis and Machine Intelligence*, vol. 15, pp. 850–863, 1993.

[127] S. Weszka and A. Rosenfeld, "Threshold evaluation techniques," *IEEE Transactions on Systems, Man and Cybernetics*, vol. 8, pp. 622 – 629, 1978.

[128] A. Nazif and M. Levine, "Low level image segmentation: An expert system," *IEEE Transactions on Pattern Analysis and Machine Intelligence*, vol. 6, pp. 558–577, 1984.

[129] M. Levine and A. Nazif, "Dynamic measurement of computer generated image segmentations," *IEEE Transactions on Pattern Analysis and Machine Intelligence*, vol. 7, pp. 155–164, 1985.

[130] L. V. Z. Y. I. C. S. H. C. L. H. B. Udupa, J. K. and J. Woodburn, "A framework for evaluating image segmentation algorithms," *Computerized Medical Imaging and Graphics*, vol. 30, pp. 75–87, 2006.

[131] J. Mathews and K. Docksum, *Complex Analysis for Mathematics and Engineering*. Jones and Bartlett Publishers, 2001.

[132] R. M. Hartenstein, H. and D. Saupe, "Region-based fractal image compression," *IEEE Transaction on Image Processing*, vol. 9, pp. 1171 – 1184, 2000.

[133] Z. Z. Yang, E. and T. Berger, "Fixed-slope universal lossy data compression," *IEEE Transaction on Information Theory*, vol. 43, pp. 1465 – 1476, 1997.

[134] G. Miaou and S. Chao, "Wavelet-based lossy-to-lossless ECG compression in a unified vector quantization framework," *IEEE Transactions on Biomedical Engineering*, vol. 52, pp. 539 – 543, 2005.

[135] T. I. Giurcneanu, C. and S. Mereuta, "Using contexts and R-R interval estimation in lossless ECG compression," *Comput. Meth. Prog. Biomed.*, vol. 67, pp. 177–186, 2002.

[136] A. Koski, "Lossless ECG encoding," *Comput. Meth. Prog. Biomed*, vol. 52, pp. 23–33, 1997.

[137] S. P. Dakua and J. S. Sahambi, "Lossless ECG compression for event recorder based on Burrows-Wheeler transformation and move-to-front coder," *International Journal of Recent Trends in Engineering, Academy Publisher*, vol. 1, pp. 120 – 123, 2009.

[138] ——, "Detection of left ventricular myocardial contours from ischemic cardiac MR images," *IETE Journal of Research*, Accepted, Likely to appear in Jul-Aug: 2011 issue.

[139] D. Chien and R. Edelman, "Ultrafast imaging using gradient echoes," *Magnetic Resonance in Medicine*, vol. 7, p. 3156, 1991.

[140] N. R. Council, "Mathematics and physics of emerging biomedical imaging," National Academy Press, Washington, D.C., Tech. Rep., 1996.

Chapter 8

Publications

8.1 Journal Papers (Published/Accepted)

1. S. P. Dakua and J. S. Sahambi, "Modified Active contour Model and Random Walk Approach for Left Ventricular Cardiac MR Image Segmentation", International Journal for Numerical Methods in Biomedical Engineering, Wiley, (2011) 27: 1350-1361, DOI: 10.1002/cnm.1430.

2. S. P. Dakua and J. S. Sahambi, "Detection of Left Ventricular Myocardial Contours from Ischemic Cardiac MR Images", IETE Journal of Research, (2011) 57:372-384, DOI: 10.4103/0377-2063.86338.

3. S. P. Dakua and J. S. Sahambi, "A Strategic Approach for Left Ventricular Cardiac MR Image Segmentation, Cardiovascular Engineering, Springer, (2010) 10:163-168, DOI 10.1007/s10558-010-9102-3, 2010.

4. S. P. Dakua and J. S. Sahambi, "Automatic Contour Extraction of Multi-labeled Left Ventricle from CMR Images Using CB and Random Walk Approach", Cardiovascular Engineering, Springer, (2010) 10:3043, DOI 10.1007/s10558-009-9091-2, 2010.

5. S. P. Dakua and J. S. Sahambi, "LV Contour Extraction from Cardiac MR Images Using Random Walk Approach," International Journal of Recent Trends in Engineering, Academy Publisher, vol. 1, no. 3, pp. 101 - 105, 2009.

8.2 CONFERENCE PUBLICATIONS

1. S. P. Dakua and J. S. Sahambi, "Weighting Function in Random Walk Based Left Ventricle Segmentation," in Proc. of IEEE International Conference on Image Processing (ICIP) 2011, Brussels, pp. 2133 - 2136.

2. S. P. Dakua and J. S. Sahambi, "Modified Random Walk Approach for Left Ventricular Contour Extraction from Cardiac MR Images," in Proc. of IEEE SPCOM 2010, Bangalore, pp. 1-4.

3. S. P. Dakua and J. S. Sahambi, "Noise Effect on LV image Segmentation," in Proc. of IEEE INDICON 2009, Gandhinagar, pp. 1-4.

4. S. P. Dakua S. and J. S. Sahambi, "LV Contour Extraction Using Difference of Gaussian Weighting Function and Random Walk Approach," in Proc. of IEEE INDICON 2009, Gandhinagar, pp. 1-4.

5. S. P. Dakua and J. S. Sahambi, "Unequal Error Protection based LV Segmented CMR Image Transmission Through Wireless Communication Channels," in Proc. of IEEE UKI-WCWS on Dec. 11-12, 2009.

6. S. P. Dakua and J. S. Sahambi, "Left Ventricular Contour Extraction from Cardiac MR Images Using CB and Random Walks Approach," in Proc. of IEEE NaBIC 2009 (9-11 Dec.), Coimbatore, pp. 276 - 281.

7. S. P. Dakua and J. S. Sahambi, "Effect of β in Random Walks Approach for LV Contour Extraction," in Proc. of IEEE CISIM 2009 (9-11 Dec.), Coimbatore, pp. 890-895.

8. S. P. Dakua and J. S. Sahambi, "LV Contour Extraction from Cardiac MR Images Using Random Walks Approach," in Proc. of IEEE International Advance Computing Conference 2009, Patiala, pp. 228 - 233.

9. S. P. Dakua and J. S. Sahambi, "LV Contour Extraction from Cardiac MR Images Using Random Walks Approach," in IJJCE 2009.

10. S. P. Dakua and J. S. Sahambi, "A Level Set Method for Cardiac Magnetic Resonance Image Segmentation: An Adaptive Approach," in Proc. of IEEE Third international Conference on Industrial and Information Systems 2008, IIT Kharagpur, pp. 1-6.

8.3 WORKSHOP ATTENDED

1. IEEE 802.16 Mobile WiMAX Workshops, Organized by Intel Higher Education Program at IIT Guwahati, on 17th May, 2010.